Static and Dynamic Properties of Rapidly Solidified Powder Metallurgy Magnesium Alloys: Evaluation and Simulation

By

Ayman Hamada Abd El Hady Elsayed

Division of Mechanical Engineering

Graduate School of Engineering

Osaka University

2011

Static and Dynamic Properties of Rapidly Solidified Powder Metallurgy Magnesium Alloys: Evaluation and Simulation

By

Ayman Hamada Abd El Hady Elsayed

Division of Mechanical Engineering

Graduate School of Engineering

Osaka University

2011

Contents

Chapter 1 Introduction

1.9. Magnesium and its alloys

Magnesium and its alloys are widely used in a variety of structural and nonstructural applications [1]. Structural applications include automobile, industrial, material handling, and aerospace equipment. Nonstructural applications include being used as alloying element in various alloys including aluminum, zinc, copper, and even ferrous alloys, like being used as a graphitizing agent in nodular cast iron. Magnesium alloys are usually divided into Zr-containing and Zr-free alloys, as the effects of grain refinement of Zr are much considerable. Zr-containing alloys include Mg-Zn-Zr and Mg-Y-Zn-Zr classes of alloys. Zr-free alloys include Mg-Al, Mg-Al-Zn, Mg-Al-Si, Mg-Al-RE, and others. Mg-alloys are usually produced using sand and permanent mold casting, die casting, extrusion, and forging.

The crystal structure of magnesium is hexagonal close packed (hcp), as shown in Fig. 1.1. Despite the important advantages of magnesium alloys, like the high strength-to-weight ratio [3], the hcp crystal structure disadvantageously reduces the room temperature formability of magnesium alloys, which considerably limit their applications [4]. At room temperature, the critical resolved shear stress (CRSS) of the basal plane (0001) is much lower than those of other non-basal planes [5]. This gives rise for the activation of the basal plane only, which limits the ductility. However, at higher temperatures, the CRSS of various slip systems become closer, which permits their parallel activation, and eventually, increases the formability of the alloy [4].

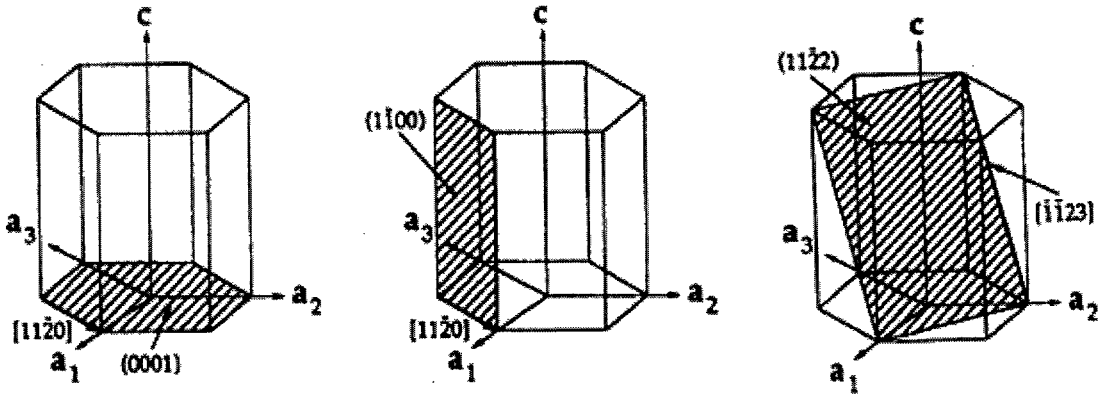

Fig. 1.1 The hexagonal close packed (hcp) crystal structure [1].

1.10. Strengthening mechanisms of Mg-alloys

Efforts have been done to improve the properties of magnesium alloys based on various strengthening mechanisms, including, chemical alloying, thermo-mechanical processing, and rapid solidification.

1.10.1. Chemical alloying

Chemical alloying has been extensively used to improve the properties of Mg alloys. Amongst alloying elements used with Mg alloys, rare earths have shown promisingly positive effects on the properties of Mg alloys. It has been reported that alloying with La, Ce and Gd resulted in grain refinement of Mg, leading to the increase in the strength [6]. Rare earths have also shown another important advantage of reducing the texture strength of basal plane, an effect that eventually improved the ductility of Mg alloys [7]. The same effect of reducing texture strength has also been reported to increase the formability of Mg sheets [8]. Moreover, the compound effect of both grain refinement and weakening of texture was also

shown for rare earth, leading to an improvement of the mechanical properties of Mg alloys [9]. Creep resistance of Mg alloys has also been shown to improve by using alloying with rare earths, especially through the mechanism of suppression of grain boundary sliding and dislocation motion caused by fine dispersed stable Al-La compound particles along the grain boundaries [10, 11]. Corrosion resistance has also been reported to improve as a result of the decrease of galvanic corrosion caused by the rare earths' effect of suppression of Mg-Al (β-phase) and the formation of Al-La (γ-phase) [12]. La was also shown to improve the mechanical properties of Mg-alloys that contain Al-Zn-Ca additions through its effects on grain refinement and the formation of finely dispersed compound particles [13]. Furthermore, La is much cheaper than the other rare earth alloying elements, and is one of the effective additions to Mg alloys for their performance improvement.

Other alloying elements which have shown good effects on the strength of Mg-alloys include, but not limited to, Zn, Zr, Mn, Y, and Ca. Zr has been shown as an effective element for the grain refinement of Mg-alloys [2]. It was also shown as an important factor for the strengthening of Mg-alloys when combined with other elements like Zn [14]. Mn addition with carefully adjusted contents have also contributed to the increase in the fatigue strength of Mg-alloys, but when its content increased, it tended to have the adverse effect of forming harmful compounds that worked as stress raisers [15].

Mg-Y-Zn series of alloys have also shown a unique structure of long period stacking order (LPSO) phase that provided Mg-alloys with improved properties [16]. The quasi-crystalline icosahedral phase provides unique set of properties due to its thermal stability and strong bonding to the Mg matrix [17]. The Mg-Y-Zn-Zr alloy combination has also shown high mechanical strength in its as-cast form due to the combined effects of LPSO phase [18,

19]. Ca also has shown positive effects on Mg-alloys through its role to decrease the alloy combustibility and to increase its high temperature strength [20, 21]. It has also revealed its promising effect of forming fine intermetallic compounds that contributed to the increase in the tensile properties of Mg-alloys [22].

1.10.2. Thermo-mechanical processing

Thermo-mechanical processing was also shown as an important mechanism for the strengthening of Mg-alloys. Repeated plastic working has been reported to improve the mechanical response through grain refinement [23]. Equal channel angular extrusion (ECAE) has also been reported to refine magnesium grains and reduce texture, which in turn increased the yield strength of AZ31 alloy [24]. It was reported that ECAE has resulted in an extensive grain refinement of AZ31 alloy by the fragmentation of large grains of the as-extruded alloy [25]. ECAE was also shown as an effective means for the realization of high strength of AZ31 magnesium alloy through its combined effects of grain refinement and texture modification [26]. Not only the strength of Mg-alloys were reported to improve, but also the toughness of AZ31 alloy could be improved, compared to that of the as-cast alloy, by the use of ECAE via the activation of new deformation mechanisms; namely the fine grain rotation and the parallel wrinkled deformation types [27].

In these studies, and in other studies as well [4, 28, 29], the Hall-Petch relationship describing the trend of increasing the yield strength with decreasing of the grain size was shown to prevail. The strengthening factor of Mg alloys in this relationship has shown exceptionally high values (0.2 to 0.34 MPa $\sqrt{m}$) compared to that of other materials, like Al which shows

lower values (about 0.07 MPa √m) [30]. This shows the strong effect of grain refinement on the properties of Mg alloys.

It has also been reported that various Mg-alloys could be shown to follow the Hall-Petch relationship strictly [13, 22]. The strengthening factors for those alloys have been 0.170 MPa √m and 0.192 MPa √m for Mg-Al-Zn-Ca-La and Mg-Al-Mn-Ca alloys, respectively. Those values also corresponded well to the above shown range of the strengthening factor of Mg-alloys.

1.10.3.Rapid solidification

Grain refinement could be obtained in metals by rapid solidification [31-34]. It was shown that rapid solidification can contribute to the realization of high strength of magnesium alloys containing both Al-Ca and Zn-RE combinations. Li et al. reports the improvement of tensile properties of AZ91HP alloy strengthened with Si C through the use of rapid solidification [31]. Mg-Y-Zn alloys have also been reported to improve through the use of rapid solidification much more compared to conventional cast ones [32, 33], and further improved by the use of reciprocating extrusion [34].

The use of powder metallurgy processing technique has provided promising improvements in the mechanical responses of Mg-alloys [13, 14, 22, 35]. In these reports, alloys like Mg-Zn-Zr, Mg-Al-Mn-Ca, and Mg-Al-Zn-Ca-La have been fabricated using powder metallurgy processing and hot extrusion, and have shown excellent tensile properties compared to those of their extruded cast forms. The Mg-Al-Mn-Ca alloy have shown an increase in tensile strength of about 30 % for extruded powders compared to that of extruded cast billets [22]. However, the elongation has decreased about 40 %.

On the other hand, the Mg-Al-Zn-Ca-La alloy has shown a better increase in its strength to about 50 % of extruded powders compared to extruded cast billets, while attaining almost the same level of elongation [13].

The use of rapid solidification process has provided a lot of advantages including both grain refinement and super saturation of alloying elements, an effect that reduces the formation of coarse inter-metallic compounds, especially in the case of low solubility alloying elements, leading to improved mechanical response [36]. Similarly, rapidly solidified powder metallurgy Al alloys have shown an improvement of the mechanical properties [37]. Different Mg alloys have also been produced using rapidly solidified powder metallurgy technique, including Mg-Al-Zn, Mg-Al-Ca, and Mg-Zn-Y, leading to improved mechanical response [38, 33]. The authors of the current paper have also reported the well promising properties of Mg-Al-Mn-Ca alloy processed by rapidly solidified powder metallurgy, and showed that its properties are well improved compared to that of cast alloy [31].

Spinning Water Atomization Process (SWAP) has proven its ability to produce rapid solidified powder particles with ultra fine grained microstructure [37]. In this process, gas atomization is combined with water atomization in SWAP, which in turn increases the cooling rate to about 10^6 K/s, while it ranges from 10^2 to 10^5 K/s for the conventional atomization processes.

1.11. Major reported high strength Mg-alloys

Several other previous reports have also shown remarkable improvements in the mechanical properties of Mg alloys. Honma et.al. reported attaining 473 MPa yield strength, 542 MPa tensile strength and 8%

elongation for 1.8%Gd-1.8%Y-0.69%Zn-0.16%Zr Mg alloy produced through hot extrusion followed by aging treatment [39]. Similar Mg-10Gd-2Y-0.5Zr alloy has also showed good performance in the as-extruded form with better elongation of 15.3%, but lower tensile strength of 403 MPa [40]. Hot rolling was also used to produce ternary $Mg_{90.5}$ $Ni_{3.25}$ $Y_{6.25}$ (at. %) cast alloy consisting of long-period ordered phase, which resulted in 460 MPa yield strength, 526 MPa ultimate tensile strength, and 8% elongation [41]. On the other hand, processing routes like equal channel angular extrusion has also been employed to AZ31 alloy, which resulted in the ultimate tensile strength of 445 MPa [42]. Rapidly solidified powder metallurgy processing was also used to produce Mg-Zn-Y alloy showing 410 MPa yield strength with 12% elongation [16]. Reinforcing AZ91D alloy with Si-coated carbon nano-fibers has also shown a maximum tensile strength of 470 MPa for 7.5% carbon nano-fibers, but with the elongation falling to 1.7% [43].

1.12. Anisotropy of Mg-alloys

Anisotropy of mechanical properties of wrought Mg alloys caused by the strong texture has been shown as a barrier in the extension of their applications. Hence, the texture analysis became a very important tool for the evaluation and understanding of the mechanical response of Mg alloys [44]. The texture evolution during thermo-mechanical processing of Mg alloys has been investigated aiming at understanding their effects on properties of those alloys [45-47]. Based on the reported results, various conclusions have been made, with some of them suggesting that the extrusion temperature, for example, has no relation with the texture formation [45] and with others showing its effect on the amount of dynamic recrystallization [46]. The common result among most references was that the fiber texture was usually obtained after hot deformation of Mg alloys in which the basal plane is

aligned parallel to the extrusion direction [48, 49]. That strong texture was then linked to the anisotropy of mechanical properties through the possibility of favoring twinning in both tension and compression loadings. Texture evolution during hot deformation, like compression, has also been studied and the effect of both strain rate and processing temperature on the texture was revealed through the Zener-Hollomon parameter [50, 51]. It could be shown that this factor controls the recrystallization behavior of the investigated alloys.

Trials have been made to modify the texture formation, and ultimately to improve the mechanical response, in Mg alloys through the use of alloying elements, especially rare earth elements [52-58]. Those elements have shown a remarkable modification of the texture of wrought Mg alloys owing to the reduced texture strength by the formation of randomized crystal orientation [52]. That effect was shown to be mainly obtained through the formation of transverse texture component, extensive grain refinement, solute atoms interactions, and nucleation of grains at shear bands rather than inside original grains [53-56], while in some cases particle-stimulated nucleation of recrystallization has been shown as of minor effect [57]. Elongation of magnesium alloys has been ultimately improved due to that reduction in the texture strength [8, 58]. Alloying with Ca has been shown to reduce the texture strength due to the randomized nucleation of recrystallized grains at intermetallic compound particles [59]. Equal channel angular extrusion has also been reported to improve the ductility of Mg alloys in the longitudinal direction as a result of the inclined texture formation, but on the expense of reduced strength [60]. The effect of the texture on the mechanical properties of wrought Mg alloys has also been investigated and found to be mainly through the susceptibility of the deformation mechanism, namely slipping or twinning, based on the available texture pattern [61, 62]. The tensile and

compression properties have been shown to be of totally different nature for the same alloy due to the different possibilities of twinning activation [63, 64]. The grain size also has played an important role in determining whether the twinning mechanism becomes active or not, which if activated results in remarkable softening.

1.13. Study of Fracture Mechanics of Magnesium alloys

As the number of references which have discussed the fracture toughness of magnesium alloys based on standard test methods is very small, it was required to characterize the alloys produced in this study using powder metallurgy processing. This lack of references occurs despite the increasing importance of characterizing the fracture toughness of various materials when introducing them as a design solution for different applications. A few articles have discussed the fracture toughness of magnesium alloys, with their emphasis on the evaluation of both K_{IC} and CTOD fracture parameters.

1.13.1. Fracture mechanics definition and its importance

Fracture mechanics is the study of mechanical behavior of cracked materials subjected to an applied load [65]. When solids contain flaws or cracks, the field equations are not completely defined by the theory of elasticity since it does not consider the stress singularity phenomenon near a crack tip. It only provides the means to predict general yielding as a failure criterion. Despite the usefulness of predicting yielding, it is necessary to use the principles of fracture mechanics to predict fracture of solid components containing cracks [66].

The field equations are assumed to be within a small plastic zone ahead of the crack tip. If this plastic zone is sufficiently small, the small-scale yielding approach is used for characterizing brittle solids and for determining the stress and strain fields when the size of the plastic zone is sufficiently smaller than the crack length; than is, $r << a$. In contrast, a large-scale yielding is for ductile solids, in which $r \geq a$. Most static failure theories assume that the solid material to be analyzed is perfectly homogeneous, isotropic and free of stress risers or defects, such as voids, cracks, inclusions and mechanical discontinuities (indentations, scratches or gouges). Actually, fracture mechanics considers structural components having small flaws or cracks which are introduced during solidification, quenching, welding, machining or handling process [65].

1.13.2. Linear Elastic Fracture Mechanics

According to linear elastic fracture mechanics (LEFM) approach, fractures of engineering parts and structures occur when the driving force, expressed as a function that depends on the applied stress and the flaw size, exceeds the resistance force of the material. A crack in a body may be subjected to three different types of loading, which involve displacements of the crack surfaces. The mechanical behavior of a solid containing a crack of a specific geometry and size can be predicted by evaluating the stress intensity factors (K_I, K_{II} and K_{III}) shown in Fig. 1.2 [67]. As mode I loading is prevailing, K_I is usually referred as the stress intensity factor that accounts for the applied stress and the flaw size, and is representing the driving force of fracture. On the other hand, the K_{Ic} represents the critical stress intensity factor at which fracture starts to occur, which is considered as a material property that can be evaluated only by testing under strict loading and boundary conditions. It is also regarded as the plane strain fracture toughness

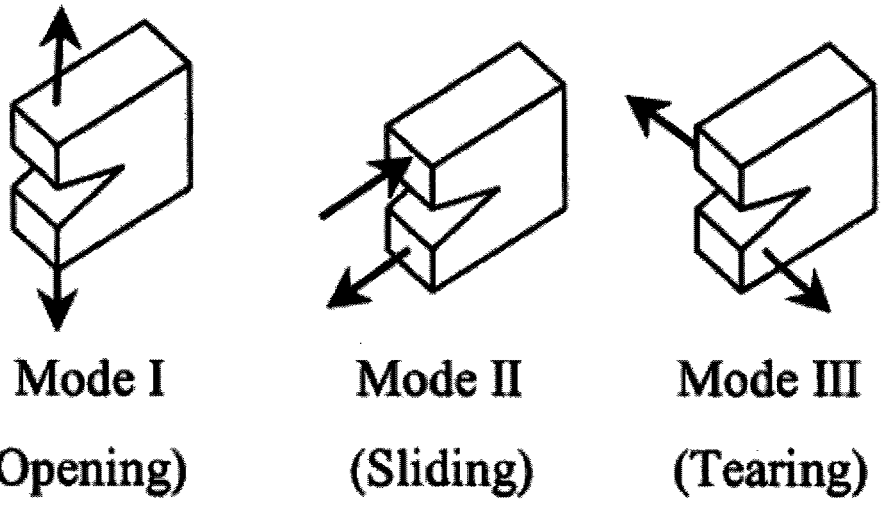

Fig. 1.2 The three loading modes of the cracked components [67].

of brittle materials, according to ASTM E 399 standard, which characterizes the fracture toughness of brittle materials [67].

On the other hand, materials with considerable ductility levels are usually characterized with parameters based on elastic-plastic approach [66]. The crack tip opening displacement (CTOD), which is the displacement of the crack surfaces due to elastic and plastic deformation at variously defined locations normal to the original (unloaded) crack plane at the tip of the fatigue precrack, is usually used ASTM E 1820 [68].

The above mentioned parameters are usually evaluated using the relevant standard practices, like the well established ASTM E 399 and ASTM E 1820 standard methods [67, 68]. Alternatively, other methods may also be used, like the stretch zone analysis, as a result of the difficulty to obtain valid results of the standard parameters using reasonable specimen sizes [69].

1.14. Evaluation of Dynamic behavior of magnesium alloys

The need for the evaluation of the dynamic properties of the extruded magnesium alloys' powders has arisen after their static behaviors were shown to be promising. It could be shown previously that the powder metallurgy processing has resulted in improved mechanical properties of magnesium alloys. Hence, the need for studying the dynamic performances of the magnesium alloys fabricated by using rapid solidification powder metallurgy has arisen, as it could open a wider market for magnesium alloys.

1.14.1. Experimental investigation of ballistic impact of Mg-alloys

The ballistic impact testing has been used for the evaluation of the dynamic behavior of alloys and structures under high velocities over a range of specimen configurations [70-73]. The fracture behavior was the main emphasis in some of the previous work with various types of projectile configurations [70, 71]. The effect of ballistic impact on the deformed microstructure was also studied for AM60B magnesium alloy at hyper-velocities [72]. The use of magnesium alloys for dynamic applications, which require materials with excellent performances under severe conditions of high strain speeds, has been investigated in the above references. The trials for setting of a standard specification for the use of AZ31 alloy in dynamic applications have resulted in the release of the MIL-DTL-32333 standard in 2009 [74]. This shows the applicability of magnesium alloys in this important field, especially with alloys that have better performances. In this study, the dynamic behavior of extruded magnesium alloy powder was evaluated through the ballistic impact test of alloy plates using a steel ball

with a high speed. The deformation of the specimen after test was used as evaluation criteria.

1.14.2. Simulation of the dynamic behavior using FEM model

The simulation of the ballistic impact test was needed to be able to predict the dynamic responses of the extruded Mg alloys. After performing some preliminary simulation trials using LS-DYNA software, it became clear that it is needed to develop a sound material model that can precisely imitate the mechanical response of the alloy, as the use of other material models resulted in an accuracy that is not acceptable [75].

The coupled experimental and finite element method (FEM) evaluations of mechanical tests have usually been utilized to characterize the local parameters, like stresses and strains, precisely. This is due to the limitations of the experimental measurements to acquire the global information like forces and displacements [76]. The material models available in the LS-DYNA software that have a potential to represent the alloy have been tried. Most of these models are based on the isotropic Mises yield function [77]. However, the alloy characteristics like the anisotropy and the strain rate effect have resulted in the importance of developing a better representative material model, which can take into consideration the most important characteristics of the alloy. Hence, the user defined material model subroutine that was previously developed based on the anisotropic Hill function has been selected for that purpose [78].

An optimization methodology has been used to obtain the material model parameters precisely based on the experimental and simulation results of both the tensile and compression tests. In this process, the experimental results of both tensile and compression tests, as stress-strain date, were used

to calculate the output FEM load-displacement of the simulation. Then those results of both the experimental and FEM analyses were compared, and the difference was used to optimize the data input for simulations until good agreement could be obtained.

Due to the similarity of nature of input and output parameters in both tensile and compression tests, the material model has been verified using the comparison of the experimental and simulation results of bending test. Finally, the simulation of the ballistic impact test was carried out and both the experimental and FEM results were compared together.

1.15. Aim and scope of the current study

The aim of the current study is to investigate the combined effect of both chemical alloying, with Al-Mn-Ca, Al-Zn-Ca-La and Zn-Zr element combinations, and the use of rapidly solidified powder metallurgy on the microstructure, static and dynamic mechanical responses of hot extruded alloys' powders produced using rapid solidification. Those alloys were shown previously, in this chapter, to be developed and produced in their cast forms and to show moderate behaviors. However, the focus in this study is on their behavior when fabricated using the hot extrusion of alloy powders. The alloy powders were first characterizes in their as-received conditions in order to understand their behavior. They were consolidated using different techniques, namely cold compaction and spark plasma centering (SPS), and then hot extruded using different extrusion temperatures for optimization purposes of the conditions.

1.16. Thesis composition

This thesis is composed of 8 chapters, including the current introduction one, as illustrated in the flow chart of Fig. 1.3. The second chapter gives a detailed explanation of the experimental procedures used in this study. In chapter 3, an extensive study on the characteristics of the rapid solidification powders of magnesium alloys are shown and compared to those of the cast alloys. Chapter 4 reveals the microstructures and the evolution of crystallographic textures during hot extrusion of the magnesium alloys. The static mechanical properties of the extruded magnesium alloys via rapid solidification powder metallurgy, including tensile, compression, and hardness properties are introduced in chapter 5. The fracture toughness of extruded magnesium alloys is investigated in chapter 6. The evaluation of the dynamic characteristics of magnesium alloys through the experimental investigation and FEM simulation of the ballistic impact testing of magnesium alloys is shown in chapter 7. In chapter 8, the summary of the entire study, as well as the important conclusions, are revealed.

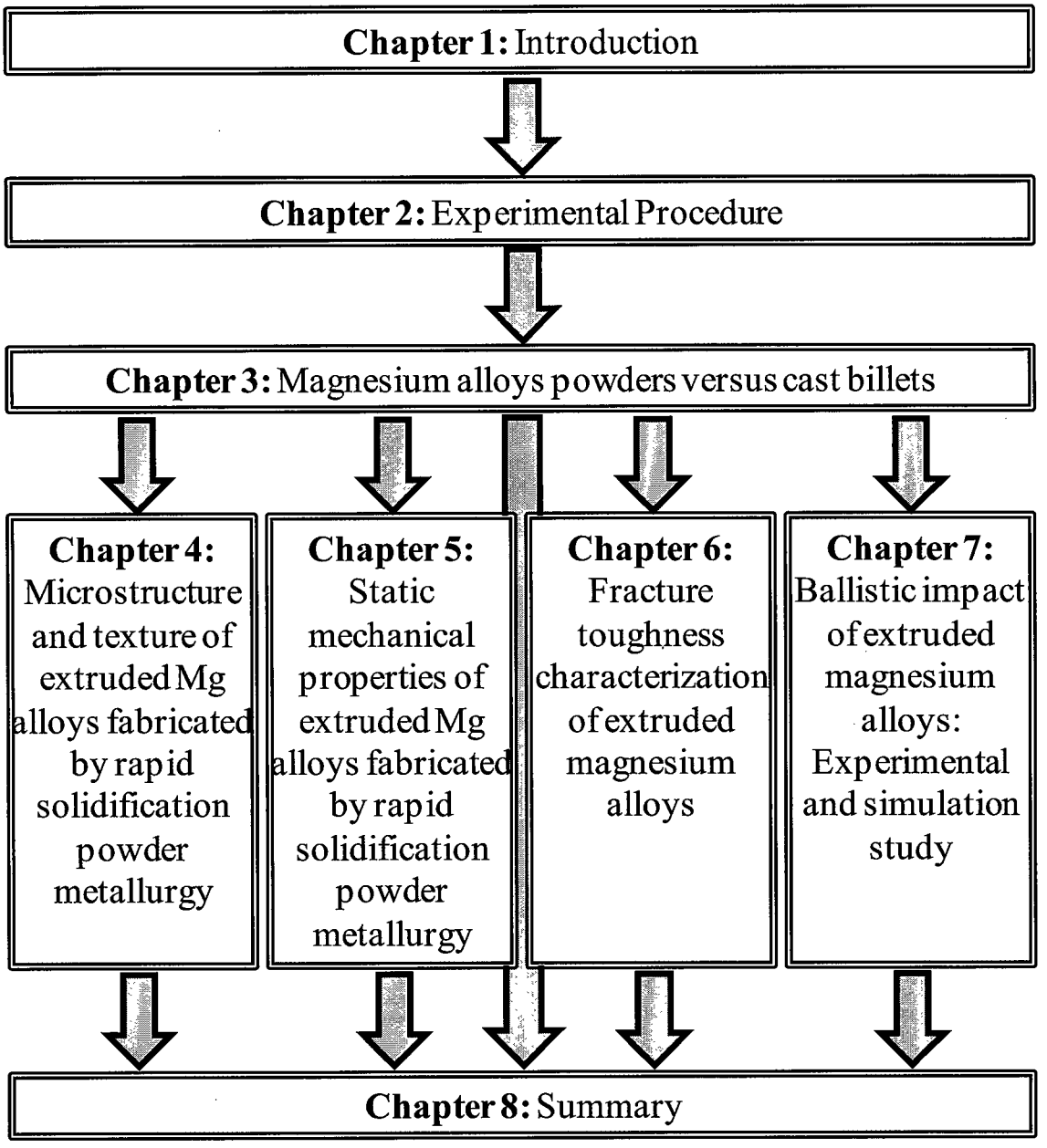

Fig. 1.3 Flaw chart of the current thesis.

References

[1] B.L. Mordike, K.U. Kainer, Magnesium Alloys and Their Applications, Wiley-VCH, Verlag GmbH, Weinheim, 2000.

[2] H.E. Friedrich, B.L. Mordike, Magnesium Technology, Springer-Verlag Berlin Hidelberg, 2006.

[3] Z. Yang, J.P. Li, J.X. Zhang, G.W. Lorimer, J. Robson. Acta Metallurgica Sinica (English Letters), 21 (2008) 313-318.

[4] A. Jain, O. Duygulu, D.W. Brown, C.N. Tome, S.R. Agnew, Materials Scinece and Engineering A, 486 (2008) 545-555.

[5] D.K. Xu, L. Liu, X.B. Xu, E. H. Han, Materials Science and Engineering A, 443 (2007) 248-256.

[6] C. Ma, M. Liu, G. Wu, W. Ding, Y. Zhu, Materials Science and Engineering A, 349 (2003) 207-212.

[7] R.K. Mishra, A.K. Gupta, P.R. Rao, A.K. Sachdev, A.M. Kumar, A.A. Luo. Scripta Materialia, 59 (2008) 562-567.

[8] K. Hantzsche, J. Bohlen, J. Wendt, K.U. Kainer, S.B. Yi, D. Letzig. Scripta Materialia, 63 (2010) 725-730.

[9] N. Stanford, M.R. Barnett. Materials Science and Engineering A, 496(2008) 399-408.

[10] I.A. Anyanwu, Y. Gokan, A. Suzuki, S. Kamado, Y. Kojima, S. Takeda, Materials Science and Engineering A, 380 (2004) 93-99.

[11] N. Balasubramani, M. Suresh, A. Srinivasan, U.T.S. Pillai, B.C. Pai, Journal of Materials Science 42 (2007) 8374-8376.

[12] T. Takenaka, T. Ono, Y. Narazaki, Y. Naka, M. Kawakami, Electrochimica Acta 53 (2007) 117-121.

[13] A. Elsayed, J. Umeda, K. Kondoh, Acta Materialia, 59 (2011) 273-282).

[14] A. Elsayed, H. Imai, J. Umeda, K. Kondoh, Steel Research International, 81-9 (2010) 1304-1307.

[15] Z.B. Sajuri, Y. Miyashita, Y. Hosokai, Y. Mutoh, International Journal of Mechanical Science, 48 (2006) 198-209.

[16] E. Mora, G. Garcez, E. Onorbe, P. Povez, P. Aoleva, Scripta Materialia, 60 (2009) 776-779.

[17] J.M. Dubois, P. Plaindoux, F. Belin, N. Tamura, D.S. Sordelet, Proceeding of Sixth International Conference on Quasicrystals, World Scientific, Singapore, 1997.

[18] X. Zeng, Y. Zhang, C. Lu, Y. Ding, Y. Wang, Y. Zhu, Journal od Alloys and Compounds, 395 (2005) 213-219.

[19] D.K. Xu, W.N. Tang, L. Liu, Y.B. Xu, E.H. Han, Journal of Alloys and Compounds, 461 (2008) 248-252.

[20] B. Kondori, R. Mahmudi, Materials Science and Engineering A, 527 (2010) 2014-2021.

[21] H. Xie, L. Jia, J. Zhang, Z. Wang, Z. Lu, Materials Science and Engineering A, 519 (2009) 204-210.

[22] A. Elsayed, K. Kondoh, H. Imai, J. Umeda, Materials & Design, 31 (2010) 2444-2453.

[23] K. Kondoh, R. Tsuzuki, W. Du, S. Kamado. Journal of Materials Online, 1 (2005) 1-9.

[24] J.T. Wang, D.L. Yin, J.Q. Liu, J. Tao, Y.L. Su, X. Zhao. Scripta Materialia 59 (2008) 63-66.

[25] B.L. Wu, G. Wan, Y.D. Zhang, X.H. Du, F. Wagner, C. Esling, Materials Science and Engineering A, 527 (2010) 3365-3372.

[26] S.X. Ding, W.T. Lee, C.P. Chang, L.H. Chang, P.W. Kao, Scripta Materialia, 59(2008) 1006-1009.

[27] X.S. Wang, L. Jin, Y. Li, X.W. Guo, Materials Letters, 62 (2008) 1856-1858.

[28] P. Andersson, C. Caceres, J. Koike, Materials Science Forum 419-422 (2003) 123-128.

[29] H. Ding, L. Liu, S. Kamado, W. Ding, Y. Kojima, Journal of Alloys and Compounds, 456 (2008) 400-405.

[30] T. Mukai, K. Higashi, Scripta Materialia, 244(2001) 1493-1498.

[31] J.Q. Li, L. Wang, H.W. Cheng, H.F. Zhang, Z.Q. Hu, H.N. Cai, Materials Science and Engineering A, 474 (2008) 24-29.

[32] G. Garcez, M. Maeso, I. Todd, P. Perez, P. Adeva, Journal of Alloys and Compounds 432 (2007) 10-14.

[33] Y. Kawamura, A. Inoue, Materials Science Forum, 419-422 (2003) 709-714.

[34] Z.M. Zhang, C.J. Xu, X.F. Guo, Acta Metallurgica Sinica (English Letters) 21 (2008) 30-36.

[35] K. Kondoh, A. Elsayed, H. Imai, J. Umeda, T. Jones, Materials & Design, 31 (2009) 1540-1546.

[36] J. Cai, G.C. Ma, Z. Liu, H.F. Zhang, A.M. Wang, Z.Q. Hu, Materials Science and Engineering A, 456 (2007) 364-367.

[37] H. Imai, M. Kawakami, K. Kondoh, I. Otsuka, H. Izaki, Transactions of JWRI 36-2 (2007) 33-38.

[38] S.S. Ding, C. Ding, C.Z. Hua, Journal of Alloys and Compounds 470 (2009) 17-20.

[39] T. Homma, N. Kunito, S. Kamado, Scripta Materialia 61 (2009) 644-647.

[40] S.M. He, X.Q. Zeng, L.M. Peng, X. Gao, J.F. Nie, W.J. Ding, Journal of Alloys and Compounds 427 (2007) 316-323.

[41] T. Itoi, K. Takahashi, H. Moriyama, M. Hirohashi, Scripta Materialia, 59 (2008) 1155-1162.

[42] S.X. Ding, W.T. Lee, C.P. Chang, L.W. Chang, P.W. Kao, Scripta Materialia, 59 (2008) 1006-1009.

[43] T. Honma, K. Nagai, A. Katou, K. Arai, M. Suganuma, S. Kamado, Scripta Materialia, 60 (2009)451-454.

[44] W.N. Wang, J.C. Huang JC, Materials Chemistry and Physics, 81 (2003) 11-26.

[45] M. Shahzad, L. Wagner, Materials Science and Engineering A, 506 (2009) 141-147.

[46] H. Ding, L. Liu, S. Kamado, W. Ding, Y. Kojima, Journal of alloys and compounds, 456 (2008) 400-406.

[47] N.V.R. Kumar, J.J. Blandin, C. Desrayaud, F. Montheillet, M. Suery, Materials Science and Engineering A, 359 (2003)150-157.

[48] L.L. Chang, Y.N. Wang, X. Zhao, M. Qi, Materials Characterization, 60 (2009) 991-994.

[49] T. Al-Shamman, X. Li, S.G. Chowdhury, Materials Science and Engineering A, 527 (2010) 3450-3463.

[50] E. Martin, J. Jonas, Acta Materialia, 58 (2010) 4253-4266.

[51] A.S. Varzaneh, A. Hanzaki, H. Beladi, Materials Science and Engineering A, 456 (2007) 52-57.

[52] J. Bohlen, S. Yi, D. Letzig, K.U. Kainer, Materials Science and Engineering A, 527 (2010) 7092-7098.

[53] J. Bohlen, M.R. Nurnberg, J.W. Senn, D. Letzig, S.R. Agnew, Acta Materialia, 55 (2007) 2101-2112.

[54] N. Stanford, M.R. Barnett, Materials Science and Engineering A, 496 (2008) 399-408.

[55] B.L. Wu, Y.H. Zhao, X.H. Du, Y.D. Zhang, F. Wagner, C. Esling, Materials Science and Engineering A, 527 (2010) 4334-4340.

[56] N. Stanford, Materials Science and Engineering A, 527 (2010) 2669-2677.

[57] N. Stanford, M. Barnett, Scripta Materialia, 58 (2008) 179-182.

[58] N. Stanford, D. Atwell, A. Beer, C. Davies, M.R. Barnett, Scripta Materialia, 59 (2008) 772-775.

[59] T. Laser, C. Hartig, M.R. Nurnberg, D. Letzig, R. Bormann, Acta Materialia, 56 (2008) 2791-2798.

[60] T. Mukai, M. Yamanoi, H. Watanabe, K. Higashi, Scripta Materialia, 45 (2001) 89-94.

[61] D.L. Yin, J.T. Wang, J.Q. Liu, X. Zhao, Journal of Alloys and Compounds, 478 (2009) 789-795.

[62] J. Bohlen, S.B. Yi, J. Swiostek, D. Letzig, H.G. Brokmeier, K.U. Kainer, Scripta Materialia, 53 (2005) 259-264.

[63] E.A. Ball, P.B. Prangnell, Scripta Metallurgica et. Materialia, 31 (1994) 111-116.

[64] S.S. Park, B.S. You, D.J. Yoon, Journal of Materials Processing Technology, 209 (2009) 5940-2943.

[65] N. Perez, Fracture Mechanics, Kluwer Academic Publishers, Bosto, 2004.

[66] T. L. Anderson, Fracture Mechanics Fundamentals and Applications, CRC Press, California, 1995.

[67] ASTM E 399, Standard test method for plane-strain fracture toughness of metallic materials, ASTA International, West Conshohocken, PA, 2001.

[68] ASTM E 1820, Standard test method for measurement of fracture toughness, ASTA International, West Conshohocken, PA, 2001.

[69] S. Barbagello, E. Cerri, Engineering Failure Analysis, 11 (2004) 127-140.

[70] D. Hwang, A. Hashimoto, D. Numata, T. Kikuchi, K. Takayama: Key Rngineering Materials 3221-323 (2006) 654-657.

[71] T. Jones, R. Delorme, M. Burkins, W. Gooch: 23rd International Symposium on Ballistics, Tarragona, Spain 16-20 April 2007.

[72] D.L. Zou, L. Zhen, Y. Zhu, C.Y. Xu, W.Z. Shao, B.J. Pang: Materials Science and Engineering A 527 (2010) 3323-3328.

[73] J.C.F. Millett, S.M. Stirk, N.K. Bourne, G.T. Gray III: Acta Materialia 58 (2010) 5675-5682

[74] MIL-DTL-32333, Detail Specification Armor Plate, Magnesium Alloy, AZ31B, Applique, U.S. Army Research Laboratory, 2009.

[75] A. Elsayed, K. Kondoh, N. Ma, Proceeding of the Visual-JW2010, Osaka, 2010.

[76] M. Springmann, M. Kuna: Computational Materials Science 32 (2005) 544-552.

[77] LS-DYNA users manual.

[78] Ninshu MA: User's manual of a general anisotropic material model, JSOL Corporation, 2006

Chapter 2 Experimental procedure

2.1. Cast alloys and powders

Four magnesium alloys have been investigated in this study, which have the chemical compositions listed in Table 2.1. The naming pattern follows the standard practice of having the letters of main alloying elements followed by numbers representing their average percentages. For example, "A", "M", "X" and "E" means Al, Mn, Ca and rare earth elements, respectively. In the present study, La element was used as a rare earth element. Those alloys have been previously shown to have good mechanical properties in their cast form. However, the focus in this study is on their performance when fabricated via rapid solidification powder metallurgy. AMX602 alloy is a standard AM-series' alloy with the addition of Ca to improve the combustibility and high temperature properties [1, 2]. Both ZAXE1713 and ZAXE1711 alloys contain Ca and La additions as it is now well established that rare earth additions could improve the properties of Mg alloys through their effects of weakening texture, grain refinement, and increasing creep and corrosion resistances [3-6]. The ZK61 alloy is a standard alloy that contains zirconium and is extensively used as a cast alloy [7].

Table 2.1 Chemical compositions of Mg alloys investigated in this study (wt. %).

Alloy	Al	Mn	Zn	Ca	La	Zr	Mg
AMX602	6.01	0.26	0.01	2.09	-	-	Bal.
ZAXE1713	7.20	0.01	0.98	1.12	3.34	-	Bal.
ZAXE1711	6.99	0.01	0.99	1.04	1.54	-	Bal.
ZK61	0.01	0.01	5.21	-	-	0.34	Bal.

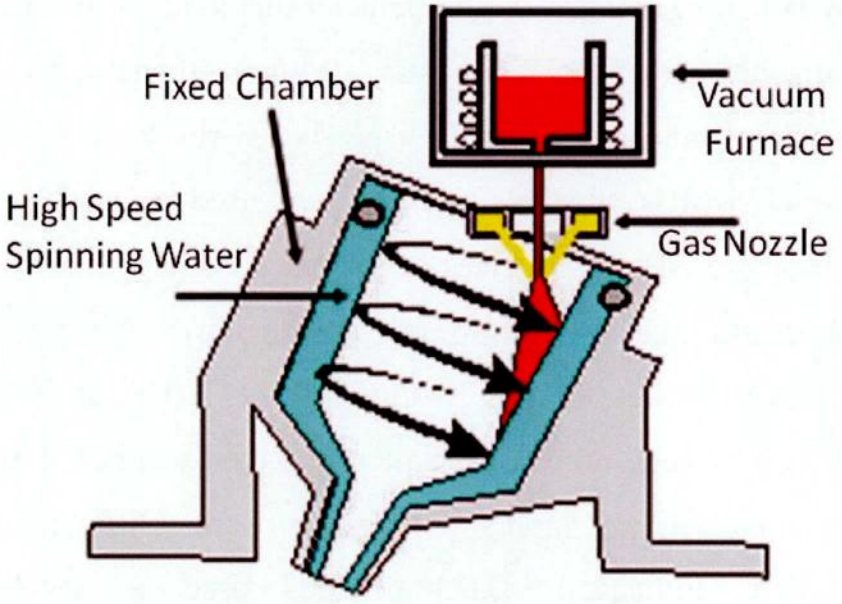

Fig. 2.1 Schematic representation for the SWAP process used to produce magnesium powders.

The cast alloys have been atomized to prepare the powders used as raw materials in the study using the spinning water atomization process (SWAP) [8]. In this process, schematically represented in Fig. 2.1, gas atomization is combined with water atomization to produce super high cooling rates of about 10^6 K/s, which result in relatively coarse powders with very fine microstructures and a super-saturation of the alloying elements [9].

2.2. Powder characterization

Microstructure analysis of the SWAP powders, cast billets, and the extruded bars was performed using both optical microscope and Scanning Electron Microscope (SEM, JEOL: JSM-6500F) because of the fine grain size of less than 1 μm. Prior to observation, the surface was prepared by grinding with successive mesh sizes of emery papers until 4000 grit,

followed by polishing using 0.25 μm diameter diamond paste, and etching in acetic-picral solution (1.5 gm Picric acid, 10 ml Acetic acid, 10 ml distilled water, and 25 ml ethanol). Energy Dispersive X-ray Spectroscopy (EDS, JEOL: EX-64175JMU) attached to SEM was used to analyze the inter-metallic compounds. The grain sizes of the extruded Mg alloy bars, as well as the dendrite arm spacing (DAS) of raw powders, were evaluated using the image analysis software (Image-Pro Plus 4.0.0.11). The grain boundaries were first traced by hand on tracing papers, and then scanned as image files, which were then used as inputs for that software. Differential Thermal Analysis (DTA, Shimadzu: DTG-60) was used to investigate the metallurgical transformations of both SWAP powder and cast material during thermal processing. The analysis was performed while heating each sample of about 18 mg of powder referred to 30 mg of alumina, as reference material, in an Ar gas atmosphere using the heating rate of 10 K/min. X-ray Diffraction (XRD) analysis was used to investigate the phases existing in both SWAP powder and cast material using an X-ray Diffractometer (Shimadzu: XRD 6100) over a range of 2θ of 20 to 80°.

In order to investigate about the effect of thermal processing on the metallurgical aspects of the SWAP powders, high temperature XRD analysis was performed at the range of temperatures of 573 to 823 K in Ar gas atmosphere over the range of 2θ of 30 to 50°. Annealing of the SWAP powder was also performed to see the microstructural changes after annealing, which helps to understand the microstructural evolution during thermo-mechanical processing (consolidation and extrusion). After annealing, the microstructure and the XRD analysis were obtained for the annealed powders.

2.3. Consolidation of powders and hot extrusion

As-received SWAP powders were consolidated using two different techniques, namely cold compaction and spark plasma sintering (SPS, Sumitomo Coal Mining: SPS-1030). In cold compaction, 60 g of powder was compacted in a 42 mm diameter steel mold at room temperature using a pressure of 600 MPa, as illustrated in Fig. 2.2. On the other hand, SPS was carried out on the same amount of powder and same size of carbon mold at various temperatures in the range of 473 to 673 K in vacuum under the pressure of 30 MPa, as illustrated in Fig. 2.3. Heating was done at a rate of 10 K/min followed by holding at the sintering temperature for 1.8 ks. SPS was used for the consolidation of the powders to achieve its advantages of the improved metallurgical bonding strength between powder particles, which is a very critical factor in determining the mechanical properties of extruded bars, as well as for its minimized grain growth compared to the conventional sintering [10]. Both cast billets and consolidated powder billets via cold compaction or SPS process were extruded using the 2000 KN hydraulic press machine at temperatures in the range of 523 to 673 K, as illustrated in Fig. 2.4. Extrusion was performed using a die that produces extrusion rods of 7 mm, which is equivalent to an extrusion ratio of about 37. The preheating of billets was carried out just before extrusion using a heating rate of 1 K/s in Ar gas atmosphere. The billets were held at the extrusion temperature in the furnace for 5 min prior to extrusion to ensure homogenous temperature distribution. Both the extrusion container and the die were also preheated to the extrusion temperature to keep the temperature of the billet homogenous during the extrusion process.

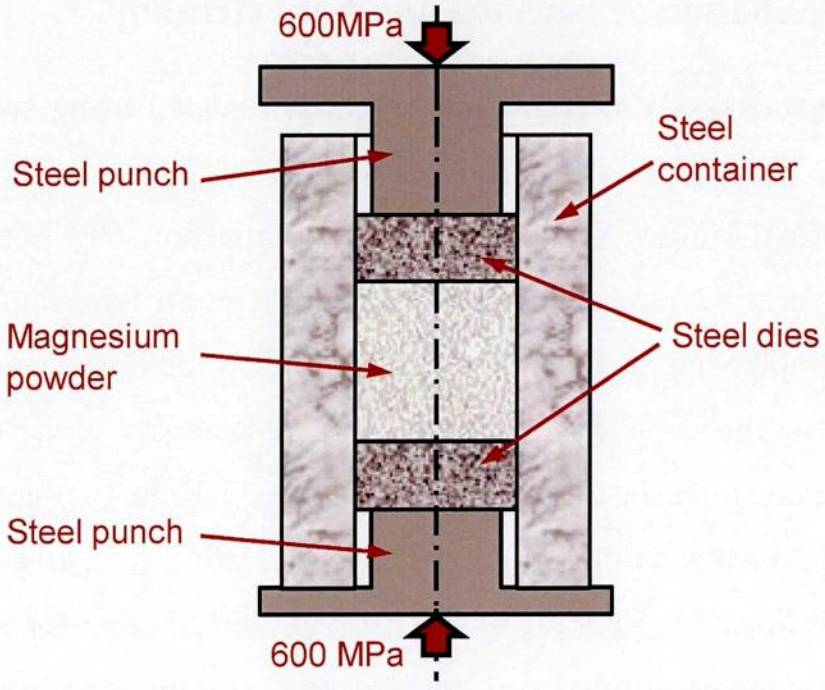

Fig. 2.2 Schematic illustration of the cold compaction process.

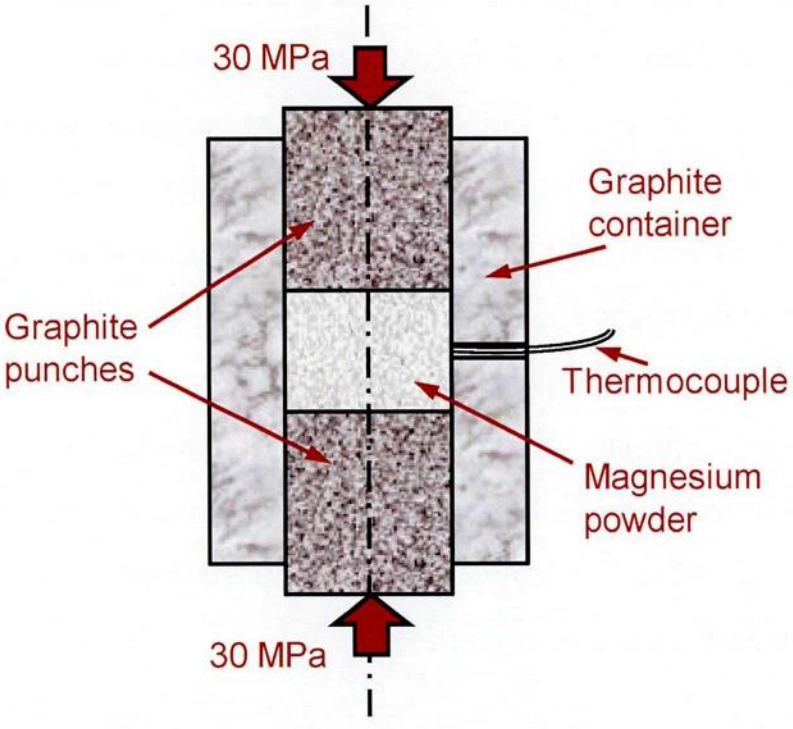

Fig. 2.3 Schematic illustration of the spark plasma sintering process.

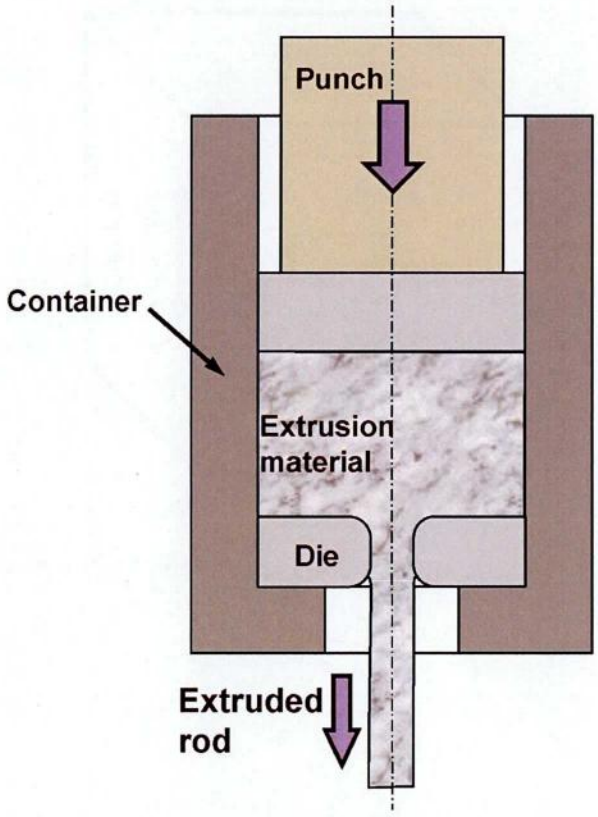

Fig. 2.4 Extrusion process setup.

2.4. Texture analysis by EBSD

The texture evolution in the extruded bars was investigated using the electron back-scattered diffraction (EBSD) analysis. The specimens for EBSD investigation were cut from the 25 x 40 mm cross-section extruded bars such that the observation plane is parallel to the extrusion direction at midway between the surface and the center of the extruded rod, as shown in Fig. 2.5. Those larger sizes of extrusion rods were prepared to enable the extraction of tensile and compression specimens at various orientation to investigate the anisotropy. The specimen surface was prepared by grinding until 4000 grit emery paper, polishing using 0.25 μm diamond paste, electro-chemical etching using (37.5 vol.% H_3PO_4 + 62.5 vol.% ethanol) solution with 5 V for 60 s, and then cleaning using methanol. Texture parameters like

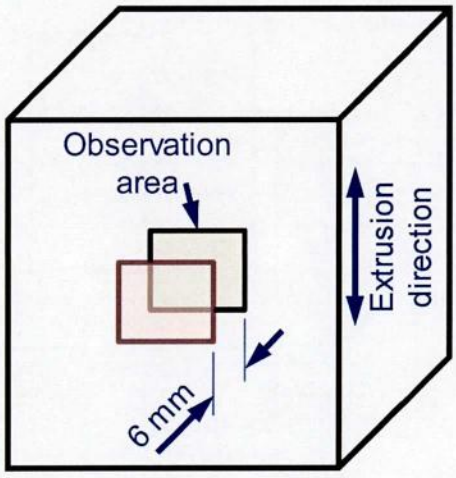

Fig. 2.5 Schematic representation of the EBSD observation area on the extruded rod.

the maximum intensity of the basal plane (0001) texture and the average Schmid factor [11], as well as the average grain size, have been obtained for the investigated specimens. The data points with quality index lower than 0.05 have been removed from the analysis.

2.5. Mechanical properties evaluation

Hardness tests were carried out using a Micro Vickers tester (Shimadzu: HMV-2T) with a test load of 0.491 N. Tensile, compression and bending tests were performed using a universal testing machine (Shimadzu: Autograph AG-X 50 KN) at room temperature on three test specimens for each material and processing condition, and the average of the three values was introduced. The tensile test specimens, having the diameter of 3 mm, the reduced length of 15 mm, and the gage length of 12 mm, were evaluated using a strain rate of $5x10^{-4}$ /s. The same strain rate was also used to evaluate the compression test specimens which had the diameter of 6 mm and the

length of 15 mm. On the other hand, 3-point bending tests were performed on 3 x 4 mm rectangular cross section specimen with 20 mm span between supporting rollers.

For both AMX602 and ZAXE1711 alloys, their anisotropy has been investigated by obtaining tensile and compression tests at various angles from the extrusion direction [12], namely 0, 45 and 90°. For the purpose of obtaining those specimens, bigger size extrusion bars have been prepared which have a rectangular cross-section with the dimensions of 25 x 40 mm using the same preparation conditions used for smaller size rods, except for increasing the homogenization temperature to 60 min.

Fracture toughness tests were performed at room temperature on 3-point bending test specimens, having straight through notch, according to both ASTM E 399 and ASTM E 1820 standards [13, 14]. The thickness, width and span of the specimens were 8, 16, and 64 mm respectively, while the total length was 68 mm, as shown in Fig. 2.6. The specimens were machined from the extruded bars so that the plane of the machined notch is normal to the extrusion direction. The integral knife edges were set up at the crack mouth to enable the use of a double cantilever clip-in displacement gage to measure the crack opening displacement (COD) during test. Fatigue pre-cracks were developed in the specimens using a sinusoidal loading with a maximum load of 900 N, a load ratio of 0.1 and a frequency of 20 cps using a servo-hydraulic axial fatigue testing machine (Shimadzu: Servopulser E100KN). The ratio of the fatigue pre-crack length to the specimen width was set to 0.5 for all specimens. The final fracture stage of the fracture toughness test was carried out using stroke control on the above mentioned tensile testing machine with the loading rate of 0.0125 mm/s, which corresponds to the rate of increase of stress intensity factor of 0.75 MPa $m^{1/2}$ /s. The test continues until the specimen could sustain no further

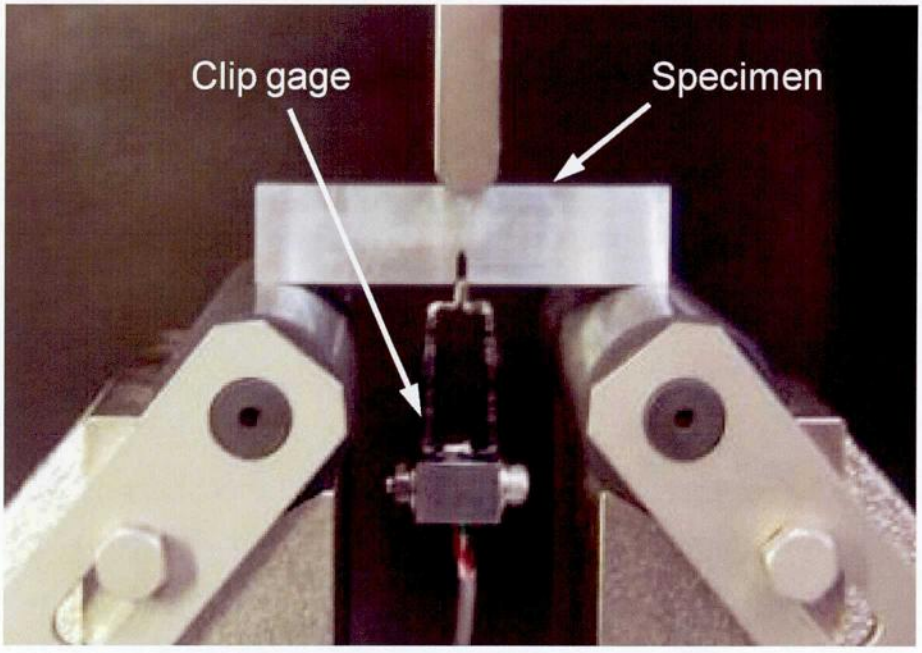

Fig. 2.6 Fracture toughness test specimen and setup.

increase in load, which corresponds to the onset of crack propagation. The load versus crack opening displacement, measured using the knife edge displacement gage placed at the crack mouth, was recorded during test and later was used to evaluate the fracture toughness parameters. Details of test procedure and equations used to calculate the fracture parameters can be seen in the relevant ASTM E 399 and ASTM E 1820 standards. Three specimens for each condition were machined and the average values were introduced.

Ballistic impact tests were performed to evaluate the dynamic behavior of magnesium alloys using the 6 mm diameter steel ball launched against the magnesium plate specimen using the compressed air, as shown in Fig. 2.7. The disk-shaped test specimens had the diameter of 38 mm and the thickness of 3 mm. The ball hits the specimen with an average speed of 140 m/s, measured using an optical speed sensor. After impact, the specimens

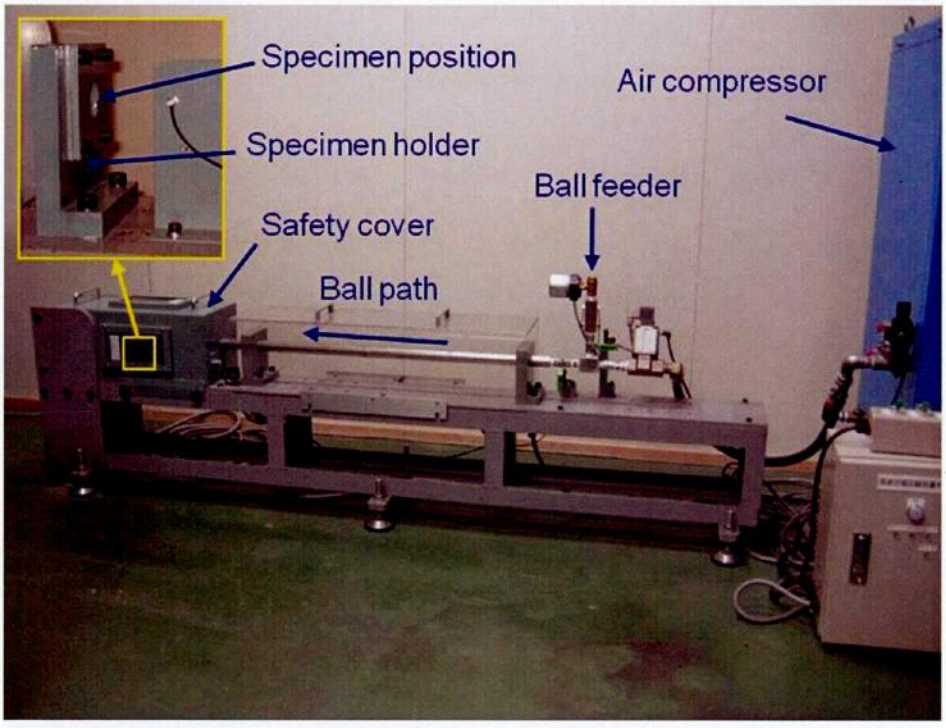

Fig. 2.7 Ballistic impact test specimen and setup.

were investigated whether it suffered a fracture, then the front indentations and the back protrusions were measured and evaluated as signs of dynamic damage.

2.6. Models for mechanical tests

To model the static and dynamic behaviors of the investigated alloys, FEM models have been setup on the LS-DYNA program with a user defined subroutine as the material model. Ultimately, the prediction of the ballistic impact behavior was required and the proper material model that imitates the original alloy properties needed to be selected. Hence, several other simulations were primarily setup to select the proper material model and to

accurately verify its parameters, including tensile, compression and bending test simulations.

The investigated alloys have shown anisotropic mechanical behaviors. The ultimate stresses and fracture strains of the investigated alloys had different values at different directions and in different stress states such as tension and compression. To express these anisotropic yield phenomena, Hill anisotropic yield function defined by the following equation is selected [15].

$$\sqrt{F(\sigma_{22}-\sigma_{33})^2+G(\sigma_{33}-\sigma_{11})^2+H(\sigma_{11}-\sigma_{22})^2+2L\sigma_{23}^{\ 2}+2M\sigma_{31}^{\ 2}+2N\sigma_{12}^{\ 2}}=\sigma_Y$$

where, F, G, H, L, M, N are coefficients which can be determined by 6 initial yield stresses σ_{Y11}, σ_{Y22}, σ_{Y33}, σ_{Y12}, σ_{Y23}, and σ_{Y31} using following Equations.

$$F=\frac{1}{2}[(\frac{\sigma_{Y11}}{\sigma_{Y22}})^2+(\frac{\sigma_{Y11}}{\sigma_{Y33}})^2-1],\quad G=\frac{1}{2}[(\frac{\sigma_{Y11}}{\sigma_{Y33}})^2+1-(\frac{\sigma_{Y11}}{\sigma_{Y22}})^2]$$

$$H=\frac{1}{2}[1+(\frac{\sigma_{Y11}}{\sigma_{Y22}})^2-(\frac{\sigma_{Y11}}{\sigma_{Y33}})^2],$$

$$L=\frac{1}{2}(\frac{\sigma_{Y11}}{\sigma_{Y23}})^2,\quad M=\frac{1}{2}(\frac{\sigma_{Y11}}{\sigma_{Y31}})^2,\quad N=\frac{1}{2}(\frac{\sigma_{Y11}}{\sigma_{Y12}})^2$$

If F=G=H=1/2 and L=M=N=3/2, the yield function is just the same with isotropic Misses yield function. Figure 2.8 shows the initial yield surfaces if the ratio $\sigma_{Y11}/\ \sigma_{Y22}$ of yield stress σ_{Y11} in the extrusion direction and yield stress σ_{Y22} in the transverse direction is assumed to be 1, 2, 3 and 4. For modeling the effect of tensile and compressive stress states on yield surface and fracture criteria, a material model considering the anisotropic stress strain relations shown in Fig.2.8 was developed by authors and implemented to LS-DYNA through a customized user subroutine [3]. In this developed material model, the effects of strain rate on Young's modulus,

plastic work hardening and fracture strains are also included. Figure 2.9 reveals the geometrical representation of simulation models which show the mesh distribution. While both the tensile and compression test specimens were modeled using two-dimensional axi-symmetrical shell elements, the three-dimensional block elements were employed for modeling of both bending and ballistic impact specimens.

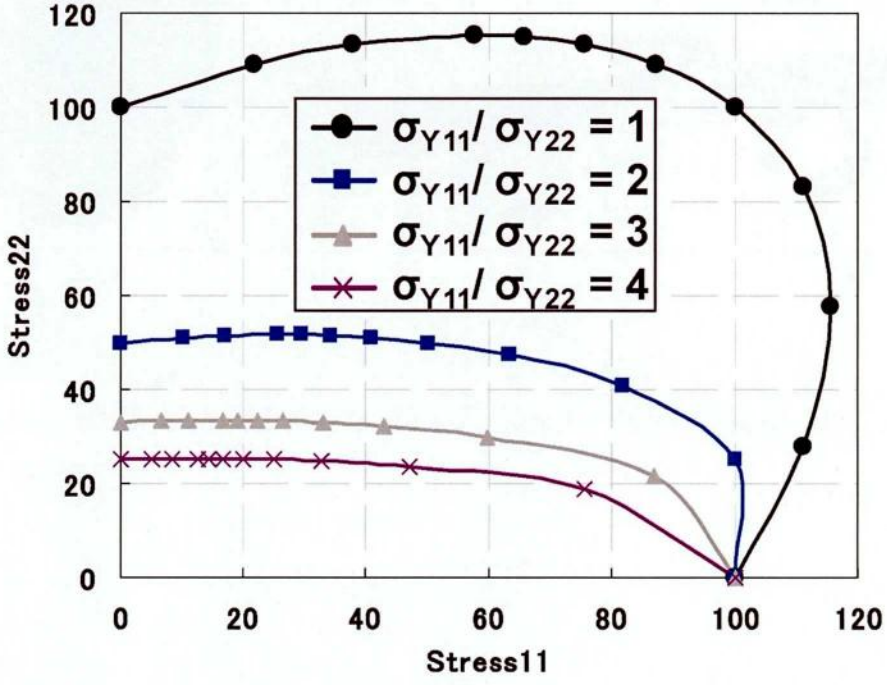

Fig. 2.8 Initial yield surfaces at various yield stress ratios for the anisotropic material model.

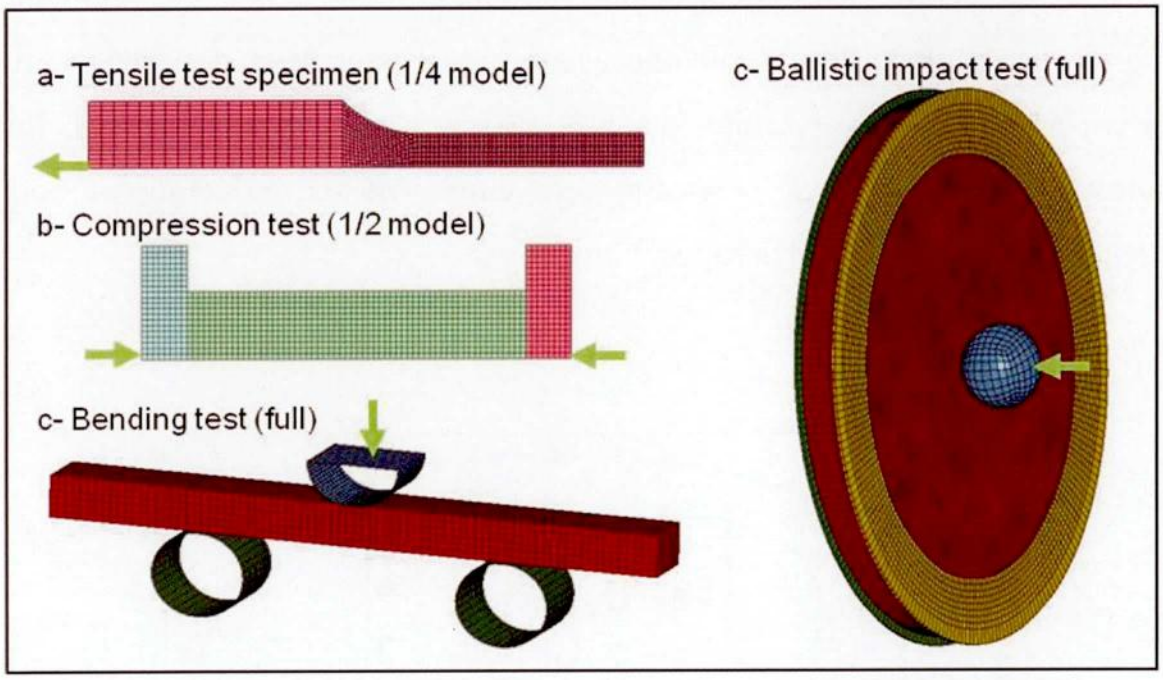

Fig. 2.9 Models for FEM analyses showing the mesh distribution.

References

[1] B. Kondori, R. Mahmudi, Materials Science and Engineering A, 527 (2010) 2014-2021.

[2] H. Xie, L. Jia, J. Zhang, Z. Wang, Z. Lu, Materials Science and Engineering A, 519 (2009) 204-210.

[3] R.K. Mishra, A.K. Gupta, P.R. Rao, A.K. Sachdev, A.M. Kumar, A.A. Luo, Scripta Materialia, 59 (2008) 562-565.

[4] K. Hantzsche, J. Bohlen, J. Wendt, K.U. Kainer, S.B. Yi, D. Letzig, Scripta Materialia, 63-7 (2010) 725-730.

[5] I.A. Anyanwu, Y. Gokan, A. Suzuki, S. Kamado, Y. Kojima, S. Takeda, Materials Science and Engineering A, 380 (2004) 93-99.

[6] T. Takenaka, T. Ono, Y. Narazaki, Y. Naka, M. Kawakami, Electrochemica Acta, 53 (2007) 117-122.

[7] M. Shahzad, L. Wagner, Scripta Materialia, 60 (2009) 536-538.

[8] A. Elsayed, K. Kondoh, H. Imai, J. Umeda, Materials & Design, 31 (2010) 2444-2453.

[9]A. Elsayed, J. Umeda, K. Kondoh, Acta Materialia, 59 (2011) 273-282.

[10] C. Wang, X. Wang, Z. Zhang, Journal of the European Ceramic Society, 31 (2011) 231-235.

[11] Z. Zeng, X. Zhang, S. Jonsson, Materials Science and Engineering A, 513-514 (2009) 83-90.

[12] A. Elsayed, J. Umeda, K. Kondoh, TMS2011 Annual Meeting & Exhibition February 27-March 3 2011, San Diego, California, USA.

[13] ASTM E399: Standard Test Method for Plane-Strain Fracture Toughness of Metallic Materials, ASTM, West Conshohocken, PA, 1999.

[14] ASTM E1820: Standard Test Method for Measurement of Fracture Toughness, ASTM, West Conshohocken, PA, 1999.

[15] Ninshu MA, User's manual of a general anisotropic material model, JSOL Corporation, 2006.

Chapter 3 Magnesium alloys powders versus cast billets

In this chapter, the microstructural features of the investigated alloys in their powder and cast forms are discussed. The XRD and EDS analyses were also used to identify the intermetallic compounds. Furthermore, the effect of thermo-mechanical processing on the microstructure of the alloys has also been investigated through performing the annealing heat treatment at temperatures similar to those used during both consolidation and the extrusion. It should be noted that both ZAXE1711 and ZAXE1713 alloys have shown very similar microstructure and intermetallic compound formation behaviors, due to the effect of supersaturation by the rapid solidification [1]. However, the extruded bars of those alloys have shown different behaviors from each other, shown in chapters 4 and 5, which provide information about the effect of alloying with La. Therefore, only one alloy among both, ZAXE1711 alloy was selected to be shown in this chapter.

3.1. Microstructure of SWAP powders and cast billets

3.1.1. Microstructure of AMX602 alloy SWAP powder and cast billet

The SWAP powder of AMX602 alloy has shown an average particle size of 1.1 mm, which is considerably coarse and ensures safe handling. The optical microstructures of both SWAP powder and cast AMX602 alloy are shown in Fig. 3.1. For SWAP powder in Fig. 3.1 (a), the directional solidification in terms of fine dendrite structures of α-Mg grains can be observed, as a result of the high solidification rate of SWAP process [2, 3], which also has resulted in the intermetallic compound-free structure due to

the supersaturation of alloying elements via rapid solidification process [4]. This fine microstructure has resulted in the hardness value of 85 Hv. The supersaturation of alloying elements reduces the formation of coarse inter-metallic compounds, especially in the case of low solubility alloying elements, leading to improved mechanical response [5]. The dendrite arm spacing (DAS) has shown considerable dependence on the powder particle size, and had an average of about 1.37 μm. This value could be used to calculate the solidification rate using the following equation [6], where R denotes the solidification rate, which showed the value of 3.6×10^4 K/s. This value of the solidification rate is much higher than that of the conventional solidification of cast alloys.

$$DAS = 35.5R^{-0.31}$$

For the cast billet, the hardness has much lower value of 55.4 Hv, due to the much higher grain size of 94 microns compared to that of SWAP powders, as shown in Fig. 3.1 (b). The main constituent of the microstructure of the cast alloy is also the α-Mg grains with an intermetallic compounds precipitated at the grain boundaries, which are later identified.

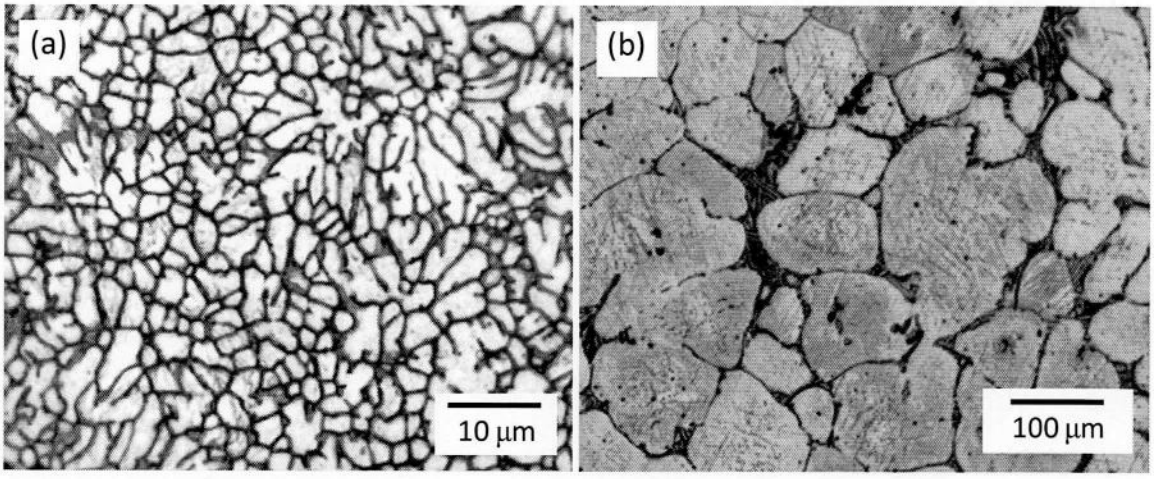

Fig. 3.1 Microstructures of AMX602 SWAP powder (a) and cast ingot (b).

3.1.2. Microstructure of ZAXE1711 alloy SWAP powder and cast billet

The aforementioned features of the microstructures of SWAP powder and cast billet of AMX602 alloy could also be found in both ZAXE1711 and ZAXE1713 alloys. The microstructures of ZAXE1711 alloy are shown in Fig. 3.2. The SWAP powder particles of this alloy showed finer sizes of dendrite arm spacing than those of AMX602 alloy. They showed the value of 0.91 μm for particle sizes below 100 μm, while it showed 2.03 μm for particle sizes over 1 mm with the corresponding hardness values of 99 and 87 Hv, respectively. These values of DAS correspond to the values of cooling rates of $1.36x10^5$ and $1.02x10^4$ K/s, respectively according to the above mentioned equation. No precipitation of compounds could be observed in SWAP powders, as could be shown in Fig. 3.2 (a), which is also a direct consequence of the high solidification rate. On the other hand, the intermetallic compounds with flakes shape distributed in the matrix of α-Mg were observed in the cast alloy shown in Fig. 3.2 (b). They differ from that of AMX602 cast alloy of Fig. 3.1 (b) in that they exist as separate islands. However, they have similar sizes compared to each other. The ZAXE1713 alloy, which differs only in the La percentage, has also shown a microstructure similar to that of ZAXE1711 alloy.

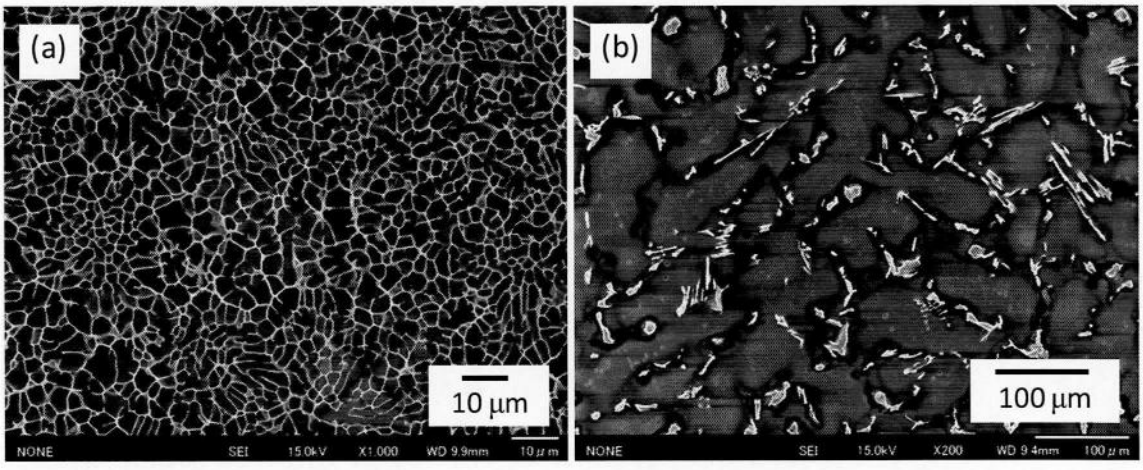

Fig. 3.2 Microstructures of ZAXE1711 alloy SWAP powder (a) and cast ingot (b).

3.1.3. Microstructure of atomized ZK61 alloy powder

The atomized ZK61 alloy powder has shown very homogeneous sizes of powder particles with a completely spherical morphology, as shown in Fig. 3.3 (a). It has shown a microstructure similar to that of SWAP powders of the other alloys. However, the DAS of the alloy powder has shown bigger values, as shown in Fig. 3.3 (b), due to its lower cooling rate in atomization compared to that of SWAP. The DAS value of 3.2 µm corresponded to the cooling rate of 2.35 x 10^3 K/s. The lower cooling rate results from the fact that only gas atomization was used in the fabrication process of this powder. This ultimately resulted in the formation of intermetallic compound-precipitated areas along the grain boundaries of the powder, unlike to the fact that the SWAP powder is free from these compounds because of their high solidification rates.

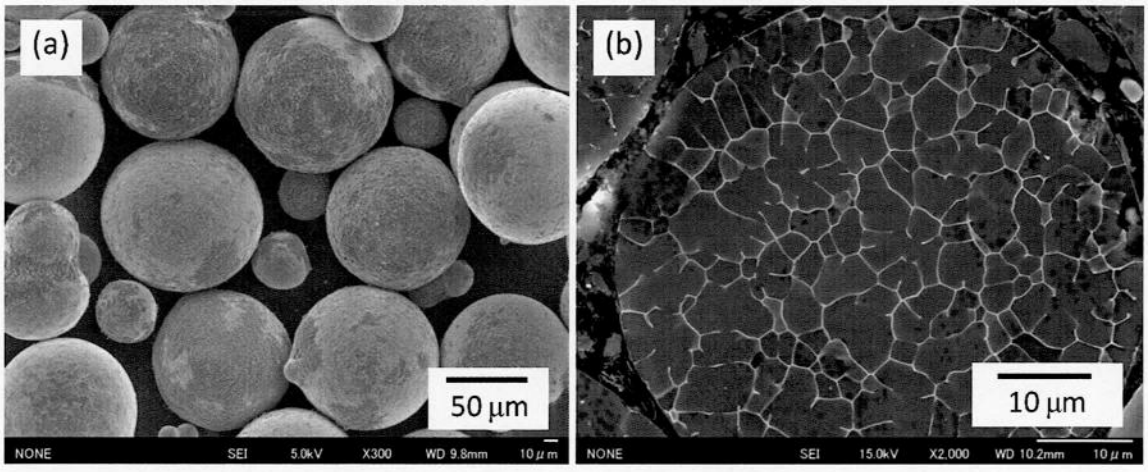

Fig. 3.3 SEM photos of ZK61 alloy atomized powers (a) and their microstructure (b).

3.2. Intermetallic compound investigation

Generally, the SWAP powders revealed no sign of the intermetallic compound formation due to high solidification rate of that process. However, the cast alloys, as well as the atomized ZK61 alloy powder, indicated some intermetallic compounds, which were investigated herein.

3.2.1. Intermetallic compounds of cast AMX602 alloy

The cast AMX602 alloy showed an intermetallic compound at the α-Mg grain boundaries, which was identified as Al_2Ca using the XRD analysis, as shown in Fig. 3.4. Peaks of this compound were detected along with those of α-Mg matrix. Peaks of Bakelite used for fixing the test samples could also be observed in the figure. It was confirmed from this figure that the SWAP powder of AMX602 alloy was free from intermetallic compounds, as stated above.

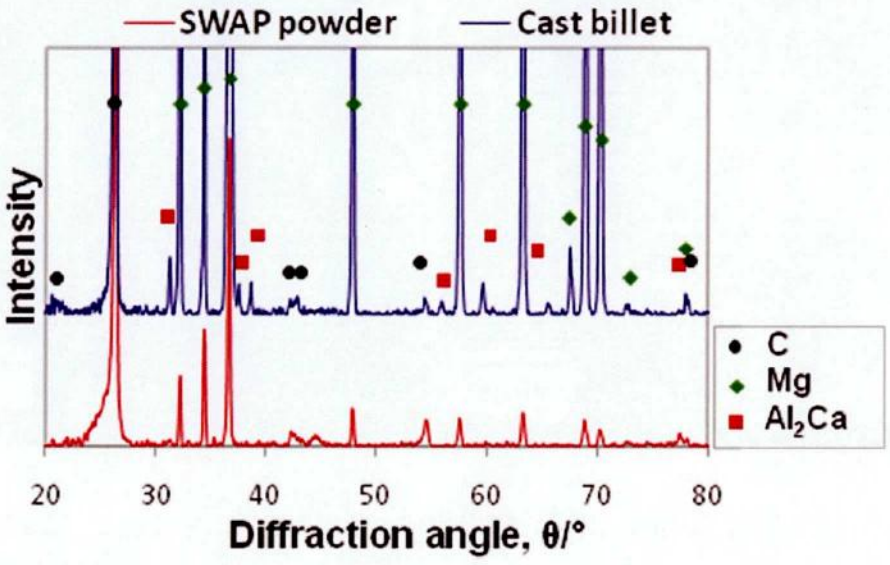

Fig. 3.4 XRD patterns of AMX602 alloy SWAP powder and cast.

The morphology of this intermetallic compound was observed in the EDS pattern of the cast alloy shown in Fig. 3.5. The Al_2Ca intermetallic compound particles showed a network structure of closely packed columnar morphologies, like Chinese characters. Another type of intermetallic compounds with a different morphology can also be observed. Very tiny spherical particle that contains both Al and Mn can be detected, which was then identified as Al_6Mn. This compound could not be detected using the XRD pattern of the cast alloy, as shown in Fig. 3.4, due to its tiny morphology and very small content in the structure. The above results confirmed the effect of rapid solidification of SWAP powders for the supersaturation of the alloying elements such as Al, Ca and Mn.

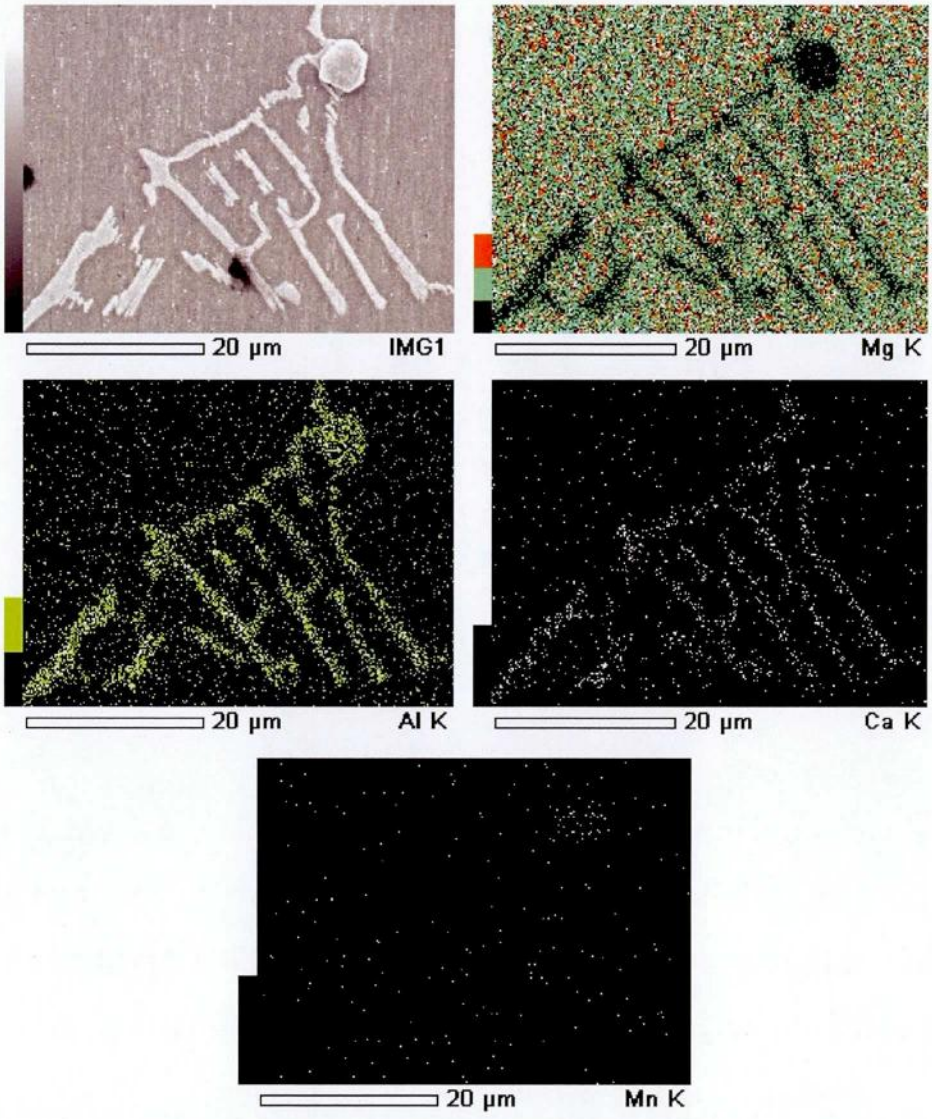

Fig. 3.5 EDS of cast AMX602 alloy showing intermetallic compounds.

3.2.2. Intermetallic compounds of cast ZAXE1711 alloy

Similar to that of AMX602 alloy, both ZAXE1711 and ZAXE1713 alloys have shown the intermetallic compound formation in their cast form. The XRD pattern of the cast ZAXE1711 alloy shows the peaks of both Al_2Ca and $Al_{11}La_3$ intermetallic compounds, as shown in Fig. 3.6. The ZAXE1713 alloy has shown the same types of intermetallic compounds that appeared in the ZAXE1711 alloy, as they both have the same alloying

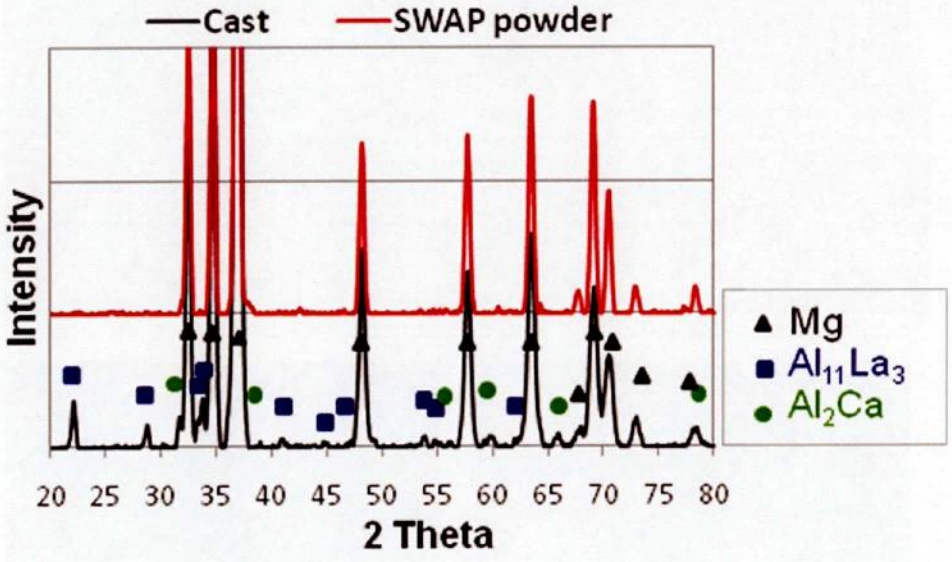

Fig. 3.6 XRD patterns of ZAXE1711 alloy SWAP powder and cast.

elements with similar percentages. The XRD pattern of the ZAXE1711 alloy SWAP powder indicated no intermetallic compounds in its structure. This also confirms the same finding about the AMX602 SWAP powder of having supersaturated alloying elements due to their high solidification rate.

The cast ZAXE1711 alloy contained relatively similar amounts of both of the aforementioned intermetallic compounds. Observing the form of both Al-La and Al-Ca compound particles in Figs. 3.7 (a) and (b), respectively, could also show that they are different from each other. In contrast to that of AMX602 alloy, Al-Ca compound particles tended to be separately distributed with irregular morphologies, while Al-La compound particles tended to have the parallel columnar form with considerably finer sizes. This fine size of $Al_{11}La_3$ intermetallic compound particles confirmed previous findings about the effect of rare earth elements in which they tend to refine the microstructure of Mg alloys [7].

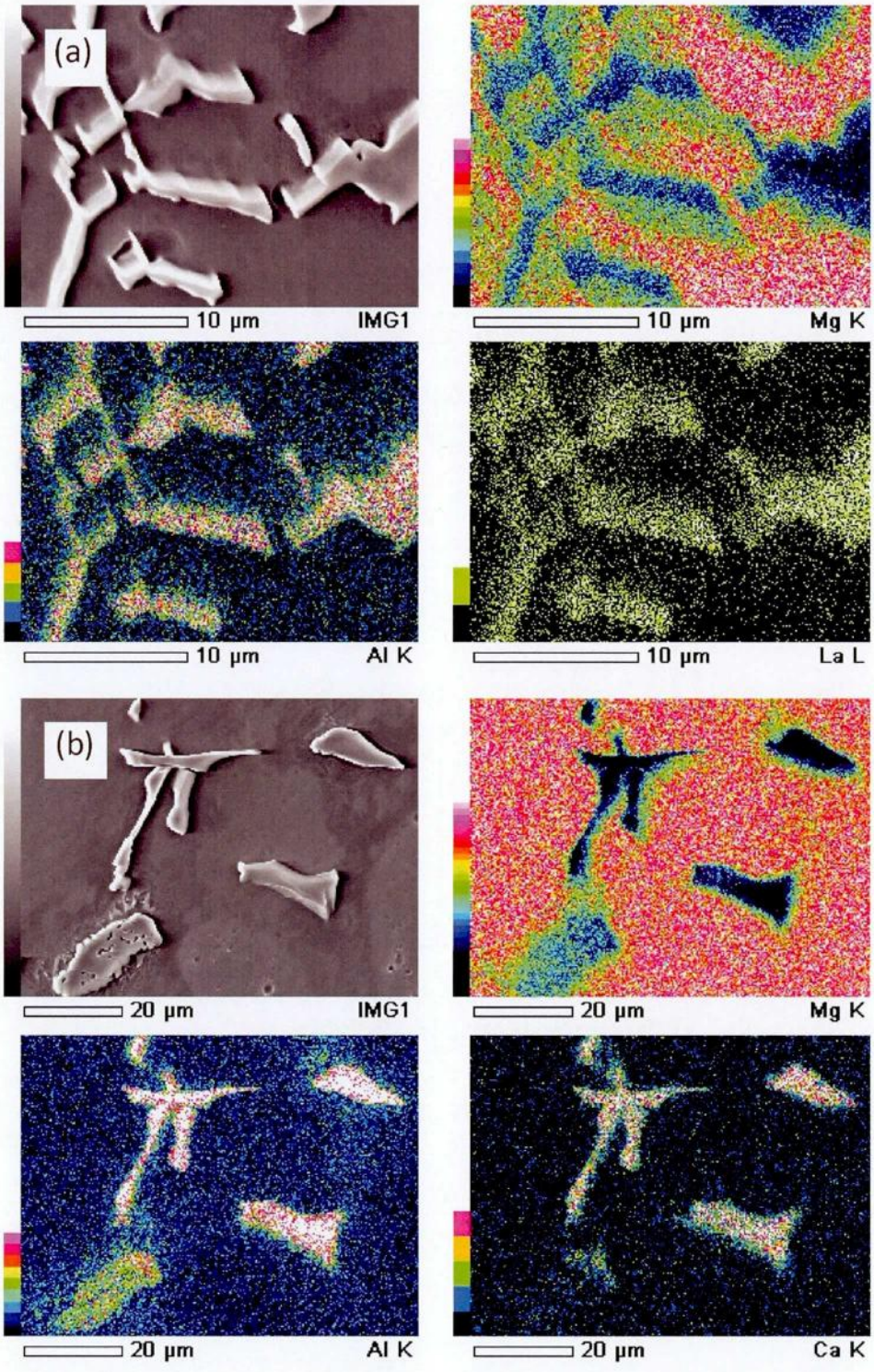

Fig. 3.7 EDS analysis of cast ZAXE1711 alloy showing both $Al_{11}La_3$ (a) and Al_2Ca (b) intermetallic compounds.

3.2.3. Intermetallic compounds of atomized ZK61 alloy powder

The atomized ZK61 alloy powder revealed the intermetallic compound of Mg_4Zn_7 dispersed along the α-Mg grain boundaries, as shown in both Figs 3.8 and 3.9. Peaks of this intermetallic compound can be seen along with those of Mg. This is different from those of both AMX602 and ZAXE1711 alloys' SWAP powders which showed no intermetallic compounds. This is due to the lower solidification rate obtained for gas atomization process compared with that of SWAP processing.

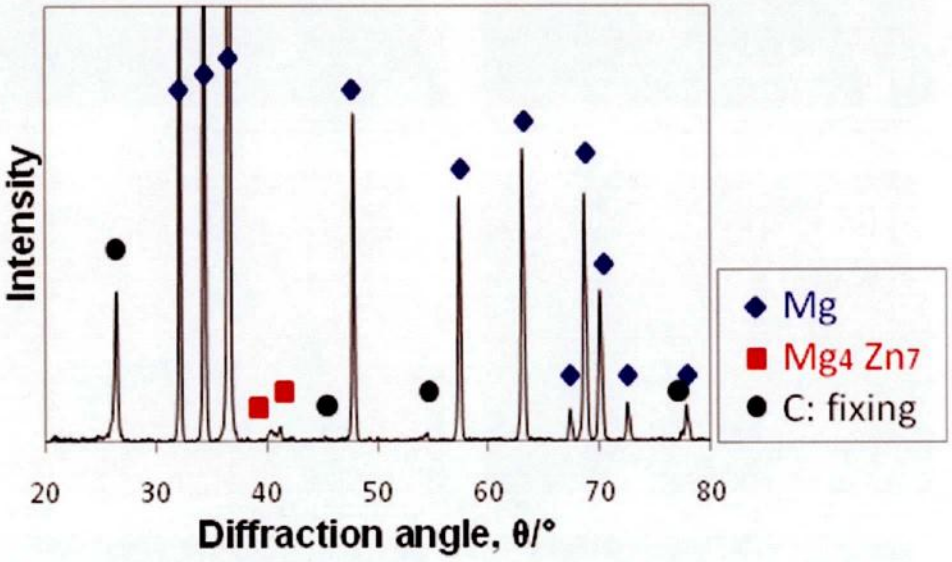

Fig. 3.8 XRD patterns of atomized ZK61 alloy powder.

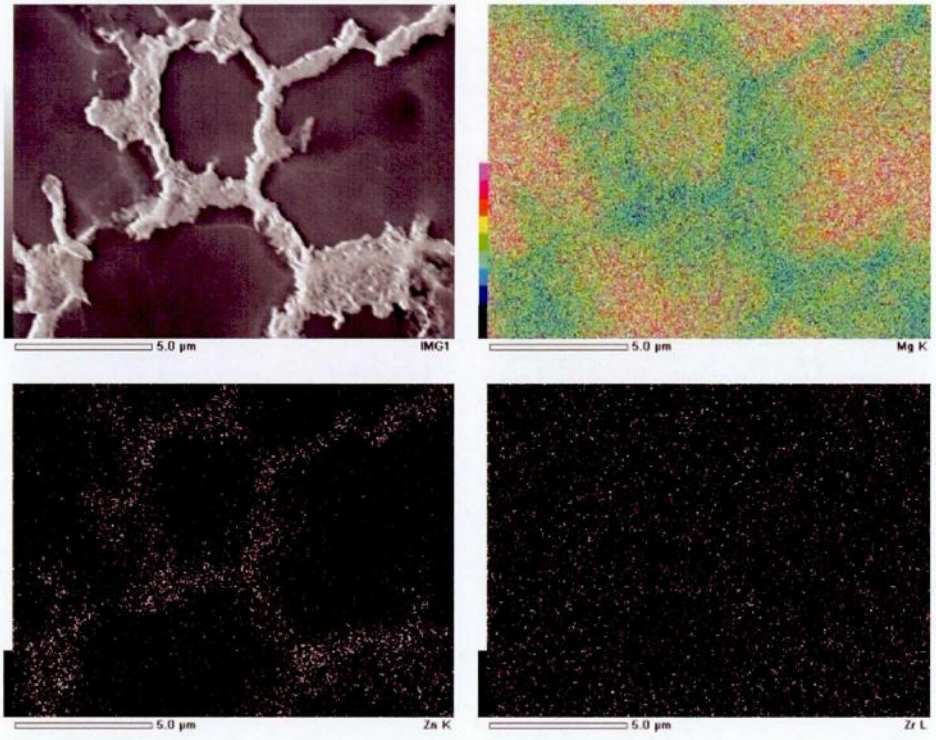

Fig. 3.9 EDS analysis of atomized ZK61 alloy powder showing Mg_4Zn_7 intermetallic compounds.

3.3. Effect of processing conditions on the microstructure of the powders

In order to investigate the effects of processing conditions (i.e. the extrusion and consolidation temperatures) on the microstructure of the investigated alloys, differential thermal analysis (DTA), high temperature XRD and annealing of the powders were performed.

3.3.1. Effect of thermal processing on AMX602 alloy powder

Figure 3.10 shows the DTA profiles of fine and coarse SWAP powders as well as of cast AMX602 alloy. They all had very similar patterns.

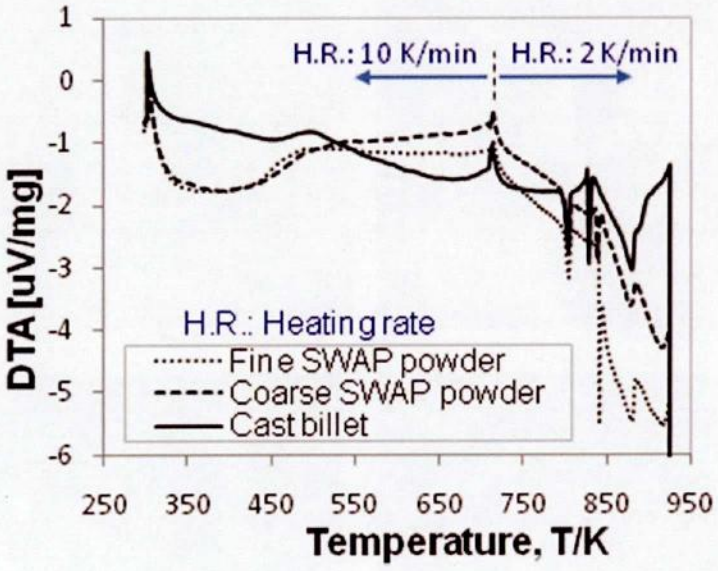

Fig. 3.10 DTA pattern of AMX602 alloy raw materials.

The first peak, observed at 723 K, is only due to the change in the heating rate from 10 to 2 K/min, to increase the resolution at the important range of high temperature. The second peak, observed at about 803 K, corresponds to an endothermic reaction due to the melting of Al_2Ca phase. Although that phase was not primarily present in SWAP powder, it precipitated due to heating of the sample powder during the DTA test. On the other hand, the third peak, observed at about 828 K for cast material and 838 K for SWAP powders, is due to the onset of melting of α-Mg phase. It could be confirmed by the DTA results that the thermal history of the hot extrusion process had a minor effect on recrystallization behavior compared to that of dynamic deformation as both the consolidation and hot extrusion temperatures were much lower than that of any metallurgical transformation observed in the DTA profile.

By observing the microstructures of AMX602 SWAP powder after annealing at 473K ~ 773K in argon gas atmosphere, it could be confirmed that the dendrite structure of SWAP powder showed no change until the

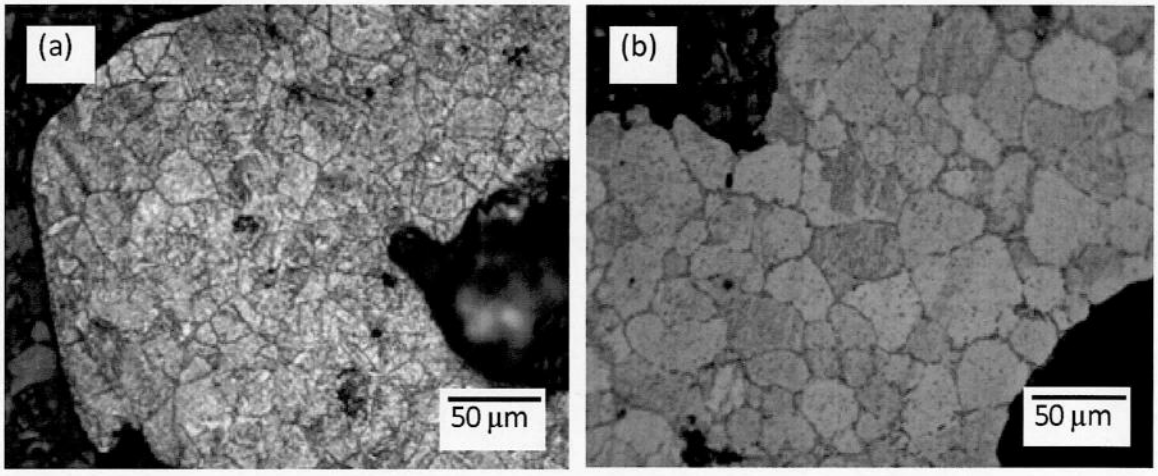

Fig. 3.11 microstructure of SWAP AMX602 alloy powder annealed at 623 K (a) and 773 K (b).

temperature of 573 K. Figure 3.11 (a) shows the microstructure of SWAP powder annealed at 623 K, which indicates that the change of microstructure and grain growth has been started between 573 and 623 K. This means that the SWAP powder can keep its fine dendrite structure and no change in microstructure occurs until 573 K without any grain growth. It is also shown that the structure was completely transformed to equi-axed grains, similar to that of the cast AMX602 alloy, with the size of 39 microns and the hardness of 65 Hv after annealing at 773 K, as shown in Fig. 4 (b). However, the processing of the alloy did not occur at this range of temperatures.

Figure 3.12 shows the XRD patterns of compacted powders after annealing at 773, 823, and 853 K compared to the as-received one. These temperatures were chosen to be just before and after the metallurgical transformation temperatures obtained from DTA profile, as shown in Fig. 3.10, to investigate the effect of these transformations on the final formation of compounds after extrusion. Two different phases were precipitated after annealing, namely Al_2Ca, which could also be observed in the cast material, and Al_6Mn. The latter has also been detected in the cast alloy but with a much lower percentage.

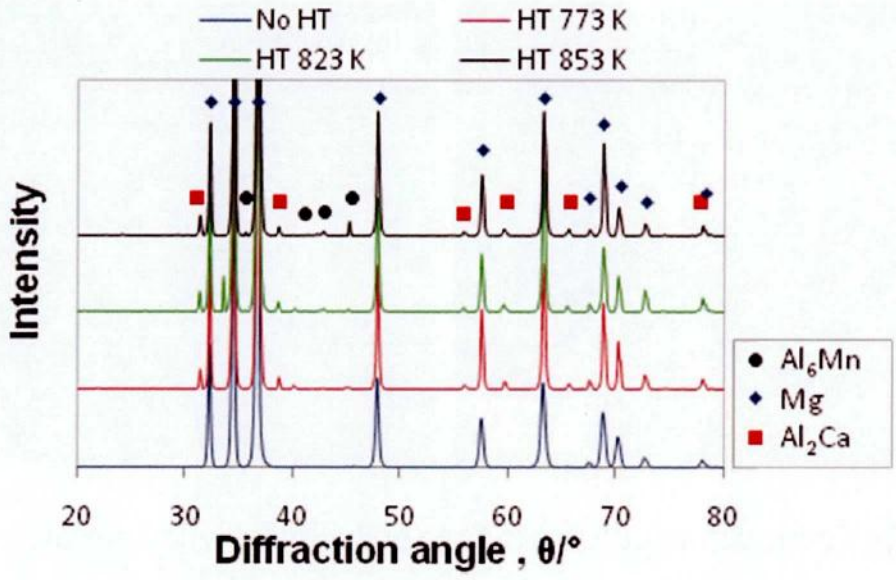

Fig. 3.12 XRD of SWAP AMX602 alloy powder annealed at various temperatures.

3.3.2. Effect of thermal processing on ZAXE1711 alloy powder

The DTA profiles of SWAP powder as well as of cast ZAXE1711 and ZAXE1713 alloys, as shown in Fig. 3.13, indicated an endothermic reaction due to the melting of Al_2Ca phase at about 800 K. Another endothermic reaction was shown at about 850 K due to the melting of $Al_{11}La_3$ phase. Those compounds were not originally present in SWAP raw powders. However, they were precipitated during heating the sample in the DTA test. This means that thermal processing of both SWAP powder and cast material at temperatures below 800 K has no effect on compound melting. The last peak observed in the figure is due to melting of α-Mg phase.

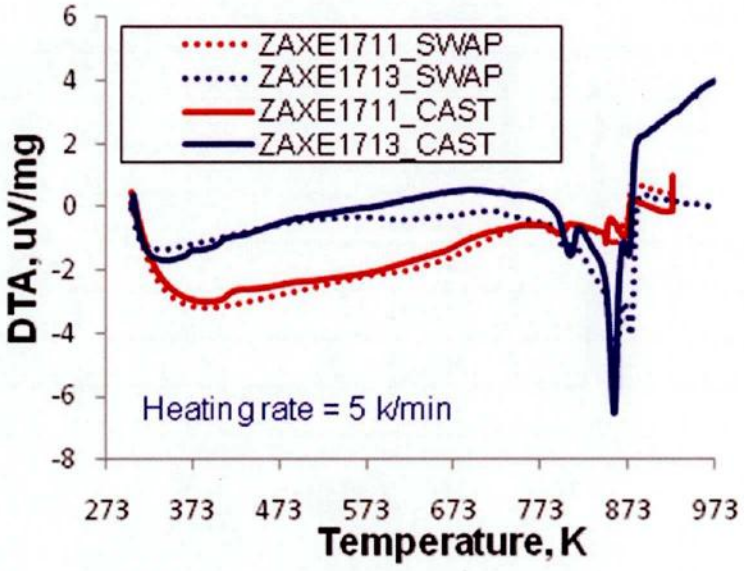

Fig. 3.13 DTA pattern of ZAXE1711 alloy raw materials.

For further understanding, both high temperature XRD and annealing of SWAP powder were performed. Figure 3.14 shows the XRD patterns of ZAXE1711 alloy SWAP powder at temperatures in the range of 573 to 823 K. The results indicate that Al-La compound particles started to precipitate between 573 and 623 K, and continued to exist until 823 K. Similarly, Al-Ca compound particles started to precipitate in the same range of temperatures, but started to melt after 773 K. Figure 3.15 indicates the effect of annealing at different temperatures on the microstructure changes of SWAP powders. The dendrite structure has been maintained after annealing at 573 K, while new boundaries of coarsened grains started to appear, as shown in Fig. 3.15 (a). Increasing the annealing temperature diminished the dendrite form of grains and changed the microstructure into conventional equi-axed grains, as shown in Fig. 3.15 (b). Compound particles changed to the fine dispersed form for annealing at 723 K, with the size of particles relatively higher near the grain boundaries. Annealing at 823 K resulted in the coarsening of both grains and the compound particles to sizes comparable to that of the cast

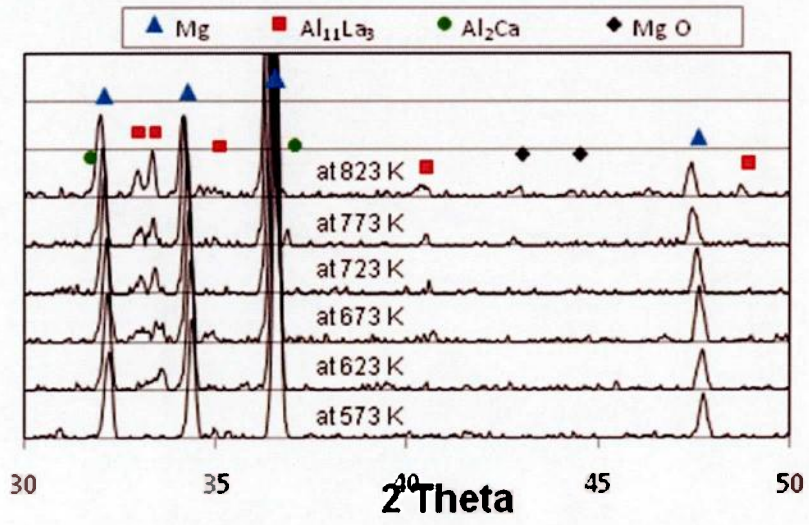

Fig. 3.14 XRD of SWAP ZAXE1711 alloy powder at various temperatures.

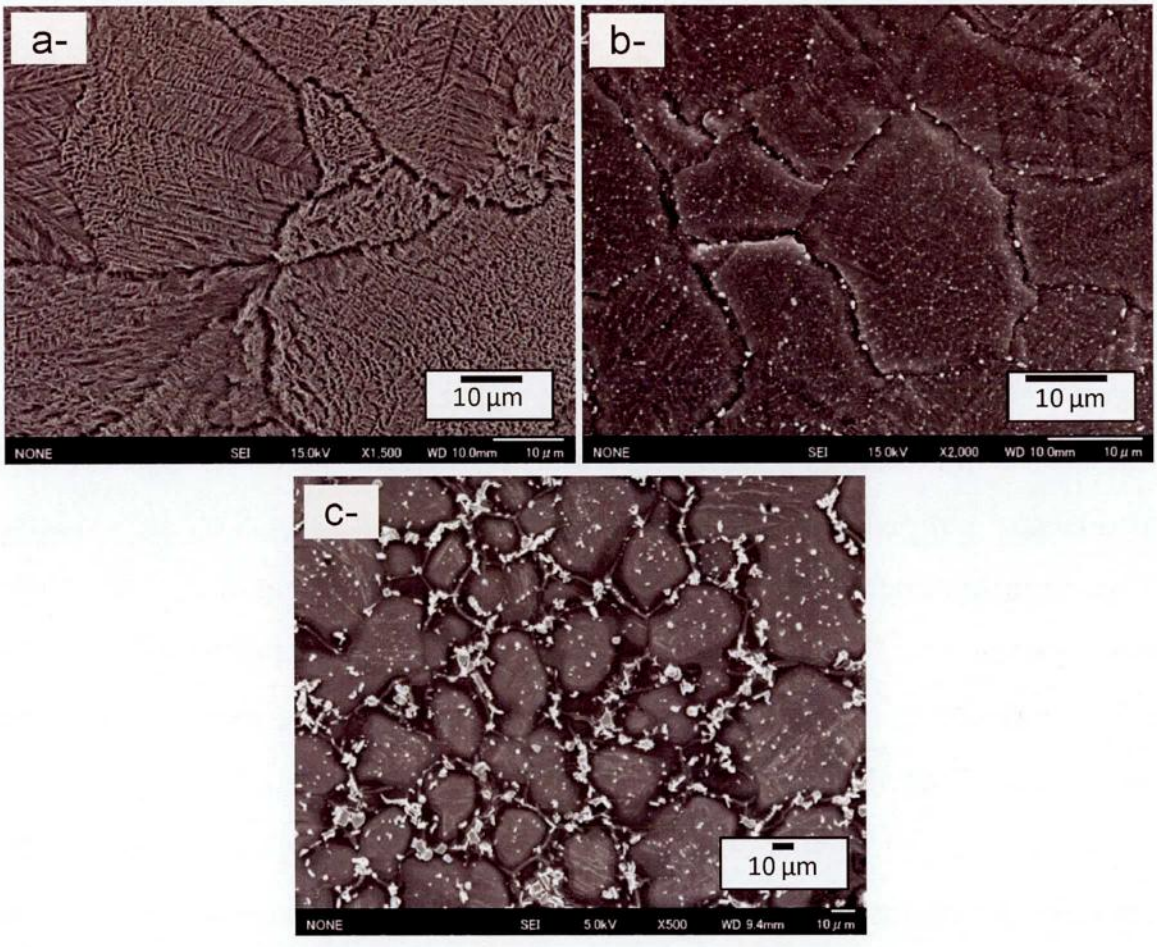

Fig. 3.15 Microstructure of ZAXE1711 alloy SWAP powder annealed at 573 K (a), 723 K (b) and 823 K (c).

ingot of the alloy, shown in Fig. 3.2 (b). However, the processing conditions used in this study did not include temperatures higher than 673 K, which means that the SWAP powder did not undergo such kind of grain coarsening.

3.3.3. Effect of thermal processing on ZK61alloy powder

The atomized ZK61 alloy powder has shown the intermetallic compound of Mg_4Zn_7 in its as-received condition. Thermal processing of this alloy powder has resulted in no sign of further precipitation of other intermetallic compounds. However, its effect on the grain size of the powder can be observed in Fig. 3.16. The grain size has increased from 3.2 μm, for the as-received powder, to 7.9 and 9.8 μm after annealing at 573 and 673 K, respectively. This has decreased the hardness of the powder from 79.4 to 76.6 and 74.2 Hv after annealing. The above mentioned finding can also be confirmed through the XRD pattern of the annealed powder at the same temperatures shown in Fig. 3.17. The pattern of the as-received powder did not change after annealing with no other peaks observed.

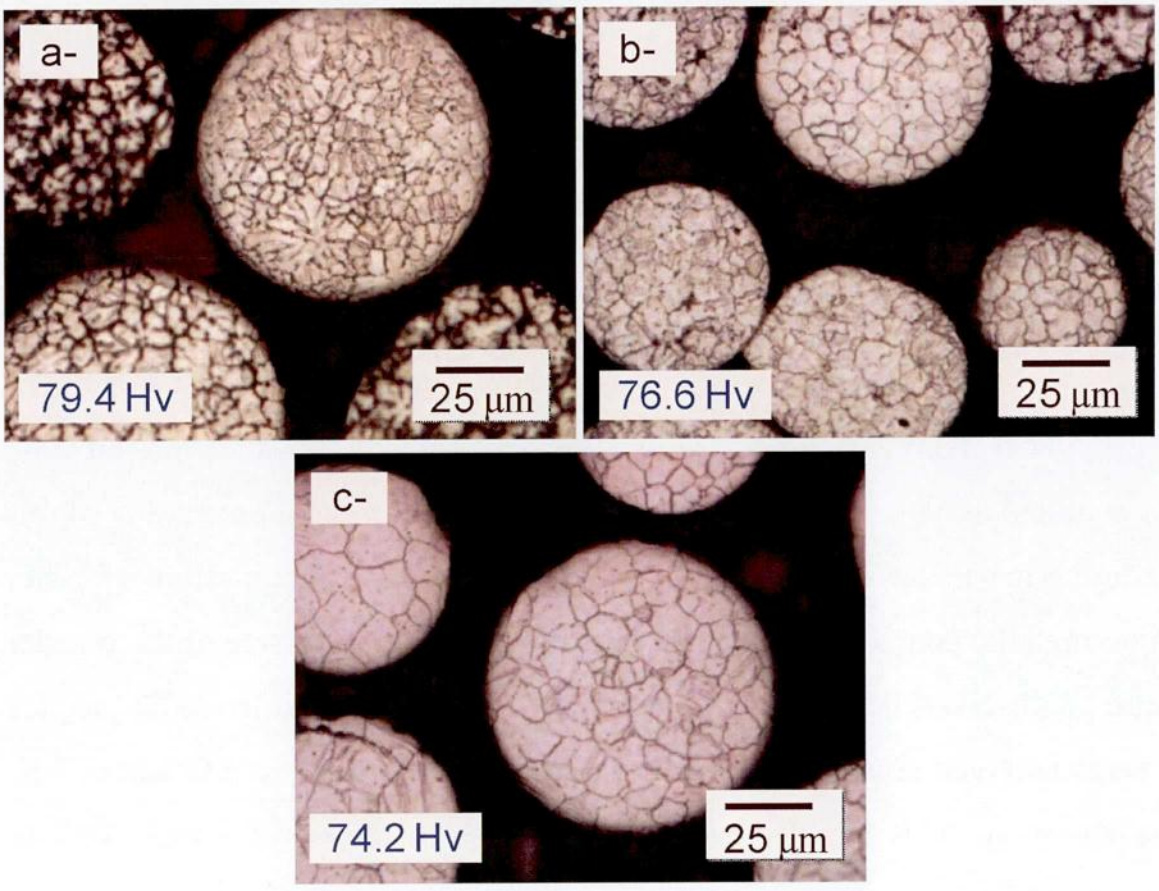

Fig. 3.16 microstructure of ZK61 alloy in its as-received condition (a), annealed at 573 K (b) and 673 K (c).

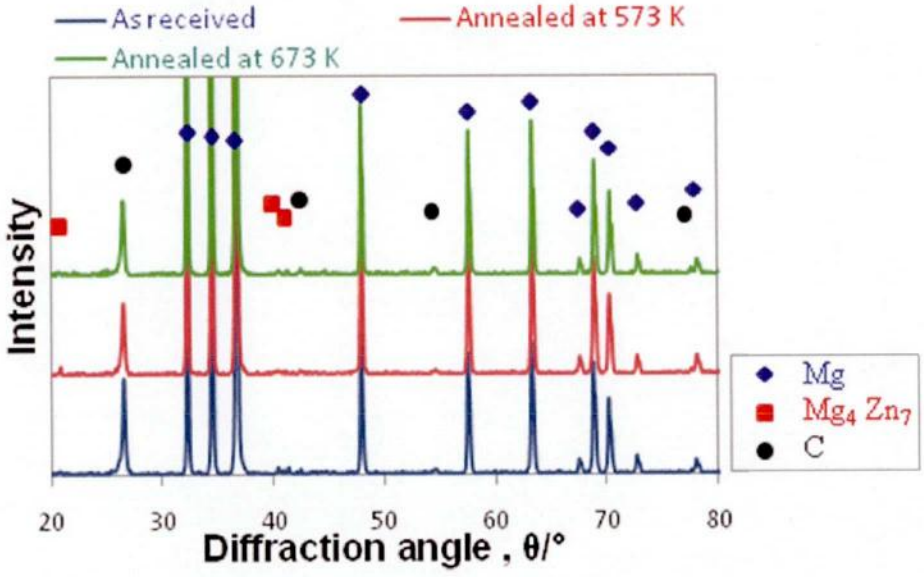

Fig. 3.17 XRD of ZK61 alloy powder annealed at various temperatures.

Conclusion

The microstructure and the intermetallic compounds, as well as the effect of thermal processing on them, have been investigated for magnesium alloys' powders and cast billets. Extensive investigations about the existence of compound particles, as well as their morphology, have been carried out. Furthermore, the effects of thermal processing on the structure of the powders have also been studied. The following conclusions were obtained:

(1) The SWAP and gas atomization processes used for the fabrication of the Mg-powders have resulted in a high solidification rate causing very fine microstructures.

(2) Supersaturation of the alloying elements was another advantage of the SWAP process, as it resisted the formation of unfavorable coarse compounds. On the other hand, some compounds were formed at grain boundaries of atomized ZK61 powder as a result of the lower solidification rate.

(3) The microstructure of the Mg-powders could be found stable under the thermal processing conditions used in this study. That was evident through keeping their dendrite structure and not forming intermetallic compounds.

References

[1]A. Elsayed, J. Umeda, K. Kondoh, Acta Materialia, 59 (2011) 273-282.

[2] A. Elsayed, K. Kondoh, H. Imai, J. Umeda, Materials & Design, 31 (2010) 2444-2453.

[3] K. Kondoh, A.H. Elsayed, H. Imai, J. Umeda, T. Jones, Materials & Design, 31-3 (2010) 1540-1546.

[4]F. Henmann, F. Sommer, B. Prodel, Materials Science and Engineering A, 125 (1990) 249-265

[5] J. Cai, G.C. Ma, Z. Liu, H.F. Zhang, A.M. Wang, Z.Q. Hu, Materials Science and Engineering A 456 (2007) 364-368.

[6] S. Nishida, M.J. Motomura, Journal of the Japan Institute of Light Metals, 38 (2008) 439-444.

[7] I.A. Anyanwu, Y. Gokan, A. Suzuki, S. Kamado, Y. Kojima, S. Takeda, Materials Science and Engineering A, 380 (2004) 93-99.

Chapter 4 Microstructure and texture of extruded Mg alloys fabricated by rapid solidification powder metallurgy

This chapter introduces the microstructure and texture evolution after hot extrusion of Mg alloys powders. The grain sizes and the morphologies of intermetallic compounds are discussed in details.

4.1. Introduction

The thermo-mechanical processing, especially hot extrusion has extensively been used to produce wrought magnesium alloys for various applications [1]. The effects of processing conditions on the microstructure and mechanical properties of extruded magnesium alloys are discussed. These conditions were reported to considerably control the characteristics of the extruded magnesium alloys, as it is well known that α-Mg grains are refined for extrusion at lower temperatures due to dynamic recrystallization [2]. The texture formation, as well as the dynamic recrystallization behavior, during extrusion were also discussed, which were previously reported to affect their mechanical properties and anisotropy [3, 4]. As for the consolidation of powders to prepare the extrusion billets, it was performed using two routes, namely cold compaction and spark plasma process (SPS). SPS results in the improved bonding between powder particles along with the uniform sintering and reduced internal stresses due to evenly dispersed spark plasma energy between powder particles. Another very important benefit of SPS is the minimized grain growth, compared to that of the conventional sintering process, due to localized heating during consolidation

[5]. However, only the microstructures of the extruded alloy powders are discussed below.

4.2. Microstructure and intermetallic compounds of extruded alloys

4.2.1. Microstructure of extruded AMX602 alloy

The extrusions of the AMX602 alloy powder compacts as well as the cast billets, for comparison, have been performed at 573, 623 and 673 K. Figure 4.1 shows the SEM images of extruded AMX602 alloy observed at a plane normal to the extrusion direction. As examples, cold compacted SWAP powder, billets sintered using SPS at 473 K, and cast billets extruded at 573 and 673 K only are shown. The grain sizes, which were calculated by using the image analysis software and shown by ovals in the figure, have been revealed to decrease as the extrusion temperature decreased, which is consistent with previous findings [2]. Generally, the extruded SWAP powders resulted in very fine and homogeneous grain sizes in the order of 0.4 to 0.5 μm, while extruded cast billets resulted in coarser and less homogeneous grain sizes in the order of 2 to 3.3 μm, which is still much finer than those of other cast alloys reported in a previous study [6]. That non-homogenity in the grain sizes of the extruded cast AMX602 alloy is due to the incomplete dynamic recrystallization, which resulted in the presence of some deformed only grains. The dynamic recrystallization behaviors are discussed in details later in this chapter. Further discussion on the dynamic recrystallization can be found later in this chapter. It can also be seen from the figure that consolidation using SPS did not result in considerable difference than that of cold compaction in terms of microstructure, as a result

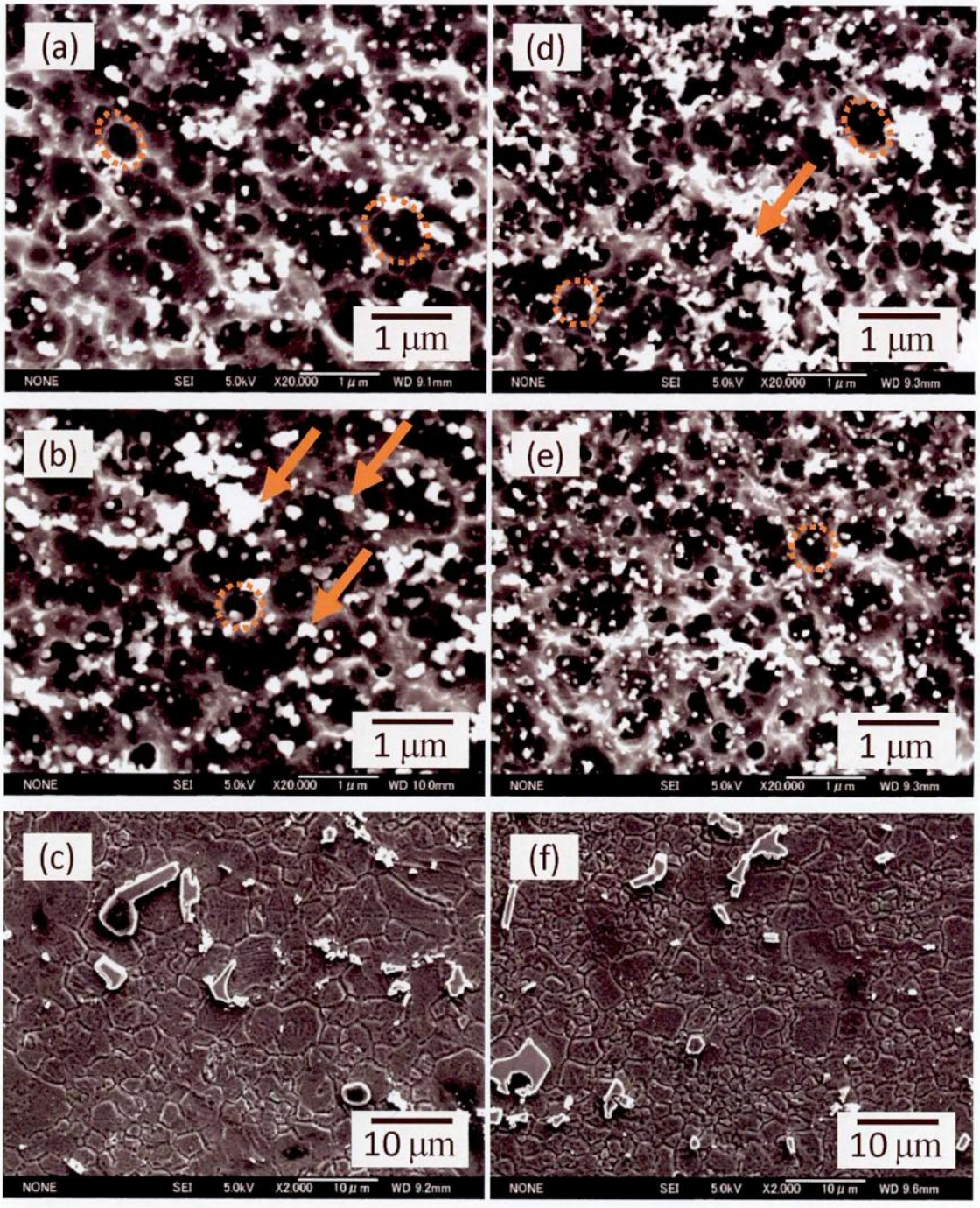

Fig. 4.1 Microstructures of the AMX602 alloy SWAP powder cold compacted (a), SPS at 473 K (b) and cast (c) extruded at 673 K, and SWAP powder cold compacted (d), SPS at 473 K (e) and cast (f) extruded at 573 K.

of the dominance of the dynamic recrystallization effect during hot extrusion. Very slight coarsening in both grains and intermetallic compound particles

can be observed for specimens consolidated using SPS than those cold compacted.

Observation of the microstructure of extruded SWAP powder materials indicates that Al_2Ca compounds, shown by arrows in Fig. 4.1, are evenly dispersed in the structure with fine grains, which in turn is expected effectively to strengthen the material as the evenly dispersed fine compound particles are well known to improve the strength of Mg alloys, especially through the effect of suppression of grain boundary sliding [7, 8]. Figure 4.2 shows EDS analysis results of the cast extruded AMX602, where the precipitation of Al_2Ca compound, confirmed also by XRD analysis, can be observed. The morphologies of the intermetallic compound particles of the extruded cast AMX602 alloy has more irregular shapes, coarser sizes with 5 ~ 10 μm length and less distribution than those of the extruded SWAP powders, which are not favored in terms of strength.

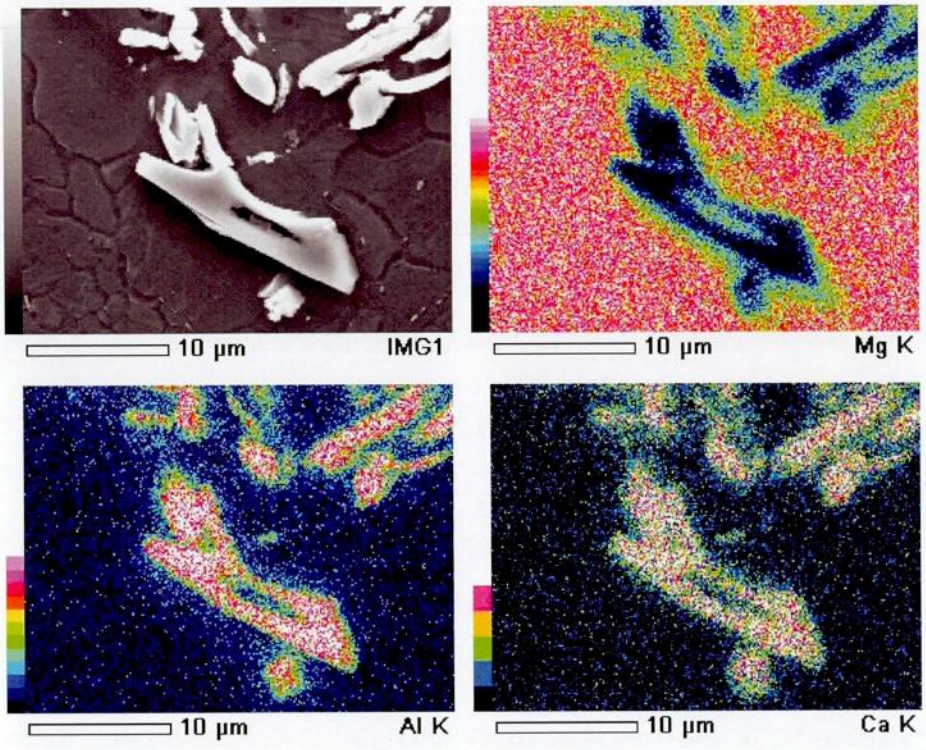

Fig. 4.2 EDS of AMX602 cast alloy extruded at 673 K.

For comparison of precipitation, the SEM images of the microstructure of AMX602 alloy SWAP powders, consolidated and extruded at higher temperatures, 793 and 823 K, are shown in Fig. 4.3 (a) and (b), respectively. The microstructures of these specimens show much coarser microstructures than those extruded at 573 and 673 K. The sizes of intermetallic compound particles were also drastically increased to 1 ~ 3 μm, especially for the specimen extruded at 823 k. That drastic increase in the size of intermetallic compounds suggests the occurrence of local melting, as this temperature is close to that of the onset of melting of α-Mg detected by DTA in Fig. 3.10. It could also be confirmed that these coarse intermetallic compounds are Al_2Ca and no other intermetallic compounds existed, as shown in Fig. 4.4.

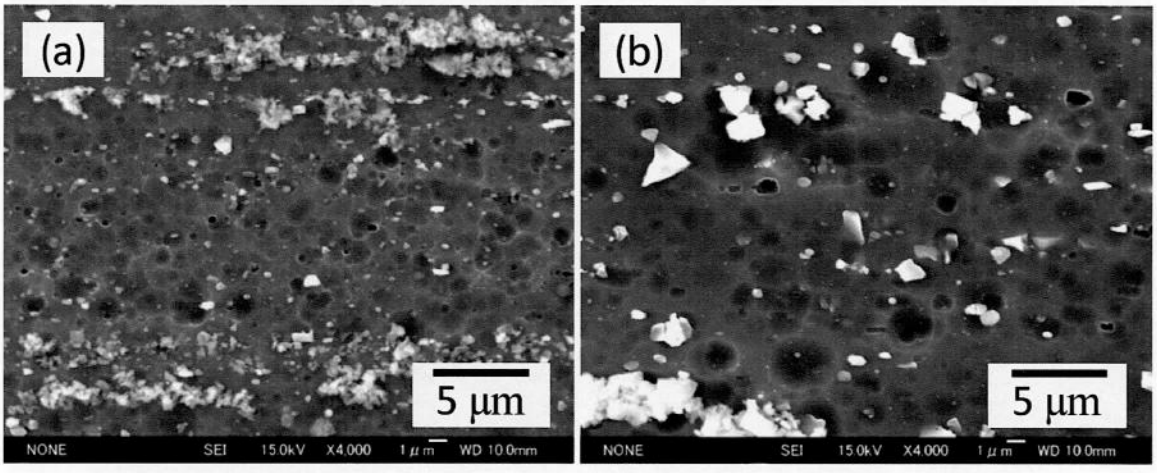

Fig. 4.3 Microstructures of cold compacted SWAP AMX602 alloy powder extruded at 793 K (a) and 823 K (b).

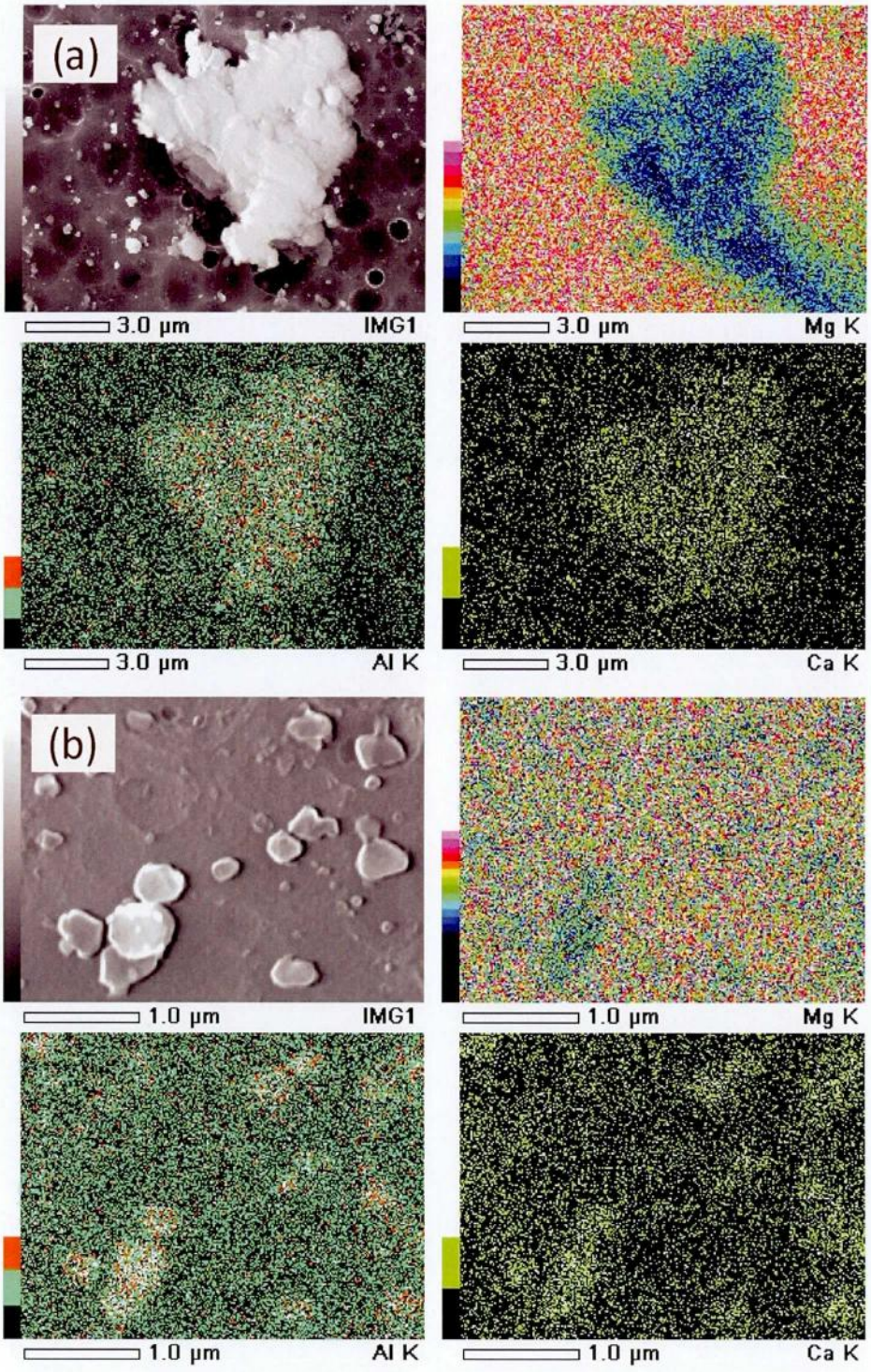

Fig. 4.4 EDS of coarse (a) and fine (b) intermetallic compound particles in cold compacted SWAP AMX602 alloy powder extruded at 793 K.

4.2.2. Microstructure of extruded ZAXE1711and ZAXE1713 alloys

Figure 4.5 shows the observed SEM images of extruded ZAXE1713 and ZAXE1711 alloys. As examples, SWAP powders of both alloys consolidated via cold compaction and extruded at 573 and 673 K, as well as cast ZAXE1711 alloy extruded at 673 K, are shown. They were selected to represent the lowest and highest extrusion temperatures. The extruded SWAP powder specimens indicate that the structure consists of fine intermetallic compound particles dispersed in the matrix of fine α-Mg grains, while in the case of extruded cast specimens both the grains and the compound particles had coarser sizes. Those compounds, confirmed to be both Al_2Ca and $Al_{11}La_3$ using XRD analysis, have been formed during dynamic recrystallization associated with the hot extrusion process. The amount and size of these precipitated compounds obviously depended on the La content. By increasing the content of La addition from 1.5 % for ZAXE1711 alloy to 3.3 for ZAXE1713 alloy, the coarser precipitated compounds could be observed. The effect of La on the microstructure of Mg alloys has been previously shown to be through the formation of fine compound particles [9, 10]. Those fine compound particles promote the nucleation of fine grains during dynamic recrystallization when performing hot extrusion, which ultimately improve the properties of the alloy. However, when the La addition increases over a certain limit, it starts to form coarser intermetallic compound because of its low solubility in magnesium [10]. That confirms the negative effect of 3.3% La addition on magnesium alloys.

The use of SPS has resulted in the formation of more and coarser precipitated compounds than that of cold compacted samples, as shown in Fig. 4.5 (e). This is because of the relatively high temperature and long processing time used for SPS process, 623 K, and 1.8 ks, respectively.

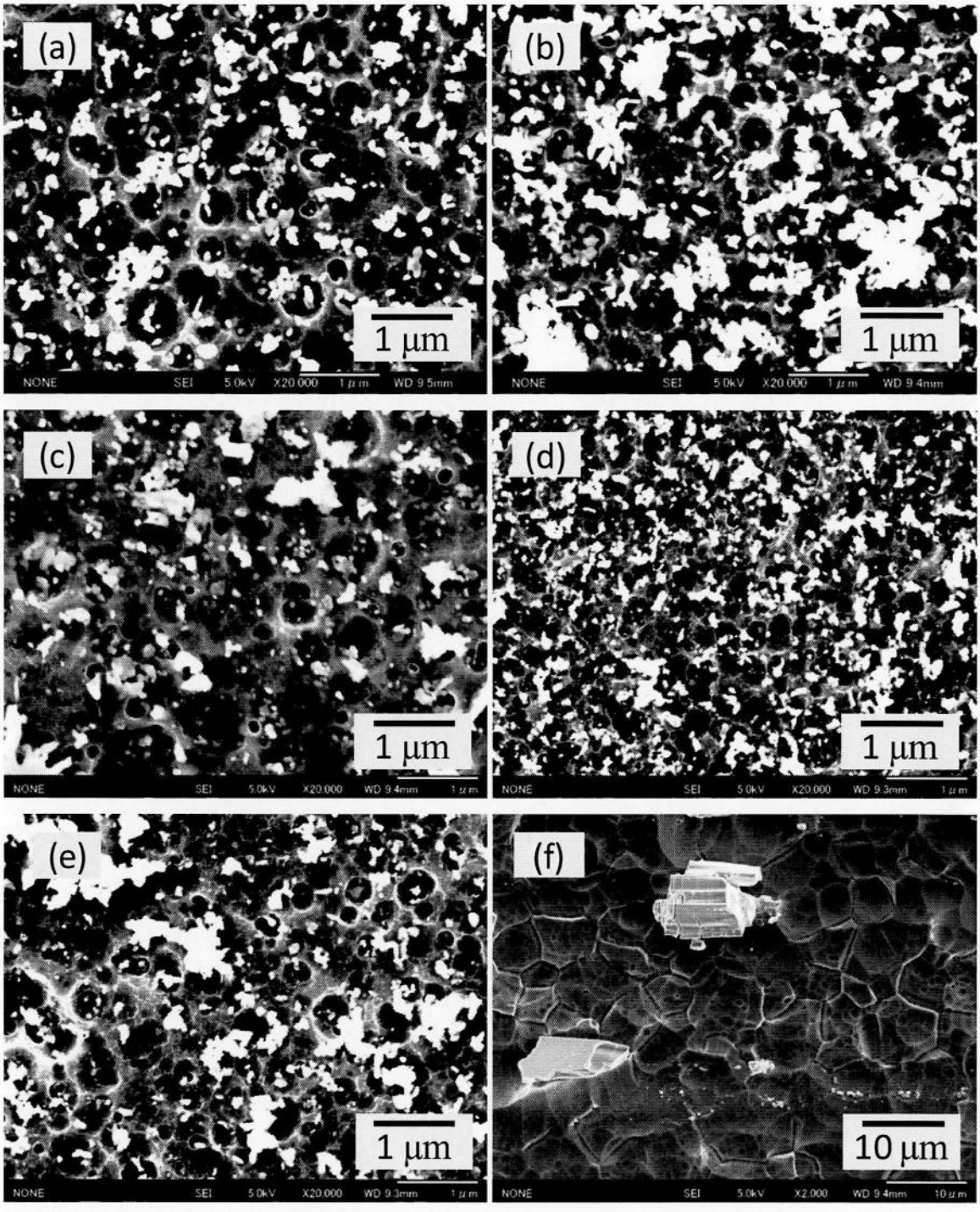

Fig. 4.5 Microstructures of cold compacted SWAP powder of ZAXE1713 alloy extruded at 673 K (a) and 573 K (b), ZAXE1711 alloy extruded at 673 K (c) and 573 K (d), SPS at 623 K and extruded at 673 K (e), and cast extruded at 573 K (f).

Similar to that of extruded AMX602 alloy, the grain size, which was calculated by the image analysis software, was shown to decrease as the extrusion temperature decreased. The same behavior was also observed for the case of the size of the precipitated compounds. Figure 4.6 shows the morphology of the coarse intermetallic compound of cast ZAXE1711 alloy extruded at 573 K. Both Al_2Ca and $Al_{11}La_3$ compounds exist in the structure, but with Al_2Ca having much coarser morphologies, which conforms to the aforementioned finding about La to form finer compounds. The other consolidation and extrusion conditions have also resulted in the formation of the same intermetallic compounds, as shown in the XRD pattern of Fig. 4.7. The peaks of both compounds could be detected in all conditions shown in the figure.

Generally, the extrusion of SWAP powders resulted in very fine and uniform grain sizes in the order of 0.4 to 0.5 microns, while extruded cast billets showed coarser grains in the order of 5 μm, as shown in Fig. 4.5 (f). Unlike to that of extruded AMX602 alloy, the extruded ZAXE1711 cast alloy has shown a homogeneous distribution of the grain sizes, a sign of the complete dynamic recrystallization, which will be discussed later in this chapter.

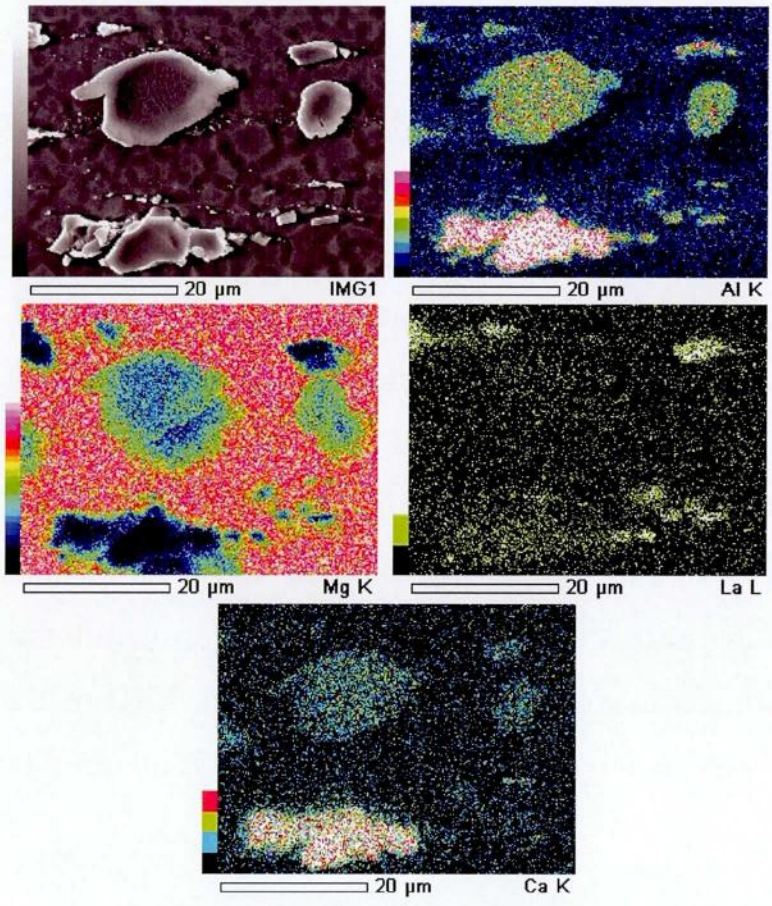

Fig. 4.6 EDS of cast ZAXE1711 alloy extruded at 573 K.

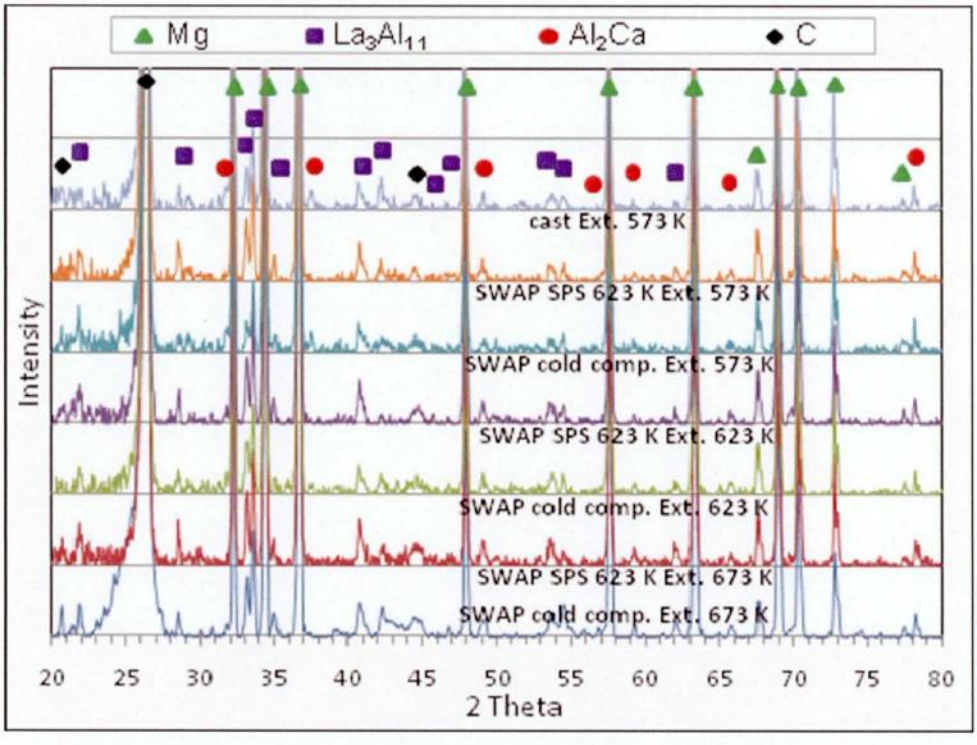

Fig. 4.7 XRD pattern of ZAXE1711 alloy extruded at various conditions

4.2.3. Microstructure of extruded ZK61 alloy

Figure 4.8 shows the optical microstructures of extruded ZK61 alloy. Although the consolidation and extrusion have been performed at 9 different conditions, only 4 examples of these conditions were selected to show the effect of the preparation conditions on the microstructure of the extruded alloy. The grain size, which was calculated by the image analysis software, was shown to decrease as the extrusion temperature decreased. Generally, the extruded atomized powders resulted in very fine and uniform grain sizes in the order of 1 to 2 microns, while extruded cast billets of previously reported research on matching alloy resulted in coarser grains in the order of 10 microns [11]. The microstructures, shown in Figure 4.8, along with the results of XRD, not shown herein, confirm that extruded atomized powder materials indicate that Mg_4Zn_7 compounds are finely dispersed in the structure with no remarkable difference between specimens with various preparation routes. This can also be shown in the SEM image of the specimen, both consolidated and extruded at 673, in which tiny inter-metallic compound particles can be seen at the grain boundaries, as shown in Figure 4.9. Although the very fine size of these particles did not enable them to be analyzed using EDS, XRD data was used to confirm the presence of these compound particles.

It can be also shown in Figure 4.8 that dynamic recrystallization has occurred homogenously during the extrusion process, which resulted in the monotonic microstructure with homogenous grain sizes. In contrast, previously reported microstructure of extruded cast ZK61 alloy was characterized with bimodal grain sizes as a result of the non-homogenous recrystallization behavior associated with coarse grained cast microstructures [11, 12]. The dominant effect of the extrusion temperature over that of the sintering temperature can be shown by comparing the pairs of Figure 4.8 (a)

to (b), (c) to (d), (a) to (c), and (b) to (d), in which it is clear that the extrusion temperature has the strongest effect on the grain size of the extruded ZK61 alloy.

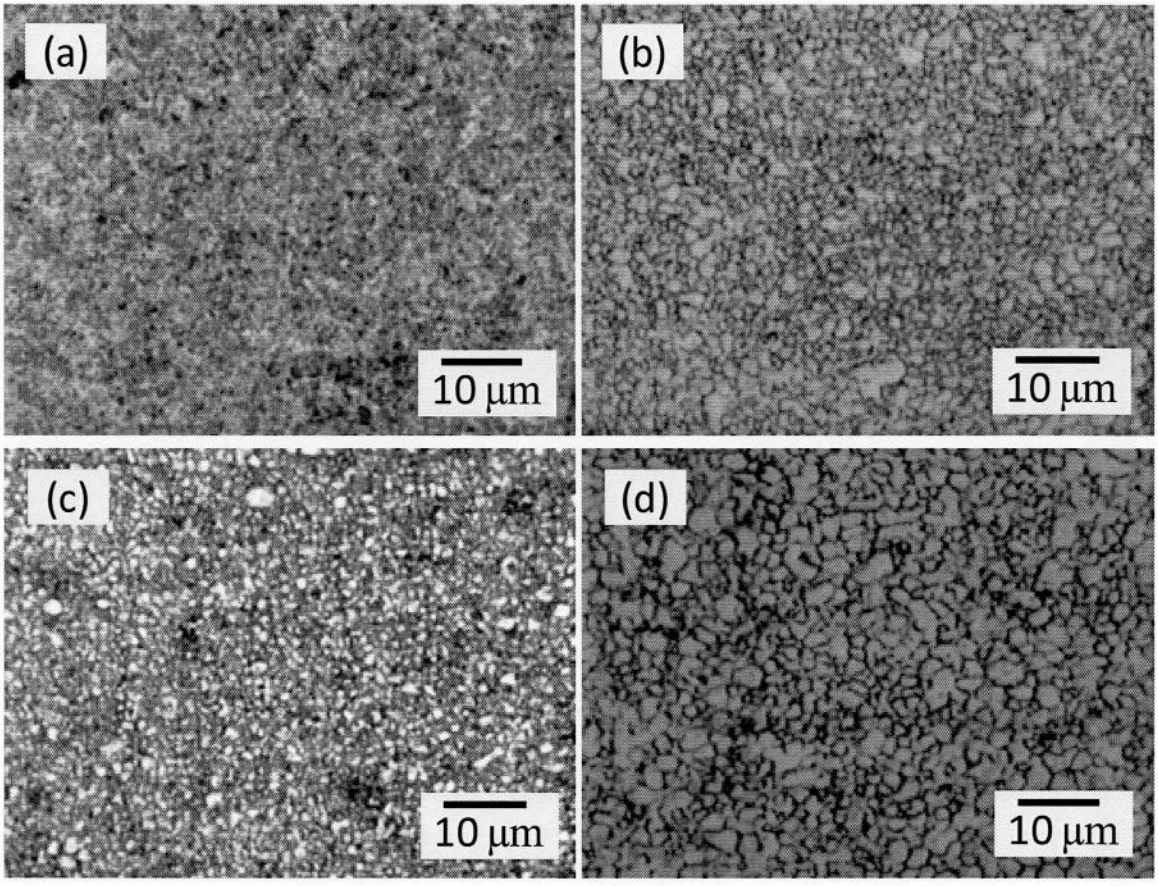

Fig. 4.8 Optical microstructures of ZK61 atomized powder sintered at 473 and extruded at 523K (a) and 673 K (b), and those sintered at 673 K and extruded at 523 K (c) and 673 K.

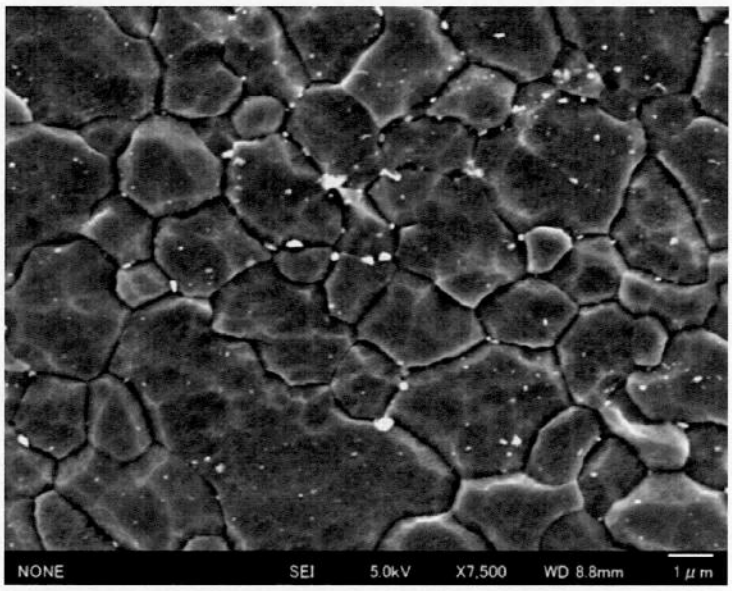

Fig. 4.9 SEM image of the microstructures of ZK61 atomized powder sintered at 673 K and extruded at 673 K

4.3. Texture evolution in extruded SWAP and cast magnesium alloys

In order to reveal the texture evolution during extrusion of the Mg alloys, the EBSD analysis has been applied to both extruded SWAP powder specimens and extruded cast ones, as shown in Fig. 4.10. Both the AMX602 and the ZAXE1711 alloys have been selected for this analysis. The inverse pole figures (IPF) showing the crystal orientation mapping, with the extrusion direction vertically aligned, and the corresponding pole figures (PF) of (0001) basal plane texture of the extruded specimens are shown in the figure. The inter-metallic compound particles are not shown in this map with the black dots representing their positions.

Fig. 4.10 The EBSD analysis results of (a) AMX602 alloy SWAP powder, (b) AMX602 alloy cast, (c) ZAXE1711 alloy SWAP powder, and (d) ZAXE1711 alloy cast specimens extruded at 673 K showing both the crystal orientation mapping and the basal plane orientation texture.

The (0001) basal plane texture shows a mixture of the normal and transverse components, which is consistent with the findings by other references [13]. The basal planes in most grains are aligned along the direction that makes an acute angle with the normal direction towards the

transverse side. The maximum intensity of the basal texture shows the values of 5.1 for extruded SWAP powder specimens, and 8.8 for extruded cast ones. It should also be noted that the grain sizes of extruded cast AMX602 alloy have shown non-homogenous distribution, an observation which is consistent with that of SEM images in Fig. 4.1 (c) and (f). This was due to the incomplete dynamic recrystallization, which resulted in both recrystallized and deformed grains, which conforms to previous findings [14, 15]. The extruded ZAXE1711 ally has shown lower values of maximum intensity of the basal plane texture than that of AMX602 alloy. This was also accompanied by higher values of the average Schmid factor of ZAXE1711 alloy than that of AMX602 alloy. These results of randomized crystal orientations show that extruded ZAXE1711 alloy is expected to reveal less anisotropy than extruded AMX602 alloy in both tensile and compression properties at various loading directions. This texture randomization could be attributed to the effect of rare earth addition on the texture, which has been previously reported [16-22].

Separating both deformed and recrystallized grains in separate IPF maps and their PFs provides deeper insight of the effect of recrystallization during hot extrusion of the investigated alloys, as shown in Fig. 4.11. Deformed grains (b) show higher maximum intensity of the basal plane than that of recrystallized ones as a result of their strong texture [15]. However, as the volume fraction of the deformed grains is remarkably less than that of recrystallized ones, the maximum intensity of the basal plane texture did not increase considerably. It should also be noted that both types of grains show similar orientation of the basal plane compared to each other, and to that of extruded SWAP powder specimen.

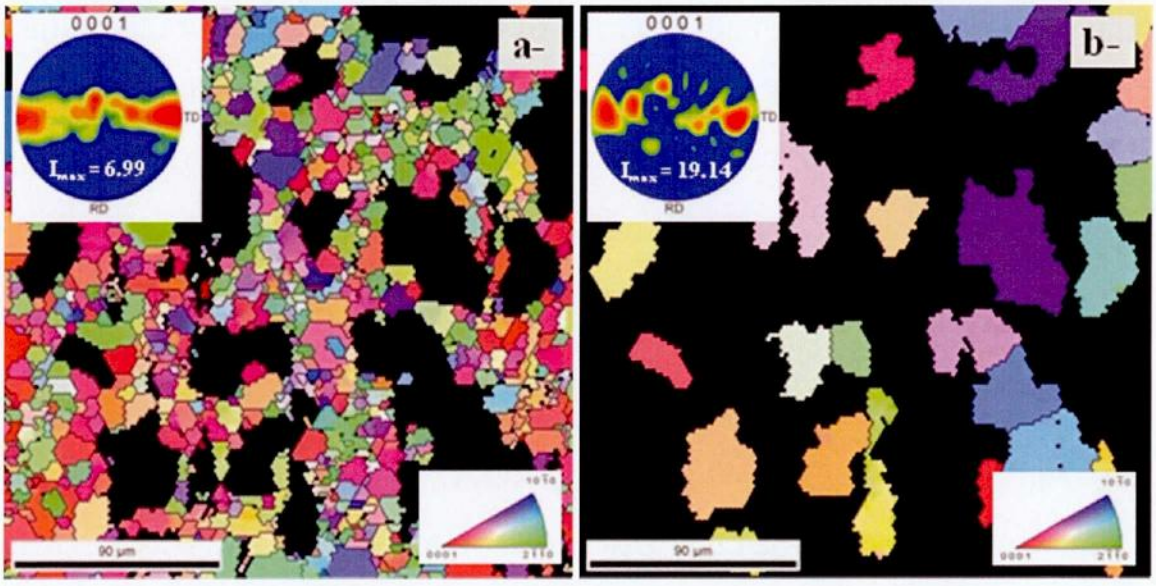

Fig. 4.11 The EBSD analysis results of AMX602 alloy cast specimen extruded at 673 K showing separately both the recrystallized grains (a) and the deformed grains (b).

For further investigation of the effect of extrusion conditions on the recrystallization behavior and on the evolution of texture, the EBSD patterns of AMX602 and ZAXE1711 alloys extruded at 573 K were also investigated. As shown in Fig. 4.12, they have shown similar results to those of specimens extruded at 673 K, including the texture pattern and the average Schmid factor. However, it is obvious that AMX602 alloy extrusions, even the extruded SWAP powder specimens, contained some amounts of deformed α-Mg grains. These grains have contributed to the increase of the maximum intensity of basal texture of AMX602 alloy, despite its common trend to decrease as a result of the lower extrusion temperature. The latter effect of extrusion temperature could be confirmed through the Zener-Hollomon parameter, according to the below equation [23]

$$Z = \dot{\varepsilon} \exp (Q / RT)$$

Fig. 4.12 The EBSD analysis results of (a) AMX602 alloy SWAP powder, (b) AMX602 alloy cast, (c) ZAXE1711 alloy SWAP powder, and (d) ZAXE1711 alloy cast specimens extruded at 573 K showing both the crystal orientation mapping and the basal plane orientation texture.

where Z is the Zener-Hollomon parameter, $\dot{\varepsilon}$ is the strain rate, Q is the activation energy which equals to 1.35 x 10^5 J/mol, R is the gas constant which equals to 8.314 J/K.mol, and T is the extrusion temperature. The

values of Z were 4.05 x 10^{11} and 0.06 x 10^{11} for specimens extruded at 573 and 673 K, respectively. It was previously clarified that higher Z values resulted in a reduced amount of recrystallized grains, weaker texture, and reduced anisotropy [23, 24], which meant that specimens extruded at 573 K were more likely to have weaker texture. However, this was overcome by the effect of the presence of strong-textured deformed grains. Separating both deformed and recrystallized grains of SWAP and cast AMX602 alloy extruded at 573 K reveals the considerably high values of maximum intensity of basal texture of deformed grains for both extruded SWAP powder and cast billets, as shown in Fig. 4.13. However, their volume fraction is much lower than recrystallized grains and also lower than that of cast AMX602 alloy extruded at 673 K shown in Fig. 4.11. It should also be noted that no such deformed grains could be observed in extruded ZAXE1711 alloy specimens at any of the extrusion temperatures. This could be due to the more distribution of intermetallic compound particles observed in extruded ZAXE1711 alloy which promoted the dynamic recrystallization in their vicinity.

It has been shown in previous reports that the Ca element has the effect of weakening of the texture of magnesium alloys through the random nucleation of recrystallized grains due to the formation of inter-metallic compound particles [25]. This effect can also be observed in this study in terms of the decreased maximum intensity of the basal texture of extruded SWAP powder specimen compared to that of extruded cast due to the fine distribution of intermetallic compounds, which never occurred in the case of the extruded cast alloys.

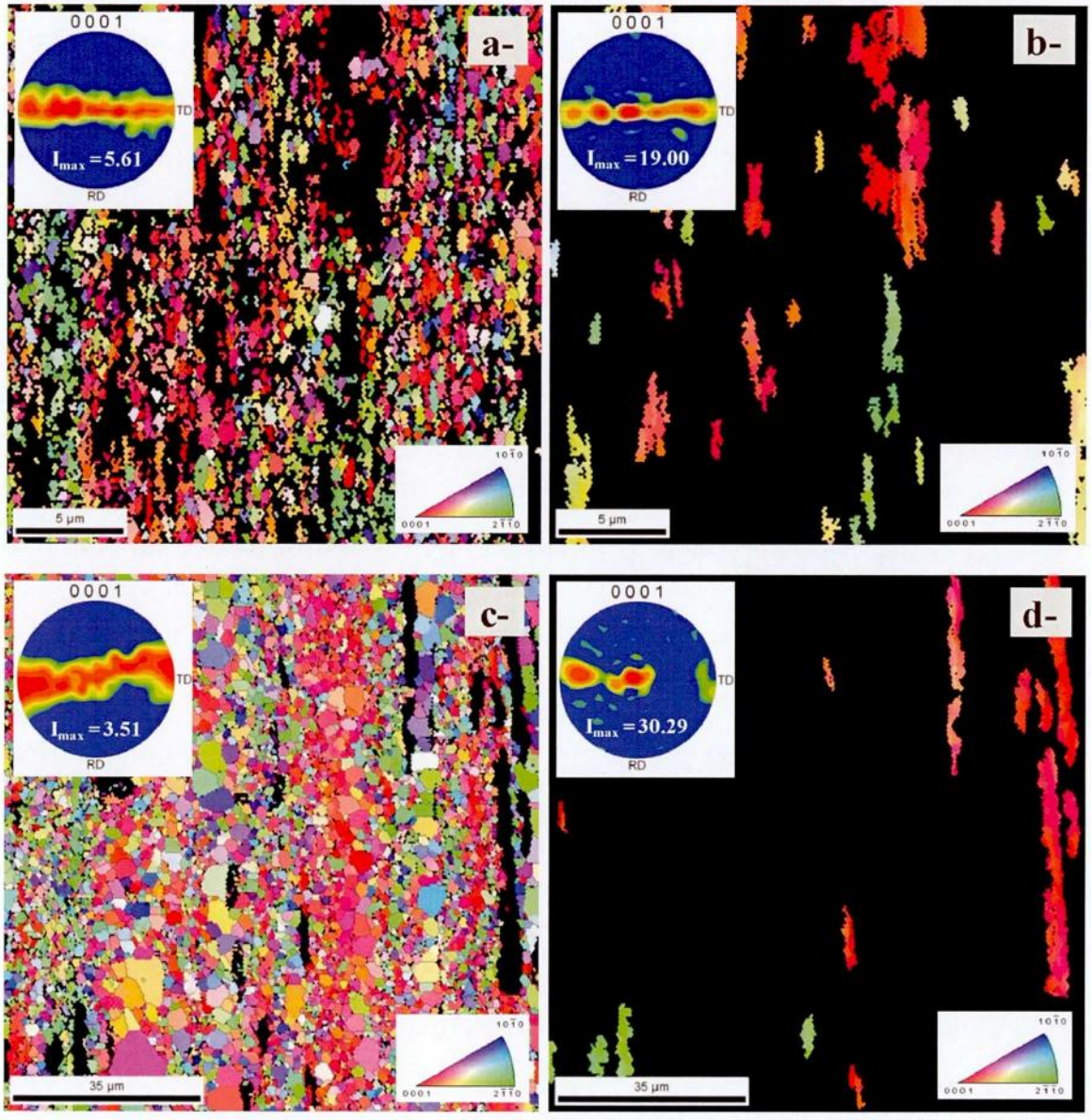

Fig. 4.13 The EBSD analysis results of AMX602 alloy SWAP powder extruded at 573 K showing separately both the recrystallized grains (a) and the deformed grains (b) and AMX602 alloy cast extruded at 573 K showing separately both the recrystallized grains (c) and the deformed grains (d).

4.4. Summary and Conclusions

The microstructure evolution during hot extrusion of the magnesium alloys, investigated herein, in terms of grain size and intermetallic compound particles morphology and distribution have been discussed in this chapter. The texture formation was also revealed by means of the back scattered diffraction pattern. The following conclusions can be obtained from the results introduced in this chapter:

(1) The powder metallurgy processing of magnesium alloys showed a very considerable improvement in the microstructure of the rapidly solidified SWAP powder compared to that of extruded cast alloys.

(2) The compound effects of both the powder metallurgy processing and the alloying with the elements combinations in this study contributed to the realization of a fine grain sizes and good dispersion of fine intermetallic compound particles which were favorable for higher strength.

(3) The magnesium alloys investigated herein showed a considerably randomized texture for extruded SWAP powders compared to that of extruded cast billets.

(4) Incomplete dynamic recrystallization occurred in the case of AMX602 alloy, especially in its extruded cast form, due to the high value of Zener-Hollomon parameter. However, a complete dynamic recrystallization occurred in the case of ZAXE1711 alloy for all preparation conditions due to the presence of the fine dispersed intermetallic compounds.

References

[1] S. Kamado, J. Koike, K. Kondoh, Y. Kawamura, Materials Science Forum, 419-422 (2003) 21-34.

[2] T. Murai, S. Matsuoka, S. Miyamoto, Y. Oki, Journal of Materials Processing Technology, 141 (2003) 207–212.

[3] L.L. Chang, Y.N. Wang, X. Zhao, M. Qi, Material Characterization, 60 (2009) 991-994.

[4] T. Al-Shamman, X. Li, S.G. Chowdhury, Materials Science and Engineering A, 527 (2010) 3450-3463.

[5] T.T. Sasaki, T. Ohkubo, K. Hono, Acta Materialia, 57 (2009) 3529-3538.

[6] H. Ding, L. Liu, S. Kamado, W. Ding, Y. Kojima, Journal of alloys and Compounds, 456 (2008) 400-406.

[7] W. Liu, F. Cao, L. Chang, Z. Zhang, J. Zhang, Corrosion Science, 51(2009) 1334-1343.

[8] J. Cai, G.C. Ma, Z. Liu, H.F. Zhang, A.M. Wang, Z.Q. Hu, Materials Science and Engineering A, 456 (2007) 364-367.

[9] I.A. Anyanwu, Y. Gokan, A. Suzuki, S. Kamado, Y. Kojima, S. Takeda, Materials Science and Engineering A, 380 (2004) 93-99.

[10] N. Balasubramani, M. Suresh, A. Srinivasan, U.T.S. Pillai, B.C. Pai, Journal of Materials Science, 42 (2007) 8374-8376.

[11] M. Shahzad, L. Wagner, Scripta Materialia, 60 (2009) 536-538.

[12] M. Shahzad, L. Wagner, Journal of Alloys and Compounds, 486 (2009) 103-108.

[13] N. Stanford, M.R. Barnett, Materials Science and Engineering A, 496 (2008) 399-408.

[14] T. Al-Shamman, X. Li, S.G. Chowdhury, Materials Science and Engineering A, 527 (2010) 3450-3463.

[15] J. Bohlen, S. Yi, D. Letzig, K.U. Kainer, Materials Science and Engineering A, 527 (2010) 7092-7098.

[16] J. Bohlen, M.R. Nurnberg, J.W. Senn, D. Letzig, S.R. Agnew, Acta Materialia, 55 (2007) 2101-2112.

[17] N. Stanford, M.R. Barnett, Materials Science and Engineering A, 496 (2008) 399-408.

[18] B.L. Wu, Y.H. Zhao, X.H. Du, Y.D. Zhang, F. Wagner, C. Esling, Materials Science and Engineering A, 527 (2010) 4334-4340.

[19] N. Stanford, Materials Science and Engineering A, 527 (2010) 2669-2677.

[20] N. Stanford, M Barnett, Scripta Materialia, 58 (2008) 179-182.

[21] R.K. Mishra, A.K. Gupta, P.R. Rao, A.K. Sachdev, A.M. Kumar, A.A. Luo, Scripta Materialia, 59 (2008) 562-565.

[22] N. Stanford, D. Atwell, A. Beer, C. Davies, M.R. Barnett, Scripta Materialia, 59 (2008) 772-775.

[23] S.S. Park, B.S. You, D.J. Yoon, Journal of Materials Processing Technology, 209 (2009) 5940-5943.

[24] S.M.F. Varzaneh, A.Z. Hanzaki, H. Beladi, Materials Science and Engineering A, 456 (2007) 52-57.

[25] T. Laser, C. Hartig, M.R. Nurnberg, D. Letzig, R. Bormann, Acta Materialia, 56 (2008) 2791-2798.

Chapter 5 Static mechanical properties of extruded Mg alloys fabricated by rapid solidification powder metallurgy

In this chapter, the static mechanical properties such as hardness, tensile and compression properties of the extruded magnesium alloys have been discussed. The mechanical anisotropy of both AMX602 and ZAXE1711 alloys has also been discussed and correlated to the texture formation pattern shown in chapter 4.

5.1. Introduction

The alloys investigated herein have shown considerable improvement in the microstructure for processing via rapid solidification powder metallurgy compared to the conventional casting routes, as shown in chapter 4 [1-3]. The fine grain sizes and the homogeneous distribution of fine intermetallic compounds are effective to improve the mechanical properties of metallic materials, especially magnesium and its alloys. This effect has been shown through Hall-Petch relationship in which the strengthening factor of magnesium is higher that that of other metals [4].

Previously, the improvements in the mechanical properties of magnesium alloys has been obtained using several ways, including but not limited to, chemical alloying and thermo-mechanical processing methods. Honma et.al. reported attaining 473 MPa yield strength, 542 MPa tensile strength and 8% elongation for 1.8%Gd-1.8%Y-0.69%Zn-0.16%Zr Mg alloy produced through hot extrusion followed by aging treatment [5]. Similar Mg-10Gd-2Y-0.5Zr alloy has also showed good performance in the as-extruded

form with better elongation of 15.3%, but lower tensile strength of 403 MPa [6]. Hot rolling was also used to produce ternary $Mg_{90.5}$ $Ni_{3.25}$ $Y_{6.25}$ (at. %) cast alloy consisting of long-period structure ordered phase, which resulted in 460 MPa yield strength, 526 MPa ultimate tensile strength, and 8% elongation [7]. On the other hand, the processing routes for microstructure control like equal channel angular extrusion (ECAE) has also been employed to AZ31 alloy, which resulted in the ultimate tensile strength of 445 MPa [8]. Rapidly solidified powder metallurgy processing was also applied to produce Mg-Zn-Y alloy showing 410 MPa yield strength with 12% elongation [9]. Reinforcing AZ91D alloy with Si-coated carbon nano-fibers has also shown a maximum tensile strength of 470 MPa for 7.5% carbon nano-fibers, but with the elongation falling to 1.7% [10]. In the current study, however, the static strengthening effect of the combination of chemical alloying and powder metallurgy process has been discussed.

The texture pattern of the alloys concerned, shown using the EBSD analysis presented in chapter 4, suggests the improvement of the mechanical anisotropy of extruded magnesium alloys. Hence, it was also investigated for both AMX602 and ZAXE1711 alloys and correlated to the texture parameters of intensity of (0001) basal plane and the Schmid factor. The tensile and compression anisotropy of magnesium alloys has been reported to occur as a result of the texture formation during thermo-mechanical processing. They have been shown to be of totally different nature for the same alloy due to the different possibilities of twinning activation [11, 12]. In this study, the tensile and compression anisotropy, as well as their asymmetry, are discussed.

5.2. Hardness and tensile properties of extruded alloys

5.2.1. Hardness and tensile properties of extruded AMX602 alloy

The dependence of both hardness and tensile properties on the extrusion temperature is shown in Fig. 5.1 and 5.2. Generally, the higher the extrusion temperature, the lower the hardness, yield, and tensile strengths and the higher the elongation of extruded AMX602 alloy. That can be attributed to the strain hardening that occurs during plastic deformation of the extrusion process, which is increased in the case of extrusion at lower temperatures. It is also shown from both figures that the extruded SWAP powder could show hardness and tensile properties superior to that of cast billets while maintaining reasonable levels of elongation. This is due to the finer size of both grains and precipitated compounds of extruded SWAP powders compared to that of cast billets, as shown in chapter 4. The increase of the yield and tensile strengths of extruded SWAP powder via cold compaction have gain improvements of 68% and 44% over that of extruded cast billets, respectively. Surprisingly, this improvement in tensile and yield strengths are accompanied with levels of elongation for extruded SWAP powder specimens which are comparable to those of extruded cast ones. That indicates the remarkable effect of powder metallurgy processing to improve the tensile properties of magnesium alloys compared to the conventional cast alloys.

These values of mechanical properties are superior to many other reported values of different alloys processed by severe warm working process [13] or by rapid solidification [14, 15]. The mechanical response of consolidated billets produced via SPS without extrusion is expected to be

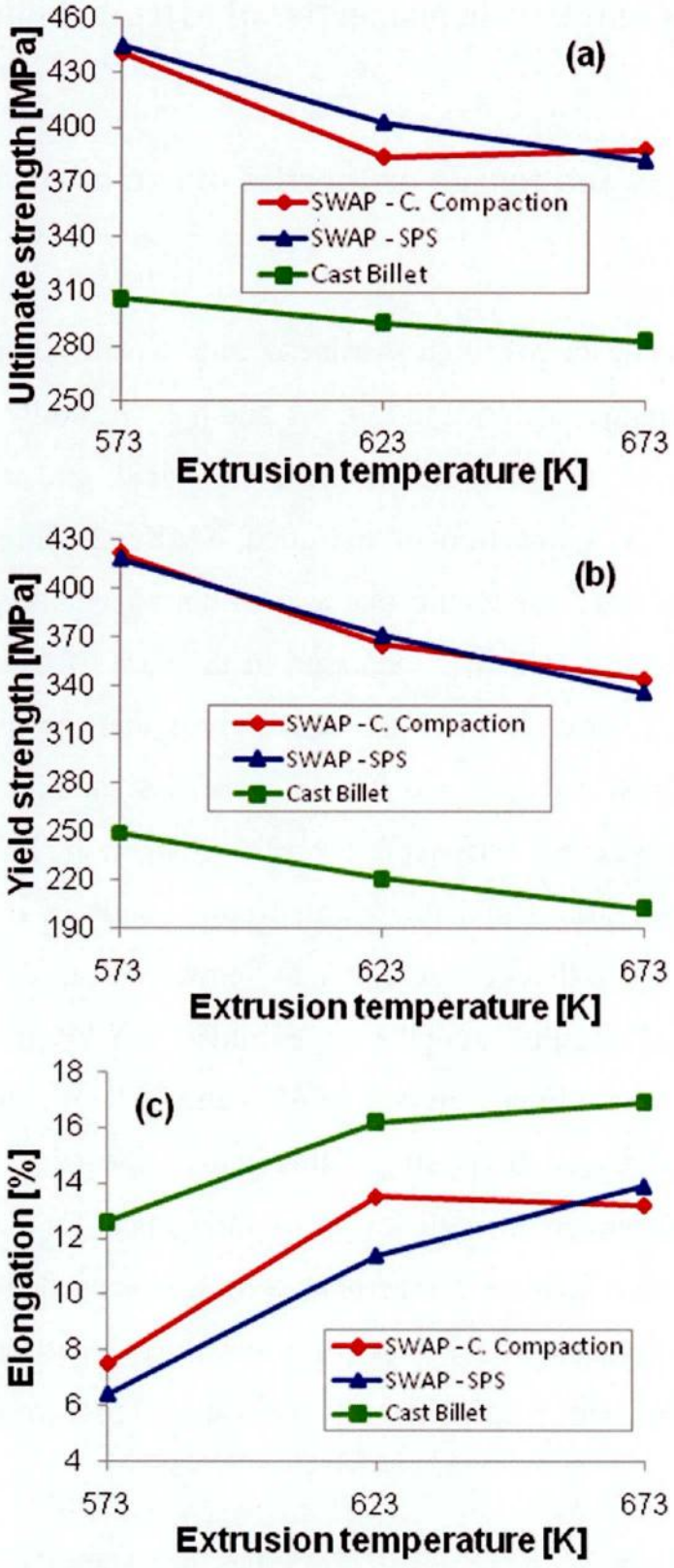

Fig. 5.1 Tensile strength (a), yield strength (b) and elongation (c) of extruded AMX602 alloy SWAP powder and cast billets.

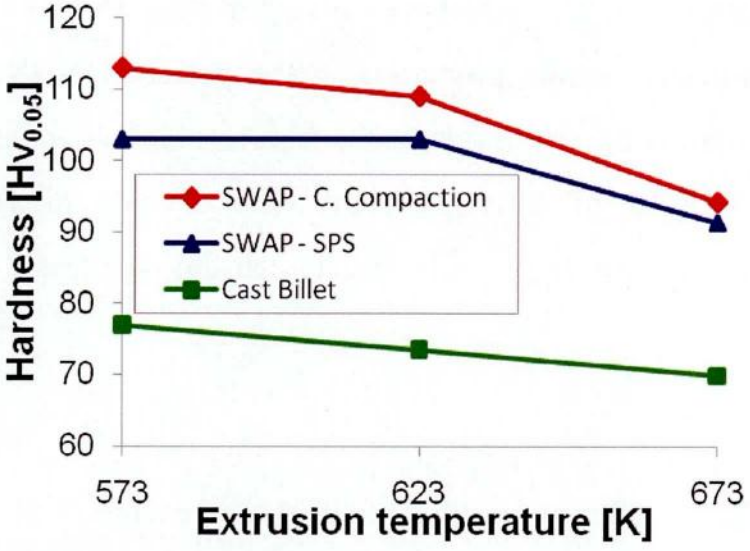

Fig. 5.2 Hardness of extruded AMX602 alloy SWAP powder and cast billets.

improved due to the effect of the strong bonding between primary powder particles as well as due to minimized grain growth compared to the conventional sintering [16]. However, the effect of SPS on the mechanical response of the extruded materials is less in this study as the extrusion temperatures are higher than the temperature in SPS and as it is compared only to that of cold compaction process in which no heating is used during consolidation.

As for the purpose of comparison and checking the effect of precipitation, the tensile properties of specimens consolidated and extruded at higher temperatures are shown in Table 5.1. The values are much lower than those SWAP powders extruded in the range of 573 to 673 K. They are comparable to the results of extruded cast billets reported herein or elsewhere [17]. This is due to the coarsened grain size of higher temperature extrusion. As it was shown in chapter 4, these specimens contained the same intermetallic compounds, but with different morphologies. Different sizes of the precipitated Al_2Ca compound particles were detected and ranged from

about 0.3 microns and less (the order of grain size) to about 10 microns. These low values of tensile properties in the presence of the precipitated compounds recommended that the mechanism responsible for improving the strength in AMX602 alloy is the refinement of both α-Mg grains and intermetallic compound dispersoids rather than the compound precipitation itself.

Table. 5.1 The tensile properties of cold compacted AMX602 SWAP specimens extruded at higher temperatures

Extrusion temperature	UTS [MPa]	YS [MPa]	El. [%]
793 K	365	283	16.6
823 K	334	236	14.3

The tensile results of the extruded SWAP AMX602 alloy powder suggest that the strength of magnesium alloys can be effectively improved through grain refining. Only a slight decrease within extruded SWAP powder in the grain size by extrusion at lower temperature could lead to a drastic increase in the strength, as shown in Table 5.1. The same behavior could also be observed for extruded cast billet specimens. Plotting the yield strength versus $(1 / \sqrt{d})$, where "d" denotes the mean grain size, shows the effect of grain refinement on the strength of Mg-Al-Mn-Ca magnesium alloy, as shown in Fig. 5.3. The strengthening factor is shown to have the value of 0.185 MPa $\sqrt{m}$, which corresponds well to the previously reported values (0.2 ~ 0.34 MPa $\sqrt{m}$) [4]. This value means that the use of SWAP process to produce AMX602 powder alloy resulted in the improved mechanical properties through the effect of grain refinement.

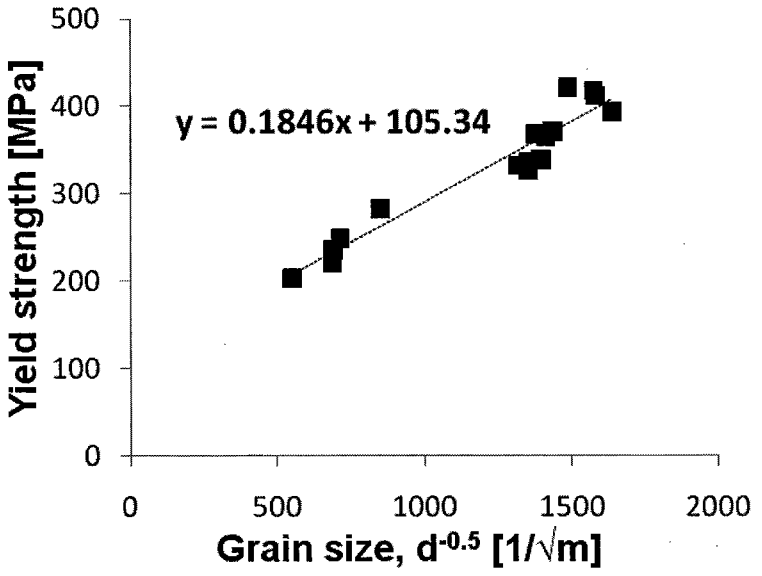

Fig. 5.3 Hall-Petch relationship of extruded AMX602 alloy.

Fractography of the fractured tensile test specimens, as some examples are shown in Fig. 5.4, reveals no evidence of powder particle primary boundary separation, proving that sufficient bonding between powder particles cold be obtained at the extrusion temperatures used. Generally, the fracture surfaces of all the fractured specimens show dimple-fractured pattern as an indication for ductile fracture. However, the size of dimples varied slightly among different consolidation and extrusion conditions of SWAP powders having an average of 0.8 microns, and showed larger size for extruded cast billets with an average of 5 microns. It could also be evident that the coarse intermetallic compounds in the extruded cast alloy have fractured under tensile loading due to their lack of ductility, resulting in degradation rather than strengthening. In contrast, no sign of such fracture of intermetallic compounds could be noticed in the case of fine compounds of extruded SWAP powder specimens.

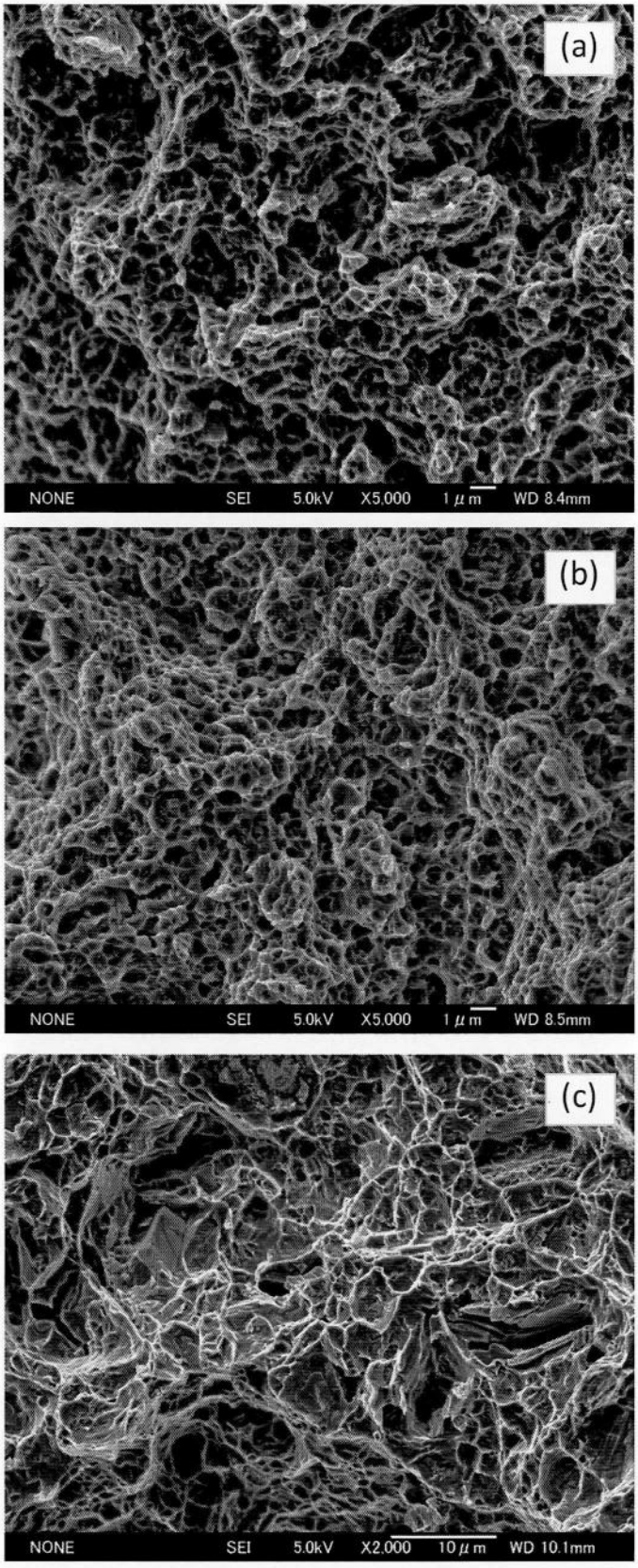

Fig. 5.4 Fractography of tensile test samples of AXM602 alloy SWAP powder cold compacted (a), SPS at 473 K (b) and cast (c) extruded at 673 K.

5.2.2. Hardness and tensile properties of extruded ZAXE alloys

Figure 5.5 shows the dependence of tensile properties on the extrusion temperatures for both ZAXE1711 and ZAXE1713 alloys. Similar to that of extruded AMX602 alloy, the higher the extrusion temperature, the lower the yield, and tensile strengths of extruded ZAXE alloys and the lower the elongation. That can be attributed to the strain hardening that occurs during plastic deformation of the extrusion process, which is increased in the case of extrusion at lower temperatures. Figure 5.5 also indicates that the extruded SWAP powders could show tensile properties superior to that of cast billets, as the tensile strength for extruded cast materials had an average of 290 MPa and the yield strength had an average of 195 MPa for both alloys while the tensile strength of extruded SWAP powder could reach 450 MPa. This is due to the finer size of both α-Mg grains and precipitated compounds of extruded SWAP powder alloys compared to that of cast billet materials. The extruded SWAP powder of ZAXE1711 has shown tensile properties that are much improved over that of SWAP powder of ZAXE1713. That can be attributed to the coarsening of precipitated compounds for the latter as a result of the increased amount of La in ZAXE1713 alloy. It can also be shown from Fig. 5.5 that the use of rapidly solidified SWAP Mg powders alloyed with La additions could lead to improved levels of tensile strength while maintaining promising values of elongation in the range of 13 to 20%. A good balance of high strength and enough elongation enables the investigated alloys produced using SWAP powder metallurgy to get more applications in automotive industry. It is even superior to, for example, rapidly solidified Mg-Zn-Ce-Ag alloy [18], powder metallurgy processed AZ91 alloy [19], and AMX602 alloy [1]. It can also be shown that the extruded SWAP powder alloys have shown superior properties compared to that of extruded cast

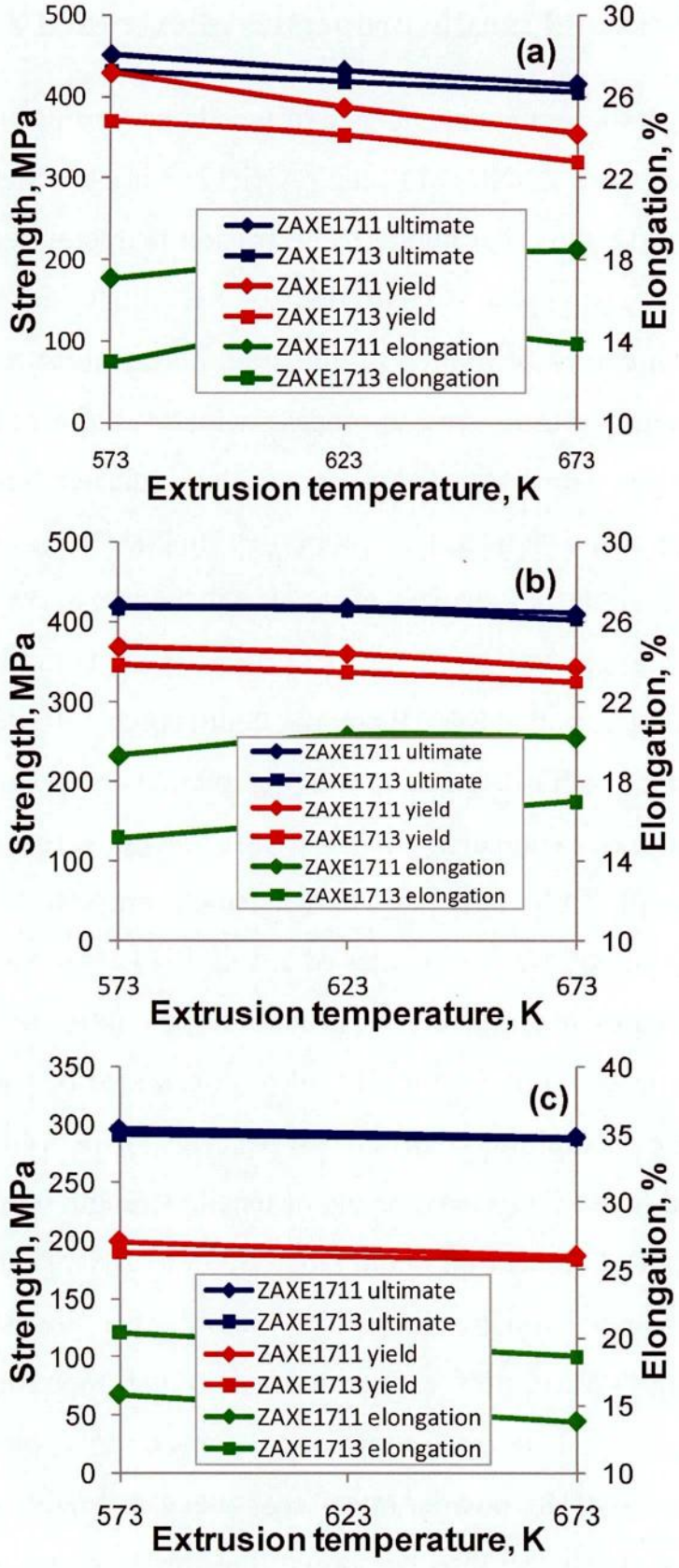

Fig. 5.5 Tensile properties of extruded ZAXE alloys SWAP powder. Cold compacted (a), SPS at 623 K (b) and cast billets.

alloys. These results prove the competence of rapidly solidified powder metallurgy to improve the static mechanical properties of Mg alloys.

The effect of SPS on the mechanical response of the extruded materials in this study is minor, compared to cold compacted ones, as a result of the dominant dynamic recrystallization effect of the hot extrusion process. As a result of coarser intermetallic compound particles, SPS processed extrusions have shown lower tensile strength but slightly higher elongation than that of cold compacted ones. For the purpose of investigating the effect of SPS temperature on the properties of the extruded SWAP powders, the tensile properties of specimens SPS processed at 473 and 573 K were compared to that of samples SPS processed at 623 K and extruded at the same temperature of 573 K, as shown in Fig. 5.6. The results show that the tensile strength increased as the SPS temperature decreased. It increased from 420 to 450 MPa when the SPS temperature was decreased from 623 to 473 K for ZAXE1711 alloy, and from 415 to 430 MPa for ZAXE1713 alloy. This is mainly due to the sizes of α-Mg grains and intermetallic compounds, which have been shown to decrease as the SPS temperature decreases.

The hardness of the extruded SWAP powders reveals a similar pattern to that of tensile properties, in which the hardness in increased as the extrusion temperature decreased, as shown in Fig. 5.7. Meanwhile, the hardness values of the extruded SWAP powders are superior to that of extruded cast alloys, a trend that is also consistent with that of tensile properties. It can be also shown that the ZAXE1711 alloy specimens attain hardness values higher than those of extruded ZAXE1713 alloy ones, following the pattern of tensile properties.

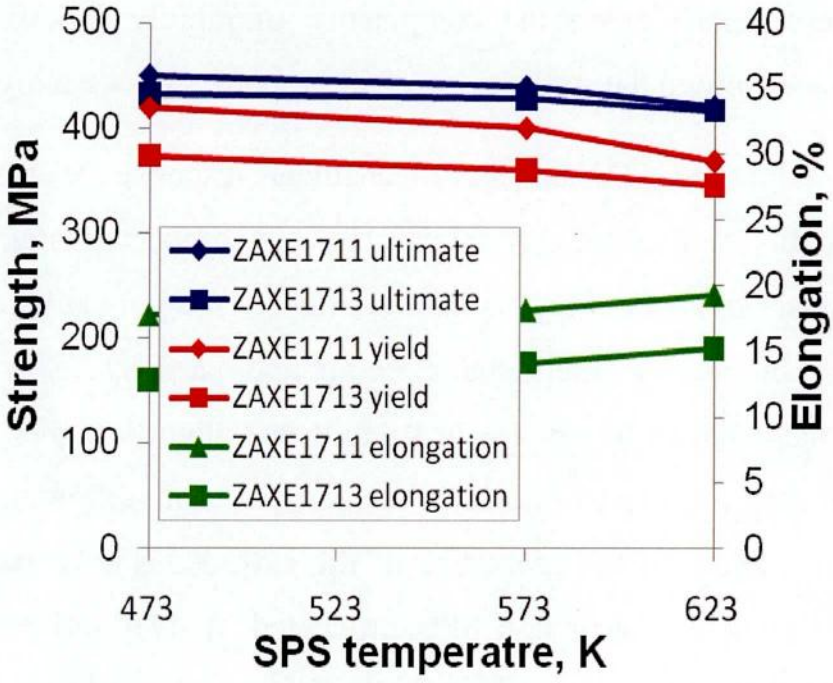

Fig. 5.6 The tensile properties of ZAXE alloys extruded at 573 K as a function of the SPS temperature.

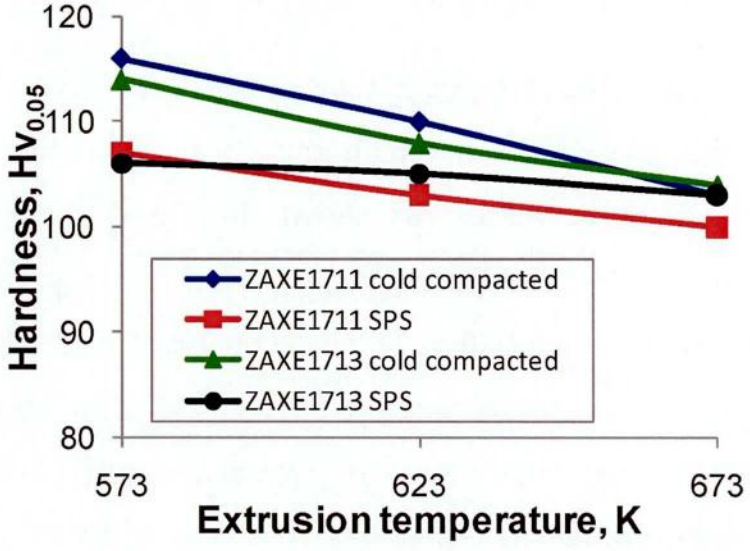

Fig. 5.7 Hardness of extruded SWAP powder of ZAXE alloys.

By plotting the yield strength of both extruded SWAP powders and cast specimens of ZAXE1711 and ZAXE1713 alloys against their corresponding values of $(1/\sqrt{d})$, where d is the mean grain size, according to Hall-Petch relationship, it becomes clear that grain refinement plays an important role in increasing the strength of both alloys, as shown in Fig. 5.8. The value of the strengthening factor "k" of 0.17 MPa $\sqrt{m}$ is slightly lower than previously reported values of Mg alloys as that value includes data of both SWAP powders and cast alloys [4]. Excluding the data of extruded cast specimens from the figure brings the strengthening factor to the value of 0.2 MPa $\sqrt{m}$, which falls in the same range of previously reported values. This means that yield strength of Mg alloys is well related to the grain size as exactly expressed by Hall-Petch relationship.

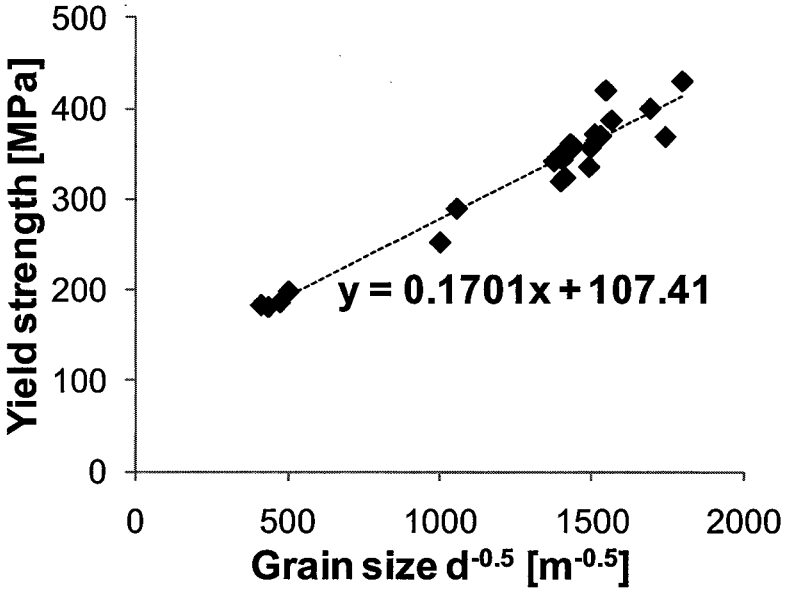

Fig. 5.8 Hall Petch relationship of extruded ZAXE alloys.

Similar to that of extruded AMX602 alloy, the Fractography of the fractured tensile test specimens showed that sufficient bonding between powder particles could be obtained at the extrusion temperatures used, as no evidence of primary particle boundary separation was observed at the fracture surface, even for specimens extruded at 573 K, which was the lowest extrusion temperature, as shown in Fig. 5.9 (a) and (b). Generally, the fracture surface of all the fractured specimens showed dimpled pattern as an indication for ductile fracture. However, the size of dimples varied slightly among different consolidation and extrusion conditions of SWAP powders. It can also be shown from Fig. 5.9 (c) that the fracture of the brittle coarse intermetallic compounds worked as initiation sites for micro-cracks, marked with an arrow in the figure, which have decreased the elongation of extruded cast specimens to the same level or less than that of extruded SWAP powders while having much lower values of yield and ultimate strengths. That fracture has been avoided in the case of extruded SWAP powders as a result of the small size of compound particles. The EDS analysis results of the fractured intermetallic compound particles, shown in Fig. 5.10, revealed that this kind of fracture occurred in both Al_2Ca and $Al_{11}La_3$ compound particles, especially ones which have larger sizes. That finding supports the aforementioned claim that the strength of extruded magnesium alloys investigated herein has been modified through the refinement of both grains and intermetallic compound particles.

The above results show that the strength of magnesium alloys can be improved through grain refinement. Only a slight decrease in the grain size by extrusion at lower temperature could lead to a drastic increase in the strength. The same behavior could also be observed when comparing extruded SWAP powder with extruded cast billet specimens.

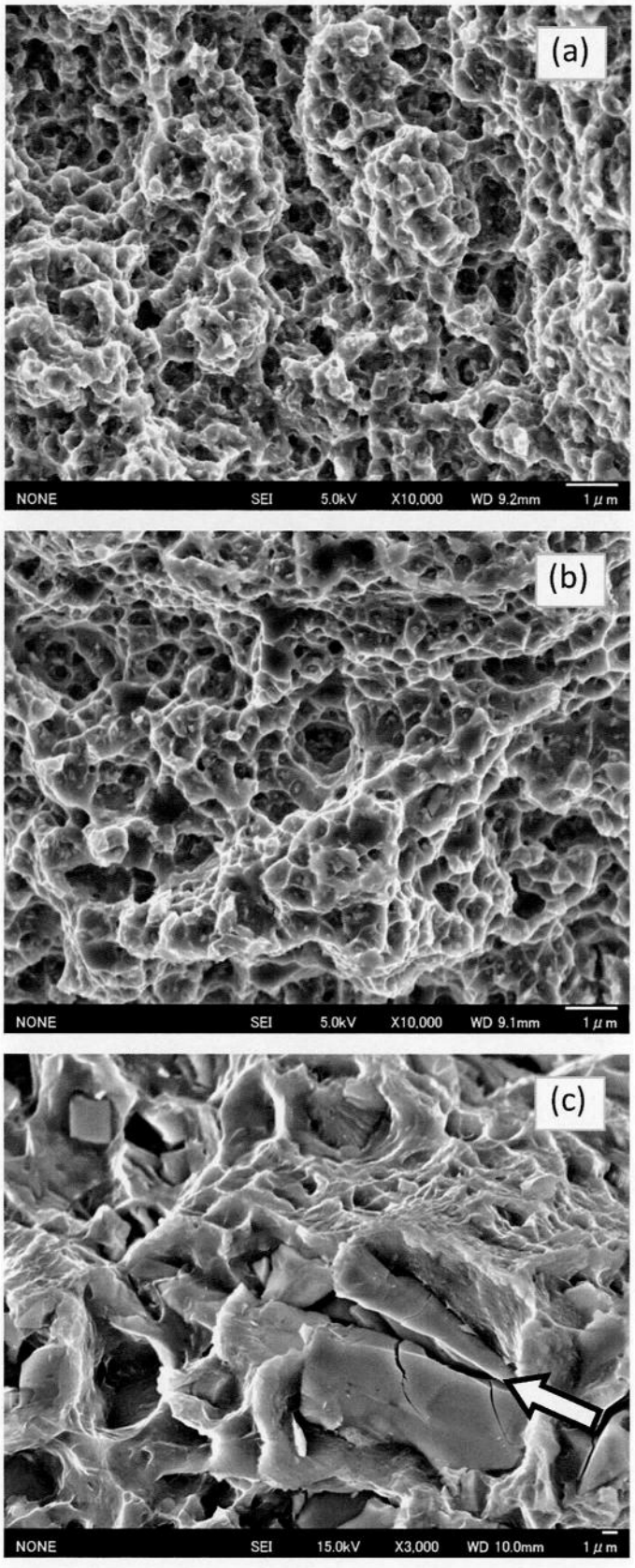

Fig. 5.9 Fractography of tensile test samples of ZAXE1711 alloy SWAP powder cold compacted (a), SPS at 623 K (b) and cast (c) extruded at 573 K.

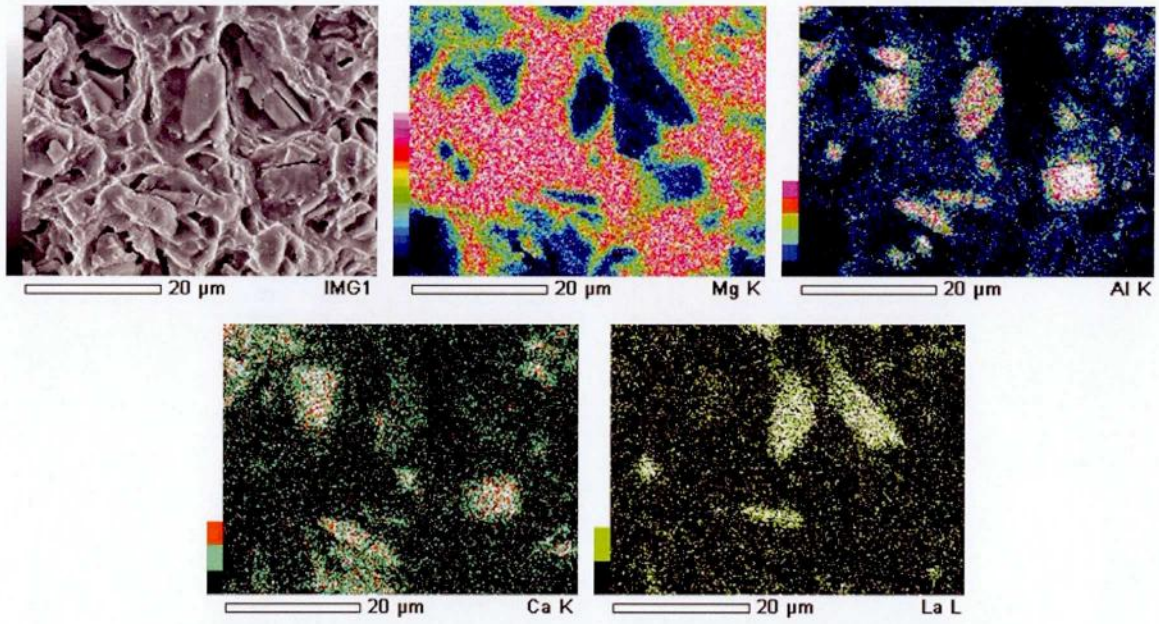

Fig. 5.10 EDS of fracture surface of tensile test specimen of ZAXE1711 cast alloy extruded at 573 K.

5.2.3. Hardness and tensile properties of extruded ZK61 alloy

The dependence of tensile properties on the extrusion temperatures is shown in Fig. 5.11. The higher extrusion temperature causes the lower yield and tensile strengths of extruded ZK61 alloy. That can be attributed to the strain hardening that occurs during plastic deformation of the extrusion process, which is increased in the case of extrusion at lower temperatures. This leads to the formation of finer microstructures that finally lead to the improved mechanical response. It can also be shown that specimens sintered at lower temperatures revealed better tensile properties compared with those sintered at higher temperatures. This can be attributed to the limited grain growth associated with SPS process at lower temperatures. It can also be shown from Figure 5.11 that the use of rapidly solidified atomized Mg powders could lead to improved levels of tensile strength while maintaining promisingly suitable values of elongation in the range of 10 to 22 %, except

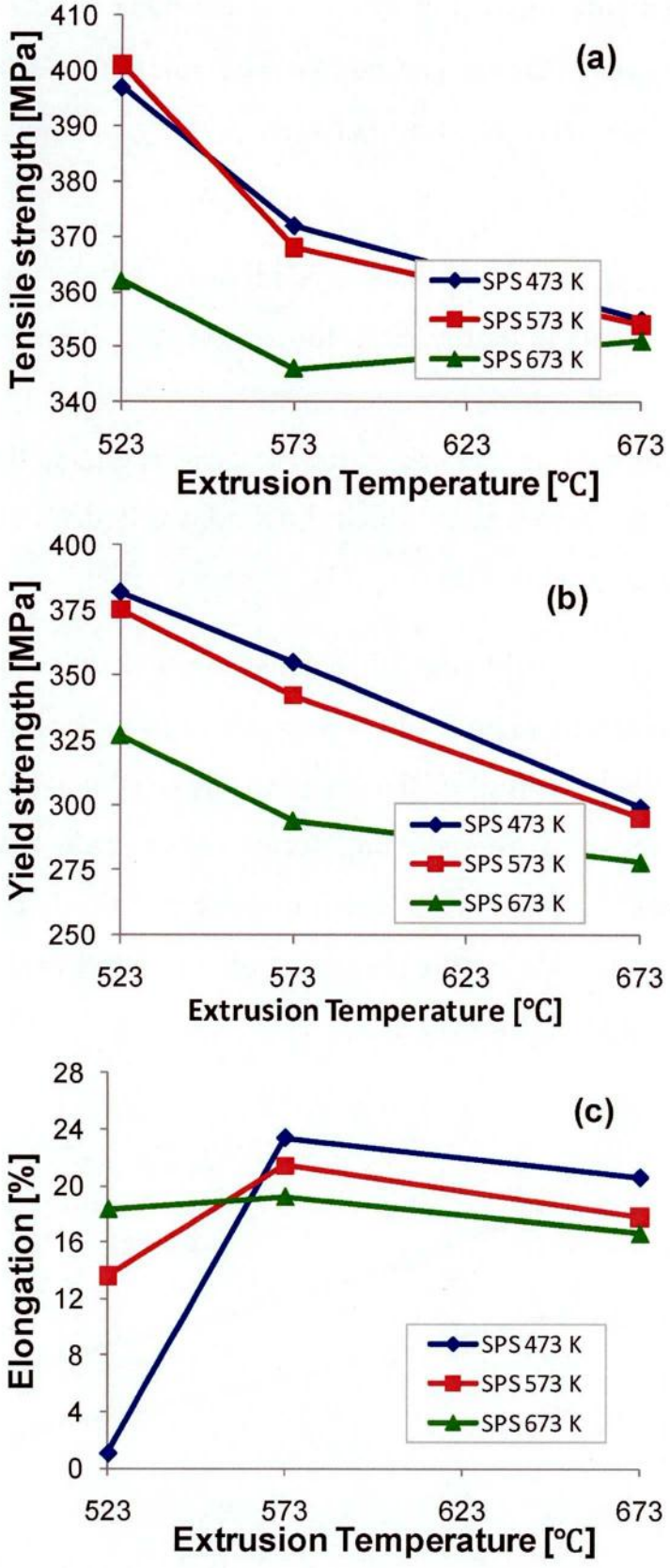

Fig. 5.11 Tensile strength (a), yield strength (b) and elongation (c) of extruded ZK61 alloy atomized powder.

for the specimen consolidated at 473 K and extruded at 523 K. This result shows that the consolidation conditions used for this specimen were not enough to produce good bonding between primary powder particles after extrusion.

The hardness values of the extruded ZK61 alloy powder showed a decrease in the hardness as the extrusion temperature increased a behavior that is consistent with that of tensile properties, as shown in Figure 5.12. The effect of the sintering temperature on the hardness is almost the same as that of the extrusion temperature, in which the hardness is decreased as the SPS temperature is increased.

By plotting the yield strength against the inverse of the root of the grain size, as shown in Figure 5.13, the effect of grain refinement becomes clear on the tensile properties of the extruded ZK61 alloy, according to Hall-Petch relationship. The strengthening factor in this case has the value of about 0.22 $MPam^{-0.5}$, which is consistent to those previously reported as 0.17 to 0.22 MPa $m^{-0.5}$, and shows the promising effect of grain refinement on the tensile response of Mg-alloys [4].

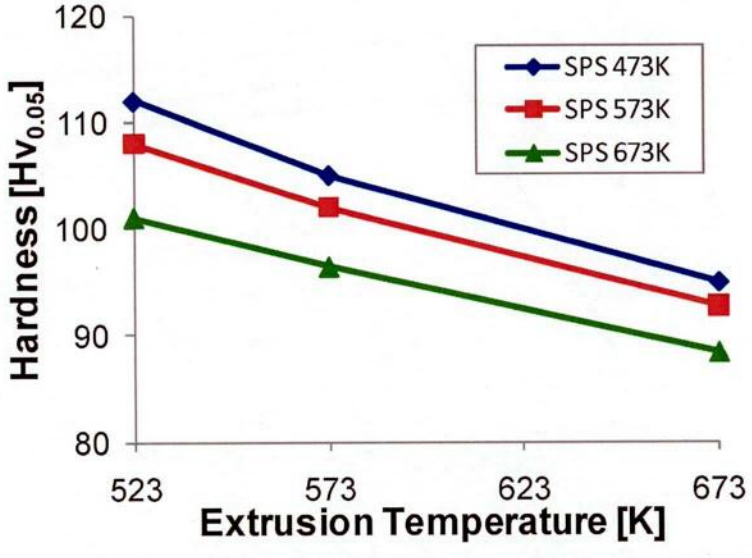

Fig. 5.12 Hardness of extruded ZK61 alloy atomized powder.

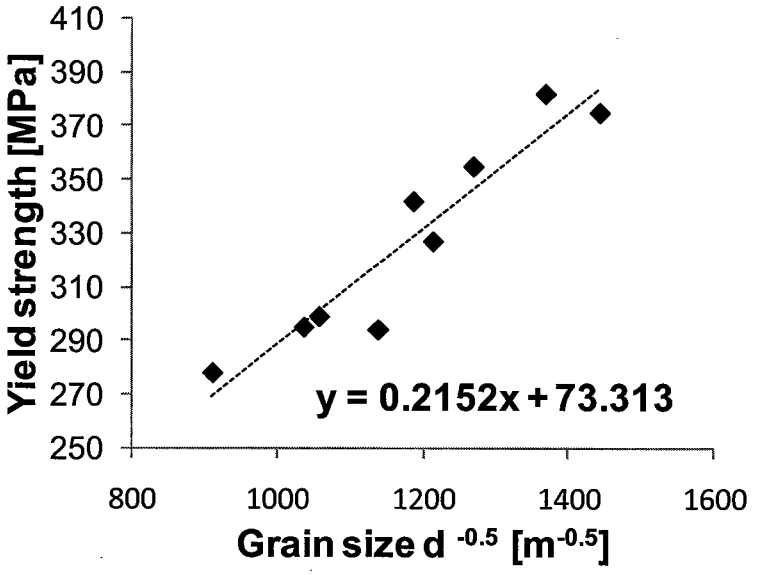

Fig. 5.13 Hall-Petch relationship of extruded ZK61 alloy atomized powder.

Fractography of the fractured tensile test specimens showed that sufficient bonding between raw powder particles could be obtained at the extrusion temperatures used, as no primary particle boundary was observed at the fracture surface, as shown in Figure 5.14. Generally, the fracture surface of all the fractured specimens after tensile test showed dimpled pattern as an indication of ductile fracture. However, the size of dimples varied slightly among different consolidation and extrusion conditions of atomized powders. However, other signs of brittleness could also be seen in terms of small microcracks. Those microcracks have hardly contributed to the final ductility as they did not coalesce with each others. The above micrographs of the fracture surfaces of tensile test specimens showed no explanation of the reduced ductility in the specimen of SPS at 473 K and extruded at 523 K. However, the fracture macrograph showed clear sign of the lack of bonding between primary powder particles, as shown in Fig. 5.15.

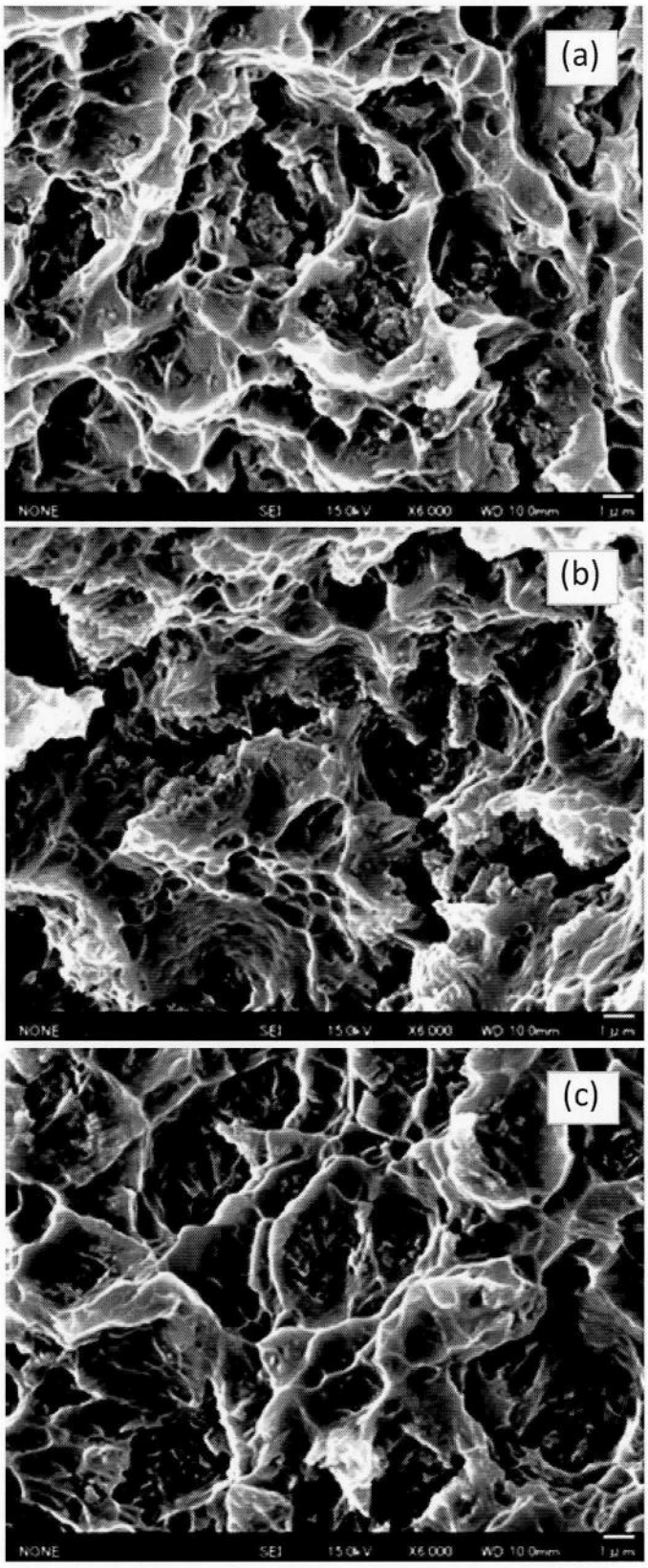
(a)
NONE SEI 15.0kV X6,000 WD 10.0mm 1 μm
(b)
NONE SEI 15.0kV X6,000 WD 10.0mm 1 μm
(c)
NONE SEI 15.0kV X6,000 WD 10.0mm 1 μm

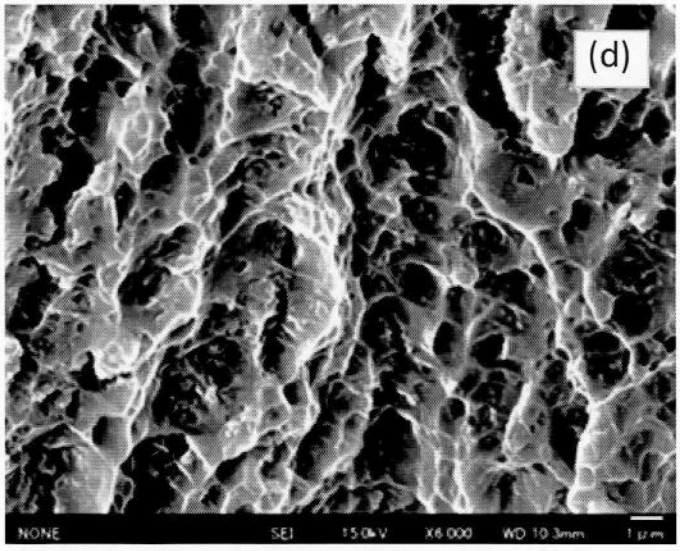

Fig. 5.14 Fractography of tensile test samples of ZK61 alloy atomized powder SPS at 673 and extruded at 673 K (a), 523 K (b), SPS at 473 K and extruded at 673 K (c) and 523 K (d).

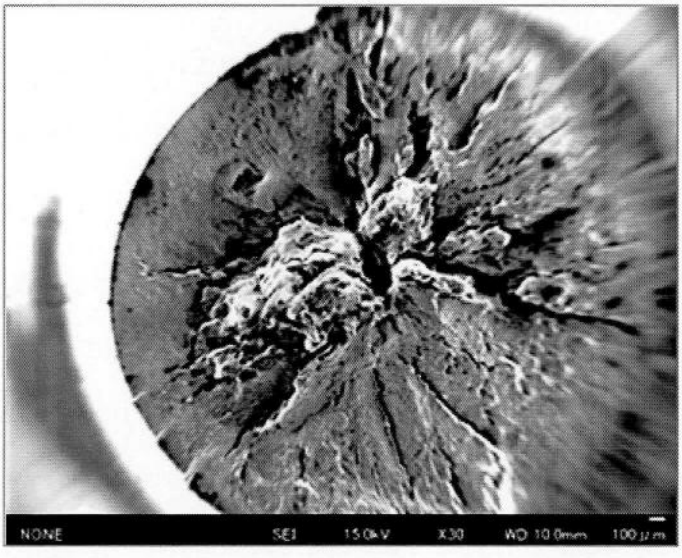

Fig. 5.15 Fracture macrograph of tensile test samples of ZK61 alloy atomized powder SPS at 473 and extruded at 523 K.

5.3. Anisotropy of extruded AMX602 and ZAXE1711 alloys

The above mentioned tensile and hardness properties of the alloys investigated shows generally much improvement in the mechanical properties of magnesium alloys. However, it was of a great importance to characterize the anisotropy of the alloys for better understanding of their behaviors. Hence, the tensile test results at 0, 45 and 90° angles from the extrusion direction of both AMX602 and ZAXE1711 alloys, which were selected for this study, are shown in terms of the stress-strain plots in Fig. 5.16. In order for that, bigger size extrusions of 25 x 40 mm rectangular cross-section extruded rods have been prepared to enable sampling in different sample orientations. It can be shown that the extruded AMX602 alloy SWAP powder specimen possesses higher values of yield and ultimate stresses while maintaining reasonable levels of ductility compared to that of extruded cast specimens. They are also superior to previously reported values of the strength of Mg alloys via conventional routes. However, these results are lower than those presented earlier in this chapter for smaller extrusions of 7 mm extruded bars of the same alloys.

Generally, both yield and ultimate strengths have decreased as the angle of the loading has increased from 0 to 45 and 90°. The elongation has also decreased simultaneously. However, the difference of both ultimate and yield strengths are much lower in the case of extruded SWAP powders than those for extruded cast billets. It could be shown from the figure that the extruded cast alloy shows more anisotropy than that of extruded SWAP powders in terms of wider difference in both yield strength and elongation at various directions, which is more noticeable for elongation levels. This could be linked to the signs of more randomized texture formation of extruded SWAP powders in terms of lower intensity of the (0001) basal plane, as shown in chapter 4. Also, comparing Figs. 5.16 (a) and (C) together shows

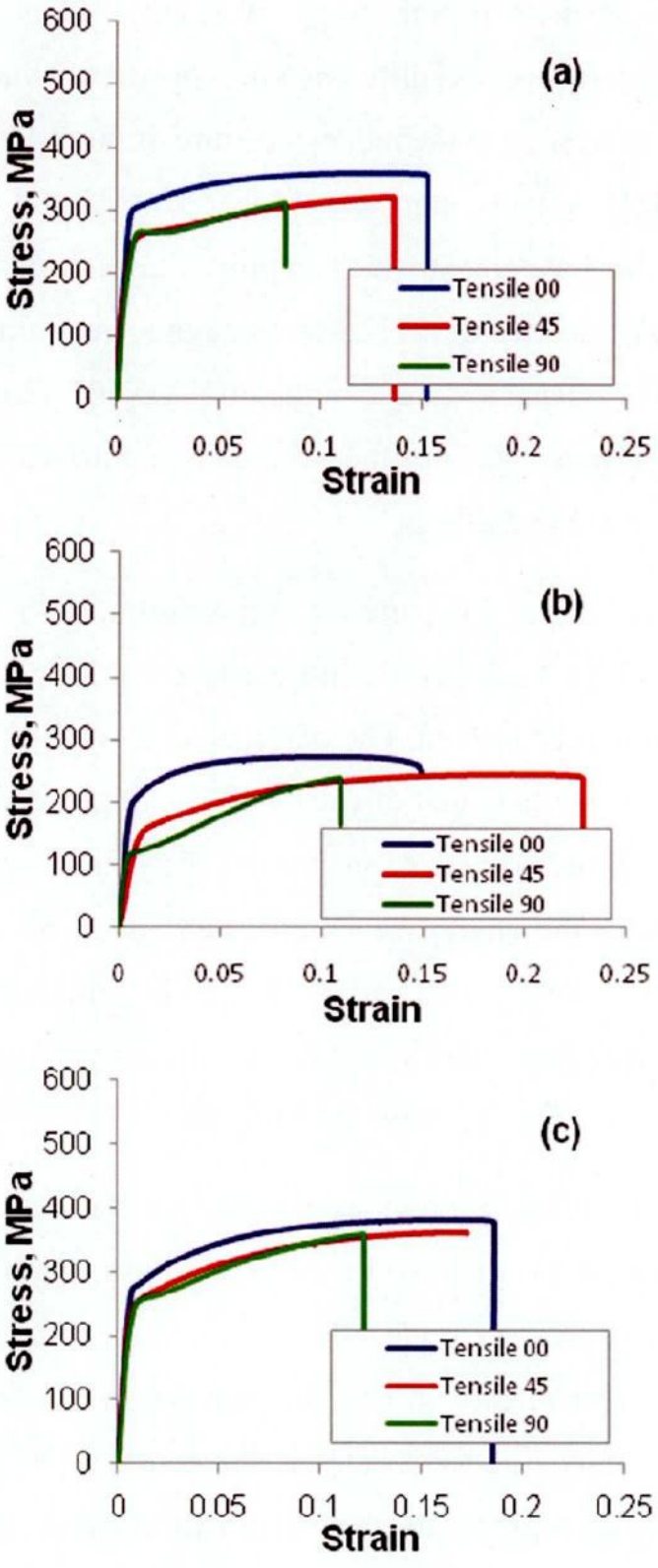

Fig. 5.16 Tensile stress-strain curves of large size extrusion rods (Extruded at 673 K) of AMX602 alloy SWAP powder(a), cast (b) and ZAXE1711 alloy SWAP powder at various orientations with respect to the extrusion direction.

the considerable decrease in anisotropy of ZAXE1711 alloy than that of AMX602 alloy in terms of less difference in properties at various directions. This also can be correlated to the reduced texture of the ZAXE1711 alloy, as shown in the EBSD patterns, compared to that of AMX602 alloy as a result of the alloying with La element which improves texture randomization. The latter was shown in the ZAXE1711 alloy through lower values of maximum intensity of the basal plane texture than that of AMX602 alloy. This was also accompanied by higher values of the average Schmid factor of ZAXE1711 alloy than that of AMX602 alloy.

This behavior has also occurred in compression, as shown in Fig. 5.17. However, both alloys have shown more strain hardening in the case of compression than that of tension. The extruded cast AMX602 alloy has also shown more anisotropy than that of extruded SWAP powders. In contrast to the previously reported pattern of increasing the compression/tensile yield strengths' ratio with the angle, the investigated alloys SWAP powder has shown almost the same values of both tensile and compression yield strengths at all directions, with the ratio equals unity. This can be shown when comparing both Figs. 5.16 and 5.17 together.

It has been shown in previous reports that the Ca element has the effect of weakening of the texture of Mg alloys through the random nucleation of recrystallized grains due to the formation of intermetallic compounds [20]. This effect can also be observed in this study in terms of the decreased maximum intensity of the basal texture of the extruded SWAP powder specimen compared to that of extruded cast due to the fine distribution of intermetallic compounds, which never occurred in the case of extruded cast alloy. Hence the decreased asymmetry of both tensile and compression results in various directions can be explained through the effect of randomized nucleation of recrystallized grains stimulated by compound

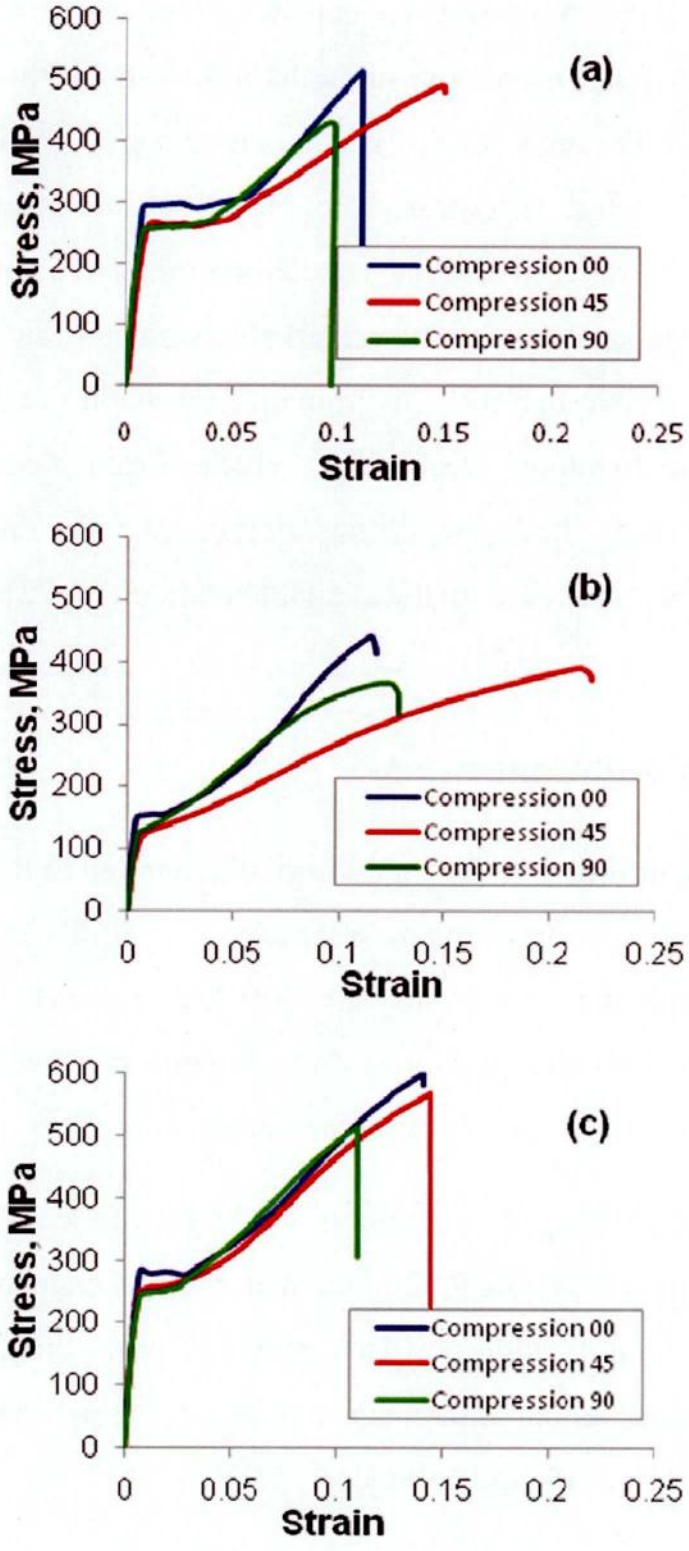

Fig. 5.17 Compression stress-strain curves of large size extrusion rods (Extruded at 673 K) of AMX602 alloy SWAP powder(a), cast (b) and ZAXE1711 alloy SWAP powder at various orientations with respect to the extrusion direction.

particles. This claim may also be supported by the observation of the decreased tensile and compression strengths from 0 to 45°, and the similarity of both of 45 and 90° angle results, which can be correlated to orientation of the basal plane being randomized in both the normal and transverse directions. On the other hand, the tensile-compression isotropy shown in both alloys can be attributed to the remarkably refined grain sizes, as it has been previously shown that the fine grain size results in the difficulty of the activation of the twinning mechanism, which if activated results in the remarkable softening behavior during deformation in either tensile or compression directions based on the available texture [21, 22].

5.4. Summary and Conclusion

Rapidly solidified powder metallurgy was applied to the fabrication of high strength and ductility of magnesium alloys. Their hardness, tensile and compression properties were investigated and correlated to both the microstructure and texture evolutions during thermo-mechanical processing. The following conclusions can be drawn from these results:

- High strength magnesium alloys could be fabricated by using the combination of chemical alloying with various element combinations and rapid solidification powder metallurgy processing, owing to their advantages of grain refinement and homogeneous dispersion of fine intermetallic compound particles.

- Higher strength of magnesium alloys can be obtained by lower temperature extrusions provided that enough bonding between powder particles can be attained at the conditions used.

- Grain refinement could be shown of a great effect to improve the strength of magnesium alloys.

- The tensile strength value of up to 450 MPa for cold compacted ZAXE1711 alloy powder extruded at 573 K is an excellent example for the improvement of mechanical properties of Mg alloys, especially with maintaining an elongation value of 17 %.

- For ZAXE alloy, A La content of 1.5 wt.% could lead to improved mechanical properties compared to that of 3.3 wt.% as a result of the good balance between the effects on grain refinement and precipitated compound formation.

- The extruded SWAP powders of magnesium alloys show superior anisotropy to those of extruded cast alloys due to the effects of randomized texture formation and extensive grain refinement.

- Alloying with La can further improve the anisotropy of magnesium alloys through its effects of fine particle stimulated nucleation of randomized textured grains.

References

[1] A. Elsayed, K. Kondoh, H. Imai, J. Umeda, Materials and Design, 31 (2010) 2444-2453.

[2] A. Elsayed, J. Umeda, K. Kondoh, Acta Materialia, 59 (2011) 273-282.

[3] A. Elsayed, H. Imai, J. Umeda, K. Kondoh, Steel Research International, 81-9 (2010) 1304-1307.

[4] P. Andersson, C.H. Caceres,J. Koike, Materials Science Forum, 419-422 (2003) 123-128.

[5] T. Homma, N. Kunito, S. Kamado, Scripta Materialia, 61 (2009) 644-647.

[6] S.M. He, X.Q. Zeng, L.M. Peng, X. Gao, J.F. Nie, W.J. Ding, Journal of Alloys and Compounds, 427 (2007) 316-323.

[7] T. Itoi, K. Takahashi, H. Moriyama, M. Hirohashi, Scripta Materialia, 59 (2008) 1155-1158.

[8] S.X. Ding, W.T. Lee, C.P. Chang, L.W. Chang, P.W. Kao, Scripta Materialia, 59 (2008) 1006-1009.

[9] E. Mora, G. Garces, E. Onorbe, P. Perez, P. Adeva, Scripta Materialia, 60(2009) 776-779.

[10] T. Honma, K. Nagai, A. Katou, K. Arai, M. Suganuma, S. Kamado, Scripta Materialia, 60 (2009) 451-454.

[11] E.A. Ball, P.B. Prangnell, Scripta Metallurgica et. Materialia, 31 (1994) 111-116.

[12] S.S. Park, B.S. You, D.J. Yoon, Journal of Materials Processing Technology, 209 (2009) 5940-5943.

[13] Y. Yoshida, K. Arai, S. Itoh, S. Kamado, Y. Kojima, Science and Technology of Advanced Materials, 6 (2005) 185-194.

[14] Q.J. Li, L. Wang, H.W. Cheng, H.F. Zhang, Z.Q. Hu, H.N. Cai, Materials Science and Engineering A, 474 (2008) 24-29.

[15] Y. Kawamura, A. Inoue, Materials Science Forum, 419-422 (2003) 709-714.

[16] T. Sasaki, T. Ohkubo, K. Hono, Acta Materialia, 57 (2009) 3529-3538.

[17] H. Ding, L. Liu, S. Kamado, W. Ding, Y. Kojima, Journal of Alloys and Compounds, 456 (2008) 400-406.

[18] J. Cai, G.C. Ma, Z. Liu, H.F. Zhang, A.M. Wang, Z.Q. Hu, Materials Science and Engineering A, 456 (2007)364-367.

[19] S.S. Ding, C. Ding, C.Z. Hua, Journal of Alloys and Compounds, 470 (2009) 17-22.

[20] T. Laser, C. Hartig, M.R. Nurnberg, D. Letzig, R. Bormann, Acta Materialia, 56 (2008) 2791-2798.

[21] D.L. Yin, J.T. Wang, J.Q. Liu, X. Zhao, Journal of Alloys and Compounds, 478 (2009) 789-795.

[22] J. Bohlen, S.B. Yi, J. Swiostek, D. Letzig, H.G. Brokmeier, K.U. Kainer, Scripta Materialia, 53 (2005) 259-264.

Chapter 6 Fracture toughness characterization of extruded magnesium alloys

In this chapter, the fracture toughness of magnesium alloys produced using rapid solidification powder metallurgy route has been investigated according to both ASTM E399 and ASTM E 1820 standards. In chapters 3 to 5, it was clarified that AMX602 alloy has shown promisingly high tensile properties. Hence, it was needed to characterize its fracture toughness properties; whish was strongly required in its application to structural components. While the plane strain fracture toughness test yielded non valid values, the crack tip opening displacement that was evaluated for the alloy has shown values of fracture toughness comparable to other conventional magnesium alloys, and even superior in some cases.

6.1. Introduction

The tensile and compression properties of magnesium alloys have been extensively studied in numerous references [1-10], as shown in previous chapters. However, there is no enough work has been dedicated for studying the fracture toughness of magnesium alloys. This lack of previous studies occurs despite the increasing importance of characterizing the fracture toughness of various materials when introducing them as a design solution for different applications. A few articles have discussed the fracture toughness of magnesium alloys, with their emphasis on the evaluation of both the plane strain fracture toughness (K_{IC}) and the crack tip opening displacement (CTOD] fracture parameters [11-20]. Very limited number of references has used the standard test methods for the evaluation of fracture toughness parameters, while others used the stretch zone analysis technique as a result of the difficulty of obtaining valid results for magnesium alloys

using reasonable specimen sizes [11]. In a rare example of fully using the ASTM E 399 standard [21], the fracture toughness of AZ91 cast alloy has been investigated in terms of both K_{IC} and J_{IC} fracture parameters. A valid K_{IC} value could be obtained for a thickness of 110 mm, and its value has been 21.7 MPa $m^{1/2}$. On the other hand, many references have reported various values of K_{IC} of magnesium alloys based on the stretch zone analysis with their emphasis on the effects of grain refinement, compound particle distribution and texture [12-20]. The fracture toughness of extruded pure magnesium depended on its grain size, with the value of K_{IC} ranging from 12.7 to 17.8 MPa $m^{1/2}$ [12]. Fracture toughness of extruded Mg-Zn alloy has also been shown to improve as a result of the solid solution strengthening with higher values of K_{IC} of 21.2 to 23.7 MPa $m^{1/2}$ [13]. Fracture toughness of AZ31 alloy has also been extensively investigated and was found, in both its extruded and rolled forms, to improve when the crack plane is normal to the extrusion or rolling directions [14-16]. Similar to that of the above mentioned pure magnesium, the trend of improving the fracture toughness of extruded AZ31 alloy has also been reported, but with higher values of K_{IC} of 22.7 to 24.9 MPa $m^{1/2}$ [17]. Equal channel angular extrusion has been shown to increase the fracture toughness of AZ31 alloy through its effects of both grain refinement and controlling the texture by inclining the basal plane to the processing angle [18]. Intermetallic compound particles dispersion has also been reported to improve the fracture toughness of various magnesium alloys, along with grain refinement, containing both Zn-Y and Ca-Zn alloying element combinations [19, 20]. However, the compound particles have also been reported to degrade the fracture toughness of AZ61 alloy when they tend to form micro voids during crack propagation, with K_{IC} values ranging from 11.4 MPa $m^{1/2}$ to 16.1 MPa $m^{1/2}$ [19].

Previously, the AMX602 alloy produced using rapidly solidified powder metallurgy has been shown to have very promising tensile properties,

as shown in chapters 3 to 5. Hence, this study is dedicated to the investigation of the fracture toughness of the above mentioned alloy using the standard ASTM procedure, as an effort for providing sufficient information about the mechanical performance of that alloy. The effect of rapid solidification process on the fracture toughness of extruded SWAP powder has been investigated comparing to that of extruded cast billet. The size of the extruded rods was much bigger in this study to allow the machining of the large fracture toughness test specimens, as well as to investigate the performance of the extruded alloy at more practical scales.

6.2. Experimental procedure

Extruded AMX602 alloy powder material, produced using spinning water atomization process (SWAP), was investigated and compared to that of extruded cast billet. That alloy was previously introduced and shown to have good tensile properties, as shown in chapters 3 to 5 and in other references [1, 4]. However, the focus of this study is on its fracture toughness evaluation. The large sized bars of 25 x 40 mm rectangular cross-sections have been obtained by extruding both cold compacted SWAP powders and cast billets at various temperatures. From those extruded bars, the three-point bending test specimens used for fracture toughness tests were machined. This size of extrusion rod has been also used for obtaining the tensile and compression test specimens of different orientations, as shown in chapter 5. Fracture toughness tests were performed at room temperature on 3-point bending test specimens, having straight through notch, according to both ASTM E 399 and ASTM E 1820 standards [21, 22]. The thickness, width and span of the specimens were 8, 16, and 64 mm respectively, while the total length was 68 mm, as illustrated in Fig. 6.1. The specimens were machined from the extruded bars so that the plane of the machined notch is

normal to the extrusion direction. The integral knife edges were set up at the crack mouth to enable the use of a double cantilever clip-in displacement gage to measure the crack opening displacement (COD) during test. Fatigue pre-crack was developed in the specimens using a sinusoidal loading with the maximum load of 900 N, load ratio of 0.1 and a frequency of 20 cps using a servo-hydraulic axial fatigue testing machine (Shimadzu: Servopulser E100KN). The ratio of the fatigue pre-crack length to the specimen width was set to 0.5 for all specimens. The final fracture stage of the fracture toughness test was carried out using stroke control on the above mentioned tensile testing machine with the loading rate of 0.0125 mm/s, which corresponds to the rate of increase of stress intensity factor of 0.75 MPa $m^{1/2}$ /s [21]. The pre-cracked specimens were loaded in bending with slow rate using displacement control mode until they could sustain no further increase in load. The load was recorded against the COD during test. The final fracture of the specimens was then performed after cooling with liquid nitrogen to allow for brittle fracture with no further deformation. The fracture surfaces of specimens were then evaluated and the fatigue precrack measurements were performed at relevant positions. Details of test procedure and equations used to calculate the fracture parameters can be seen in the relevant ASTM E 399 and ASTM E 1820 standards. Three specimens for each condition were machined to be used for calculating an average.

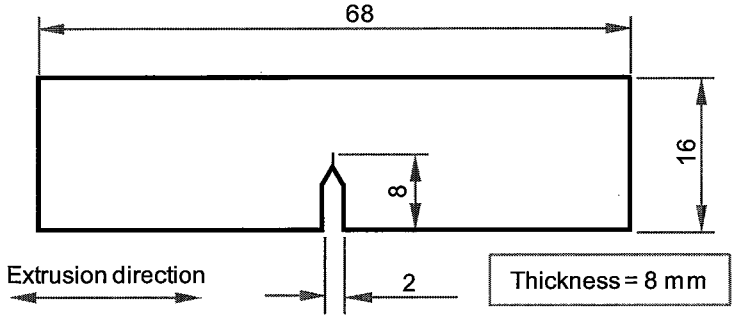

Fig. 6.1 fracture toughness 3-point bending specimen.

6.3. Results and discussion

The tensile and fracture toughness parameters results of extruded AMX602 alloy are listed in Table 6.1. It can be noticed that the tensile properties are remarkably different from those previously reported for the same alloy when extruded to small size bars (7 mm diameter rods), as shown in chapter 5. The tensile and yield strengths are lower and the elongation is higher in the case of bigger size extrusions. The load-COD records of 3-point bending fracture toughness test specimens of cold-compacted AMX602 alloy powder extruded at 573, 623, and 673 K as well as cast billet extruded at 673 K are shown in Fig. 6.2. Although the extruded cast billet has shown very similar elongation value to that of extruded SWAP powder in the case of tensile test, it has shown much broader curve in the case of pre-cracked specimens. This is due to the difference in the local yielding phenomena between both, as it could be seen that the yield strength and the ratio of yield strength to ultimate strength of extruded cast billet are much lower than that of extruded SWAP powder, as shown in Table 6.1. According to ASTM E 399 standard, a secant line was drawn with its slope equal to 95% of the slope of the initial portion of the record, and both P_Q and P_{max} were determined for each condition. Accordingly, K_Q values were also calculated based on the appropriate equation. The ratio of P_{max} / P_Q has exceeded 1.1 for all cases, and hence, no valid K_{IC} value could be obtained [21]. The reason is that the dimensions of the test specimens do not enable obtaining valid K_{IC} values for that alloy given its above mentioned elongation levels as a sign of its remarkable ductility. Although these values of K_Q are not valid K_{IC} values, they are still comparable to those previously reported for magnesium alloys in various conditions [11-20]. Apart from the ratio of P_{max} / P_Q exceeding 1.1, all the other validation criteria were passed by all specimens. Most of these validation criteria are based on the pattern of fatigue pre-crack configuration.

Figure 6.3 indicates that the crack propagation was sufficiently parallel to the machined notch, and that no remarkable difference of the crack lengths in the center and at the edges of the specimens. It is also noted that extruded SWAP powder specimen showed much wider shear lips on the sides of the specimen than that of extruded cast billet, a sign for higher ductility in the extruded SWAP powder.

Table 6.1 Tensile and fracture toughness properties of extruded AMX602 alloy SWAP powder and cast billet

Specimen conditions	UTS [MPa]	YS [MPa]	El [%]	K_Q [MPam$^{1/2}$]	CTOD [μm]	K_{IC} [MPam$^{1/2}$]
SWAP extruded at 573K	373	339	17.4	17.5	58	44.6
SWAP extruded at 623K	362	305	19.5	15.0	45	40.3
SWAP extruded at 673K	359	281	15.1	16.0	46	38.2
cast extruded at 673K	277	203	16.3	11.2	48	38.6

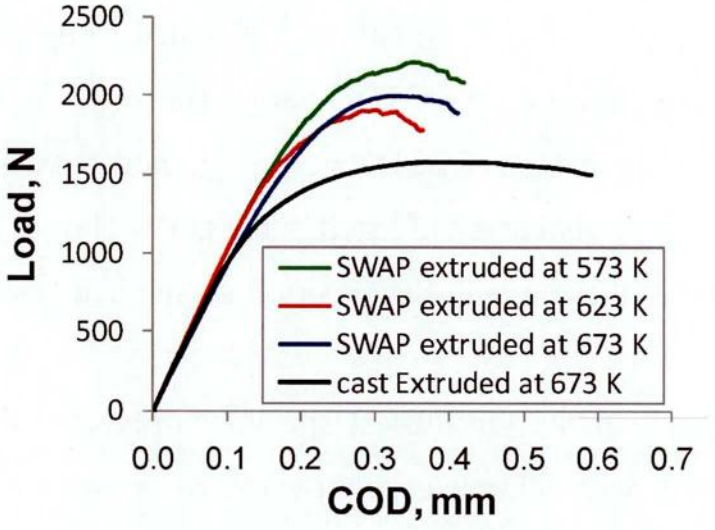

Fig. 6.2 Load versus crack opening displacement record for fracture toughness 3-point bending test samples.

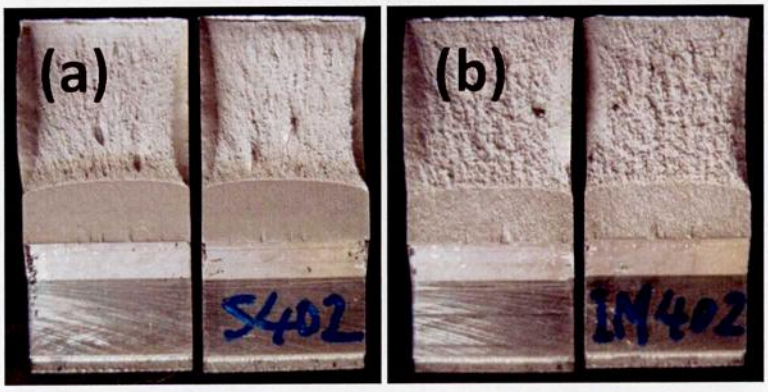

Fig. 6.3 Macrographs for fracture surfaces for fracture toughness 3-point bending test samples extruded at 673 K for both SWAP powder (a) and cast billet (b).

The need for another fracture parameter that suits materials with higher plasticity, hence, arose. The crack tip opening displacement (CTOD) was then calculated, according to ASTM E 1820 standard [22], based on the same available experimental data obtained for K_{IC} test. The values of CTOD obtained for the tested conditions are also listed in Table 6.1. These values are higher than those of the previous reports of magnesium alloys, in which the CTOD values had an average of 19 μm for rolled AZ31 alloy [16] and 11 μm for extruded AZ61 alloy [23], although obtained using the stretch zone analysis technique. Based on the CTOD values shown in Table 1 and using the equation of relating K_{IC} to CTOD values [16], the K_{IC} values for the Mg-Al-Mn-Ca alloy were obtained and listed in the table. They had much higher values than most of those previously reported for the magnesium alloys [11-20].

Fractography of the tensile test specimens revealed that the ductile fracture occurred with dimpled pattern clearly observed specially for extruded SWAP powders, as shown in Fig. 6.4 (a). More enlarged observation image indicated that the dimples had the comparable sizes to

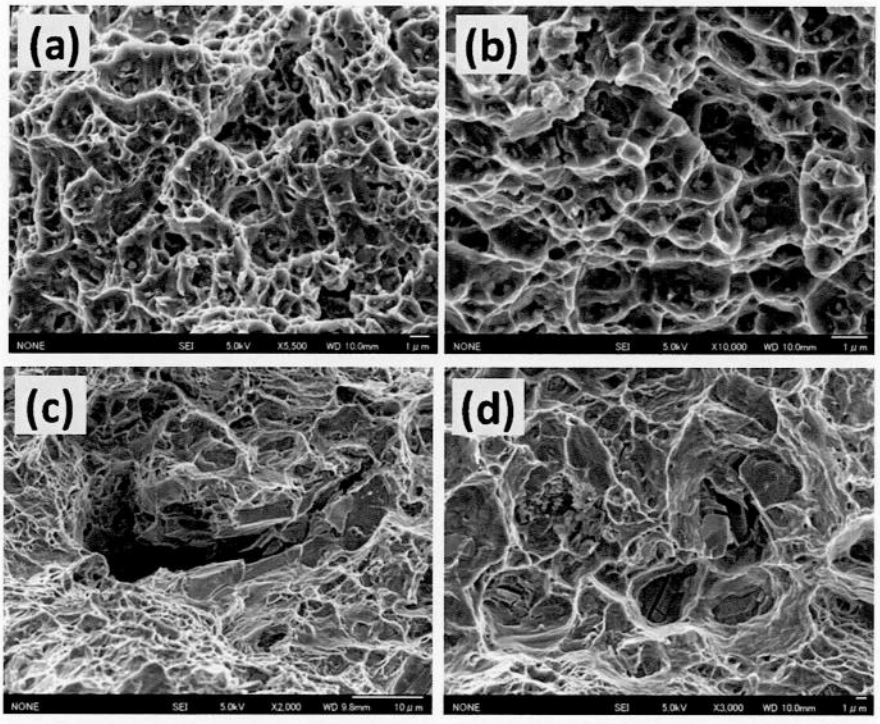

Fig. 6.4 Micrographs of fracture surface of tensile test samples:
a- SWAP extruded at 673 K lower magnification.
b- SWAP extruded at 673 K higher magnification.
c- cast billet extruded at 673 K showing micro-cracks emanating from fractured compound particles.
d- cast billet extruded at 673 K showing minor fractured compound particles.

that of the grain sizes reported herein, as shown in Fig. 6.4 (b). The extruded cast billet, however, showed signs of local brittleness occurring randomly on the fracture surface. The larger sizes of the compound particles resulted in micro-cracks emanating from the fractured particles, as shown in Fig. 6.4 (c), which could not sustain the increased local strains due to the large difference in ductility between compound particles and the matrix. Dispersed particles with lower sizes, like ones shown in Fig. 6.4 (d), have either shown no micro-cracks when fractured or even not fracture at all. These observations were consistent with those previously reported for magnesium alloys [24].

Figure 6.5 showed the morphology of both Al_2Ca and Al_6Mn compound particles existing on the fracture surfaces. It could also be noted that the morphology of the particles played a vital role in the determination of their susceptibility to fracture in which round shaped particles (Al_6Mn) have shown less possibility of fracture than that of irregular shaped ones (Al_2Ca). These results suggested that the rapid solidification powder metallurgy route could result in the remarkable improvement of the performance of the magnesium alloy containing very fine and round shaped compounds as shown in chapter 4.

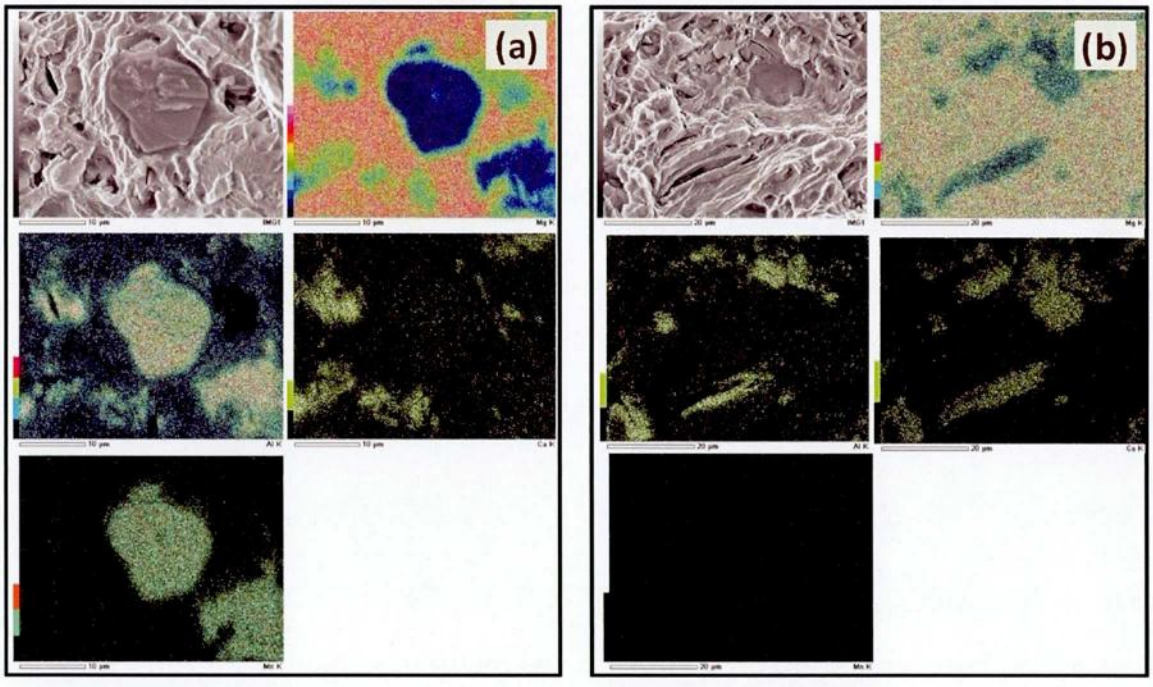

Fig. 6.5 EDS analysis of the fracture surface of tensile test specimen of cast billet extruded at 673 K showing both Al-Mn (a) and Al-Ca (b) compound particles.

6.4. Summary and Conclusions

The fracture toughness of extruded AMX602 alloy produced using rapid solidification powder metallurgy route has been investigated according to both ASTM E399 and ASTM E 1820 standards. The effects of grain size and intermetallic compound morphology on K_{Ic} were evaluated by comparing to the extruded AMX602 cast alloy with coarse microstructures. The following conclusions were obtained in this chapter:

- The rapid solidification powder metallurgy route could result in the remarkable improvement of the fracture toughness of magnesium alloy containing very fine and round shaped compounds

- Very large sizes for fracture toughness test specimens were necessary to obtain valid plane strain fracture toughness (K_{Ic}) values for magnesium alloys according to ASTM E399 standard, depending on their strength and toughness, which reaches about 110 mm as a minimum level in some cases [11].

- The AMX602 alloy showed values of fracture toughness that are comparable to that of other magnesium alloys, while maintaining superior tensile properties.

- The crack tip opening displacement parameter (CTOD), as per ASTM E1820 standard, can be used to evaluate the fracture toughness of magnesium alloys.

References

[1] A. Elsayed, K. Kondoh, H. Imai, J. Umeda, Materials and Design, 31 (2010) 2444-2453.

[2] A. Elsayed, J. Umeda, K. Kondoh, Acta Materialia, 59 (2011) 273-282.

[3] A. Elsayed, H. Imai, J. Umeda, K. Kondoh, Steel Research International, 81-9 (2010) 1304-1307.

[4] K. Kondoh, A. Elsayed, H. Imai, J. Umeda, T. Jones, Materials & Design, 31 (2009) 1540-1546.

[5] T. Homma, N. Kunito, S. Kamado, Scripta Materialia 61 (2009) 644-647.

[6] S.M. He, X.Q. Zeng, L.M. Peng, X. Gao, J.F. Nie, W.J. Ding, Journal of Alloys and Compounds 427 (2007) 316-323.

[7] T. Itoi, K. Takahashi, H. Moriyama, M. Hirohashi, Scripta Materialia, 59 (2008) 1155-1162.

[8] S.X. Ding, W.T. Lee, C.P. Chang, L.W. Chang, P.W. Kao, Scripta Materialia, 59 (2008) 1006-1009.

[9] T. Honma, K. Nagai, A. Katou, K. Arai, M. Suganuma, S. Kamado, Scripta Materialia, 60 (2009)451-454.

[10] C. Ma, M. Liu, G. Wu, W. Ding, Y. Zhu, Materials Science and Engineering A, 349 (2003) 207-212.

[11] S. Barbagello, E. Cerri. Engineering Failure Analysis 11 (2004) 127-140.

[12] H. Somekawa, T. Mukai. Sripta Materialia 53 (2005) 1059-1064.

[13] H. Somekawa, Y. Osawa, T. Mukai. Sripta Materialia 55 (2006) 593-596.

[14] H. Somekawa, T. Mukai. Sripta Materialia 53 (2005) 541-545.

[15] H. Somekawa, T. Mukai. Journal of Alloys and Compounds 417 (2006) 209-213.

[16] T. Sasaki, H. Somekawa, A. Takara, Y. Nishikawa, K. Higashi. Materials Transactions 44-5 (2003) 986-990.

[17] H. Somekawa, H. Kim, A. Singh, T. Mukai. Journal of Materials Research 22-9 (2007) 2598-2608.

[18] H. Somekawa, T. Mukai. Scripta Materialia 54 (2006) 633-638.

[19] H. Somekawa, A. Singh, T. Mukai. Scripta Materialia 56 (2007) 1091-1094.

[20] H. Somekawa, T. Mukai. Materials Science and Engineering A 459 (2007) 366-370.

[21] ASTM E 399, Standard test method for plane-strain fracture toughness of metallic materials. ASTA International, West Conshohocken, PA, 2001.

[22] ASTM E 1820. Standard test method for measurement of fracture toughness. ASTA International, West Conshohocken, PA, 2001.

[23] T. Sasaki, Y. Takigawa, K. Higashi. Materials Science and Engineering A 479 (2008) 117-124.

[24] T.S. Srivastan, S. Vasudevan, M. Petraroli. Journal of Alloys and Compounds 461 (2008) 154-159.

Chapter 7 Ballistic impact of extruded magnesium alloys: Experimental and simulation study

In this chapter, the experimental investigations, as well as the FEM simulation results, of the ballistic impact properties of hot extruded AMX602 alloy powder were presented to study the dynamic response of magnesium alloys. A user-defined FEM material model which imitates the mechanical characteristics of magnesium alloys based on anisotropic Hill function was developed, verified and then used for the dynamic simulation.

7.1. Introduction

The static mechanical properties such as tensile, compression and fracture toughness, of magnesium alloys have been extensively studied in numerous references, as well as in previous chapters. It has been shown previously that the powder metallurgy processing has resulted in improved mechanical properties of magnesium alloys due to their fine microstructures. Hence, the need for studying the dynamic performances of the magnesium alloys fabricated by using rapid solidification powder metallurgy has arisen, as it could open a wider market for magnesium alloys. On the other hand, the simulation of the ballistic impact test was needed to be able to predict the dynamic response of the extruded Mg alloy. After performing some simulation trials using LS-DYNA software, it became clear that it was necessary to develop a sound material model that can precisely imitate the mechanical response of the alloys.

Previously, the use of coupled experimental and FEM simulation techniques has been proven crucial to evaluate the local stresses and strains precisely [1-4]. The importance of this technique arises from the limitation

of the experimental measurements to the global information like forces and displacements [1]. Although some precise measurement devices can give more information about local parameters like the strain, those measurements are also limited to specific positions where such devices are attached, like strain gages. The necking stage in a steel specimen has been locally studied using the same technique, which shows its applicability in predicting the large deformations [2, 3]. It was also applied to investigate the copper specimens with a large strain range deformation, and proved good accordance with the experimental results [4]. On the other hand, the simulation of tensile test was also used to predict the necking behavior development in the tensile test specimen precisely [5]. Even tests other than tensile have also been coupled with the simulation results to evaluate the constitutive tensile behavior, in terms of stress-strain curves, like the small punch test [6, 7]. Hence, it is proposed in this study to use that technique for evaluating the mechanical performance of magnesium alloys.

Despite the lack of available data with high reliability on the dynamic response of magnesium alloys, the ballistic impact testing has been used for the evaluation of the dynamic behavior of alloys and structures under high velocities over a range of specimen configurations [8-11]. The fracture behavior was the main emphasis in some of the previous works with various types of projectile configurations [8, 9]. The effect of ballistic impact on the deformed microstructure was also studied for AM60B magnesium alloy at hyper-velocities [10].

For the purpose of simulation of the dynamic response of the AMX602 alloy, the material models available in the LS-DYNA software that have a potential to represent the alloy have been employed. Most of these models are based on the isotropic Mises yield function [12]. However, the alloy characteristics like the anisotropy and the strain rate effect have

resulted in the importance of developing a better representative material model, which can take into consideration the most important characteristics of the alloy.

The user defined material model subroutine that was previously developed based on the anisotropic Hill function has been selected for that purpose [13]. An optimization methodology has been used to obtain the material model parameters precisely by using the experimental and simulation results of both the tensile and compression tests. Due to the similarity of nature of input and output parameters in both tensile and compression tests, the material model has been verified using the comparison of the experimental and simulation results of bending test. Finally, the simulation of the ballistic impact test was carried out, and both the experimental and FEM results were compared together for the evaluation of the reliability of the material model.

7.2. Experimental procedure

The tensile and compression tests were performed for specimens oriented at 0, 45, and 90° angles with the extrusion direction of both AMX602 and ZAXE1711 alloy powder materials extruded at 623 K. The specimens' configurations were the same as those previously shown in chapter 5. Moreover, the bending test specimens, shown in Fig. 7.1, have also been obtained with the same orientations like that of tensile and compression specimens. The bending test was carried out on the universal testing machine, used for tensile and compression tests, using a stroke control with the loading speed of 0.45 mm/s.

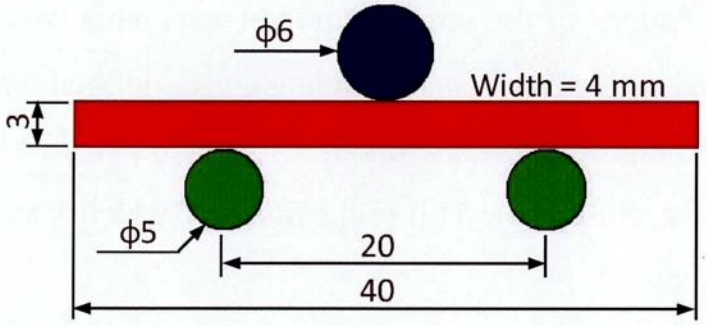

Fig. 7.1 Bending test specimen configuration, with the loading punch and support rollers.

The ballistic impact test was carried out by launching a stainless steel ball of 6 mm diameter against the magnesium disc specimen of 38 mm diameter and 3 mm thickness with the average speed of 140 m/s., as shown in Fig. 7.2. The compressed air is used to launch the ball with high speed into the directing tube, and then to the specimen. The speed of the ball was measured using an optical speedometer ahead of the specimen. After the test, the response of the specimen was evaluated by measuring the front surface indentation and the back surface protrusion caused by the ball strike.

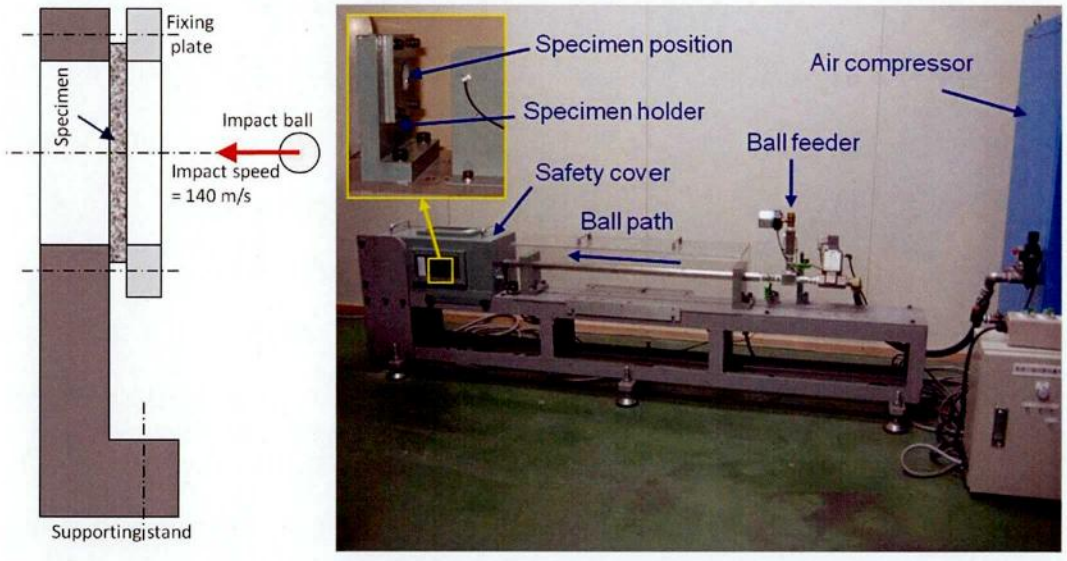

Fig. 7.2 Ballistic impact test configuration and the specimen support stand.

The simulations of the aforementioned tests have been carried out by using LS-DYNA software when embedding a user defined material model as a subroutine in the program. That model was previously developed by N. Ma [13] based on the anisotropic Hill yield function which was defined by the following equation

$$\sqrt{F(\sigma_{22}-\sigma_{33})^2+G(\sigma_{33}-\sigma_{11})^2+H(\sigma_{11}-\sigma_{22})^2+2L\sigma_{23}{}^2+2M\sigma_{31}{}^2+2N\sigma_{12}{}^2}=\sigma_Y$$

where, F, G, H, L, M, N are coefficients which can be determined by 6 initial yield stresses σ_{Y11}, σ_{Y22}, σ_{Y33}, σ_{Y12}, σ_{Y23}, and σ_{Y31} using following Equation (2).

$$F=\frac{1}{2}[(\frac{\sigma_{Y11}}{\sigma_{Y22}})^2+(\frac{\sigma_{Y11}}{\sigma_{Y33}})^2-1],\quad G=\frac{1}{2}[(\frac{\sigma_{Y11}}{\sigma_{Y33}})^2+1-(\frac{\sigma_{Y11}}{\sigma_{Y22}})^2]$$

$$H=\frac{1}{2}[1+(\frac{\sigma_{Y11}}{\sigma_{Y22}})^2-(\frac{\sigma_{Y11}}{\sigma_{Y33}})^2],$$

$$L=\frac{1}{2}(\frac{\sigma_{Y11}}{\sigma_{Y23}})^2,\quad M=\frac{1}{2}(\frac{\sigma_{Y11}}{\sigma_{Y31}})^2,\quad N=\frac{1}{2}(\frac{\sigma_{Y11}}{\sigma_{Y12}})^2$$

Those initial yield stresses represent the variation of the yield stress among different directions. If F=G=H=1/2 and L=M=N=3/2, the yield function is just the same with isotropic Misses yield function. Fig. 7.3 shows the initial yield surfaces if the ratio $\sigma_{Y11}/\sigma_{Y22}$ of yield stress σ_{Y11} in extrusion direction and yield stress σ_{Y22} in transverse direction is assumed to be 1.0, 2.0, 3.0, 4.0, respectively. Increasing this ratio moves the yield surface to areas of anisotropy behavior. As it will be shown later in this chapter that the strength of this alloy shows strong dependence on the strain rate, it is also important to be considered in this material model. Figure 7.4 shows the availability of this material model to consider the strain rate effect on both the tensile and compression stress-strain behaviors. Independent input curves can be assigned for tensile and compression sides separately as shown in the figure.

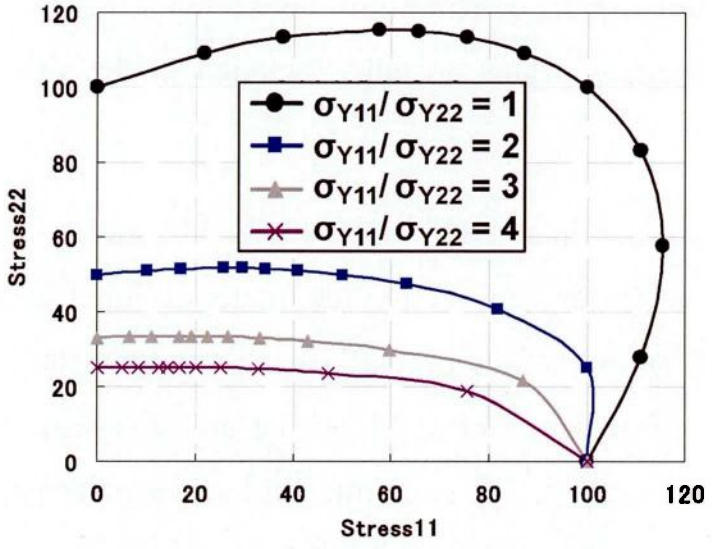

Fig. 7.3 Initial yield surfaces of the developed material model at various yield stress ratios [13].

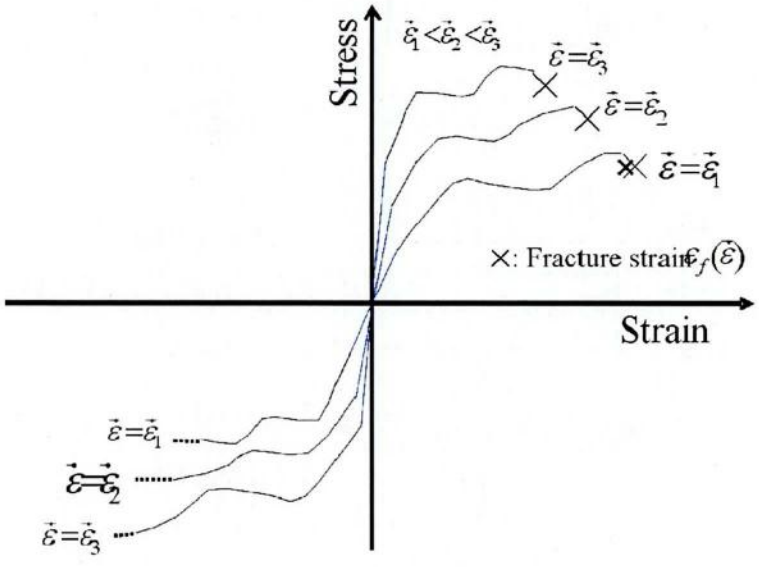

Fig. 7.4 Independent stress-strain curves for tension and compression at different strain rates [14].

In other words, the effects of strain rate on Young's modulus, plastic work hardening and fracture strains are also included in the simulation by this material model.

Using the preliminary simulation trials, it could be inferred that a precise methodology for optimizing the material input parameters (true stress-true plastic strain data) is needed. Hence, the flaw chart shown in Fig. 7.5 has been performed in which the tensile and compression simulations were used for optimization. The experimental load-displacement curves were first obtained from both experiments, and then, modified as true stress-true plastic strain data points that were next input as material model parameters. The simulation load-displacement resultant curves were later obtained and compared to those of the experimental results. When needed, the modification of the stress-strain data was performed until a good agreement was obtained between experimental and simulation results.

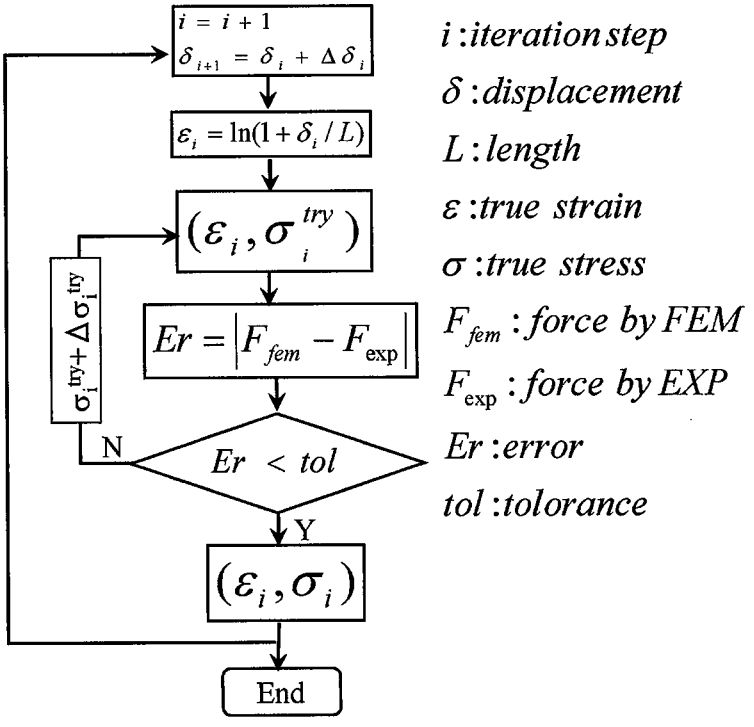

Fig. 7.5 Flow chart showing the optimization procedure used to adjust the material model parameters.

The tensile and compression models used for simulation are illustrated in Fig. 7.6. In both models, 2-dimensional axi-symmetric shell elements were used, with one fourth of the tensile test model and a half of the compression test model due to their symmetry. On the other hand, the 3-dimensinal brick elements were used to model the bending test specimen that is used for the simulation to verify the proposed optimization methodology and material model. The loading punch and support rollers were modeled using shell elements. In all the aforementioned simulations, the loadings of the specimens have been done by applying a time-displacement curves.

The 3-dimentional model for the ballistic impact test simulation, however, is shown in Fig. 7.7. Explicit analysis has been employed with the application of the newly developed material model. The steel ball projectile was launched against the magnesium plate using an initial velocity of 140 m/s, like the one used in ballistic experiments. In this simulation, a vibration damping coefficient, based on previous experience with dynamic simulation, has been set.

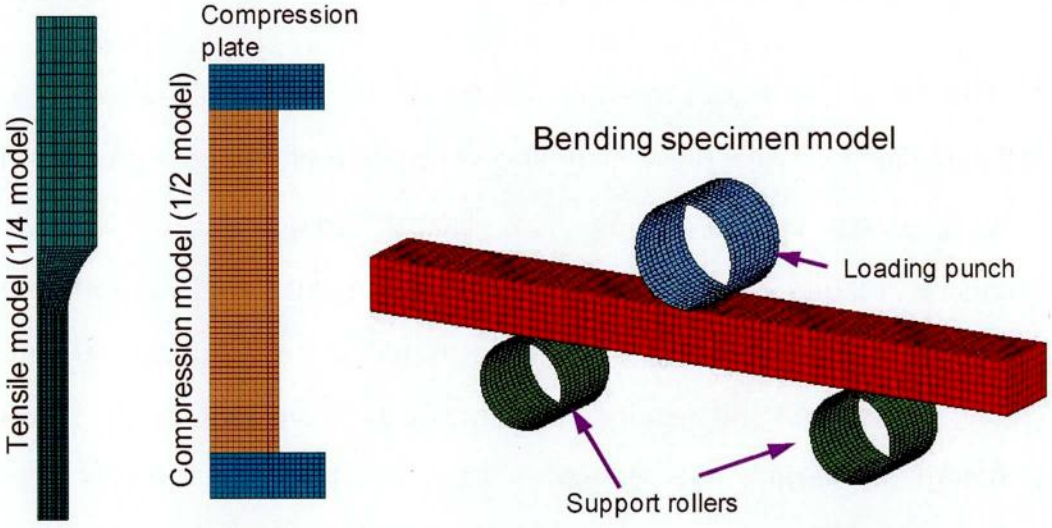

Fig. 7.6 Tensile, compression and bending test models used for simulation, showing the mesh division.

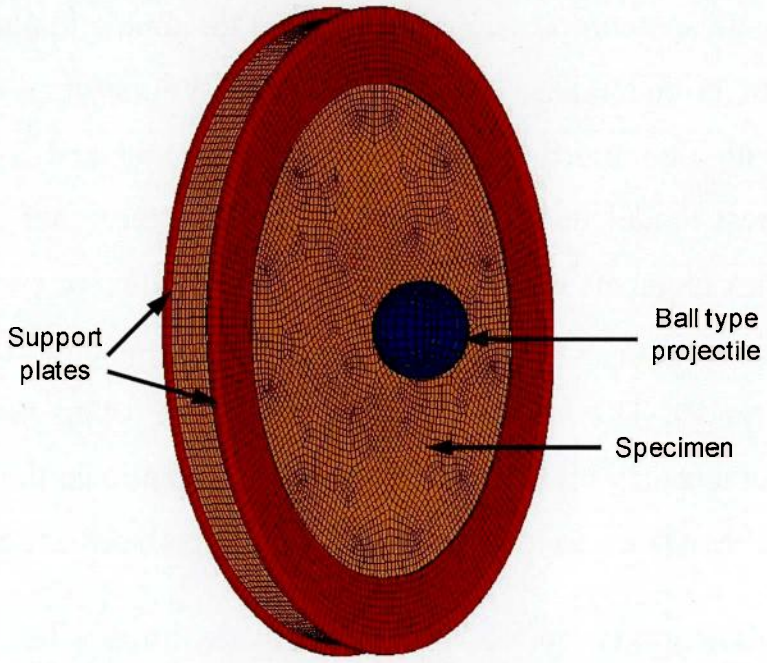

Fig. 7.7 Ballistic impact test model showing the mesh division of the specimen, support plates and the strike ball.

7.3. Results and discussion

7.3.1. Experimental test results

The tensile and compression results of the AMX602 alloy extruded SWAP powder has been previously shown in chapter 5, and summarized in load-displacement curves in Fig. 7.8. The difference of the tensile and compression results at different orientations shows the importance of considering the anisotropy in the material model. The strain rate effect was also investigated and the results of tensile tests at various loading speeds, from 0.5 to 500 mm/s, are shown in Fig. 7.9. It can be shown that the increase in the strain rate results in a slight increase in both yield and tensile strengths, but a drastic decrease in the elongation-to-failure of the extruded

AMX602 alloy SWAP powder. These results also show the importance of considering the strain rate effects in the material model.

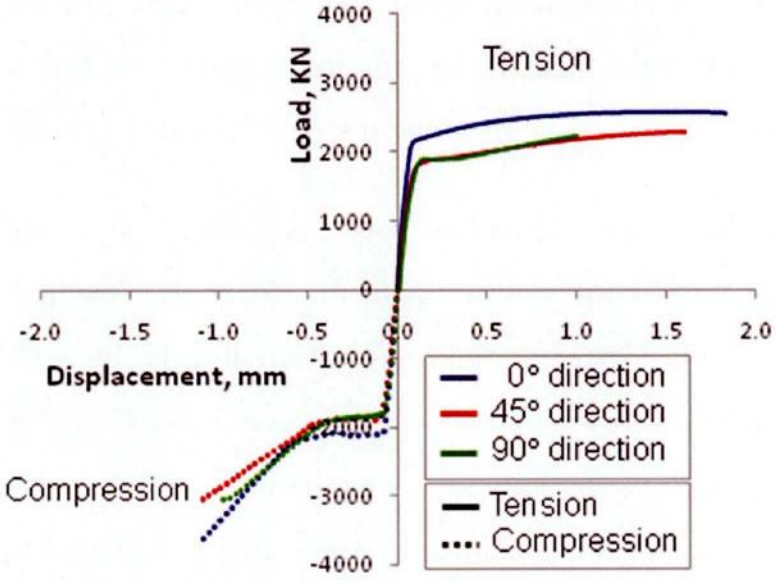

Fig. 7.8 Experimental load-displacement results of tensile and compression tests at various specimen orientations.

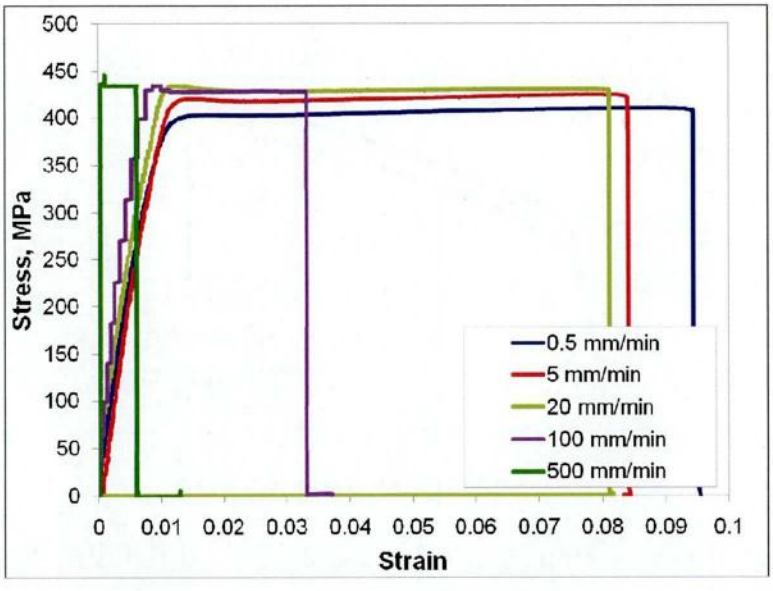

Fig. 7.9 Strain rate effect on the tensile properties of the extruded alloy.

Bending tests were also performed for the purpose of providing a verification basis of the proposed optimization methodology and the material model. The results of bending tests at various specimen orientations are shown in Fig. 7.10. The load-displacement curves obtained for specimens with 0, 45 and 90° orientations are shown with a behavior more similar to that of tensile test, than that of compression test. This is due to the fact that the fracture usually occurs in the tension side of bending specimens.

The ballistic impact tests have been performed on extruded AMX602 SWAP powder specimens, and the deformation of the specimen after test is shown in Fig. 7.11. The front side indentation and the back side protrusion diameters were 4.20 mm and 0.48 mm, respectively. Cracking occurred at the back side of the specimen, which was the tension side. However, the ball could not pass through the specimen. Even at that extremely high strain rate, the extruded AMX602 alloy SWAP powder has proven enough toughness which could survive that severe condition. These results indicate that the magnesium alloys via powder metallurgy route can provide a potential solution for light weight dynamic applications like automobile and airplanes.

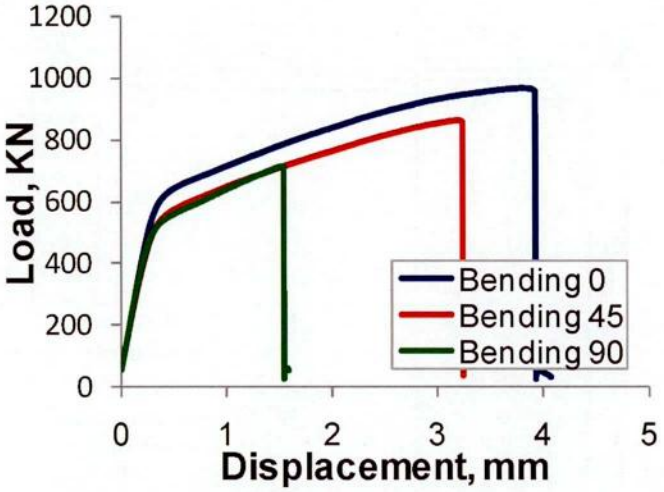

Fig. 7.10 Load-displacement curves of experimental bending tests at various specimen orientations.

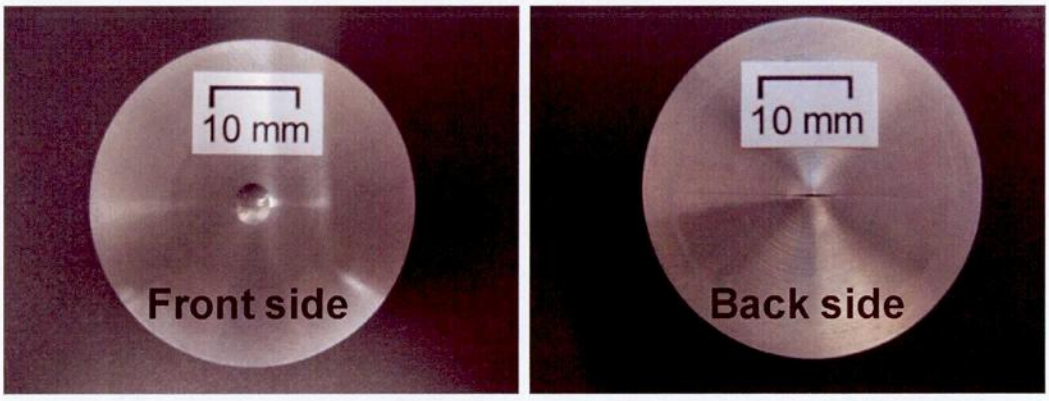

Fig. 7.11 The deformation of ballistic impact test specimen.

7.3.2. Simulation results and comparison with experimental ones

The simulations of various tests have been performed for different purposes as previously shown. The tensile and compression simulations were carried out to identify the mechanical properties of the alloy within the proposed optimization procedure shown in Fig. 7.5. The inputs for both the tensile and compression simulations were the load-displacement curves shown in Fig. 7.8, but after being modified as true stress-true plastic strain curves, as shown in Fig. 7.12. Those curves were then provided as discrete input points for simulation which showed the plastic behavior of the alloy. The results of those simulations are shown in Fig. 7.13 in terms of the effective stress distribution plots in both tensile and compression specimens. The specimen behaviors during tests were well imitated in the simulations using the proposed model. The necking stage has also occurred in the simulation based on the actual loading conditions. The resultant load-displacement curves obtained from simulations, after being optimized according to the procedure shown in Fig. 7.5, were then compared to those of experimental results, as shown in Fig. 7.14. Both the simulation and experimental results coincide to each other. This means that the proposed

material model and methodology for optimization have yielded good agreement between both FEM and experimental results.

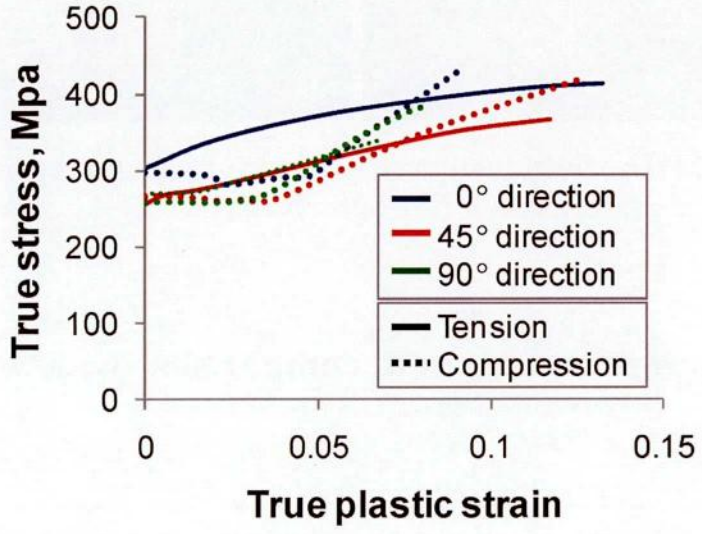

Fig. 7.12 True stress-true strain plots used as inputs for simulations.

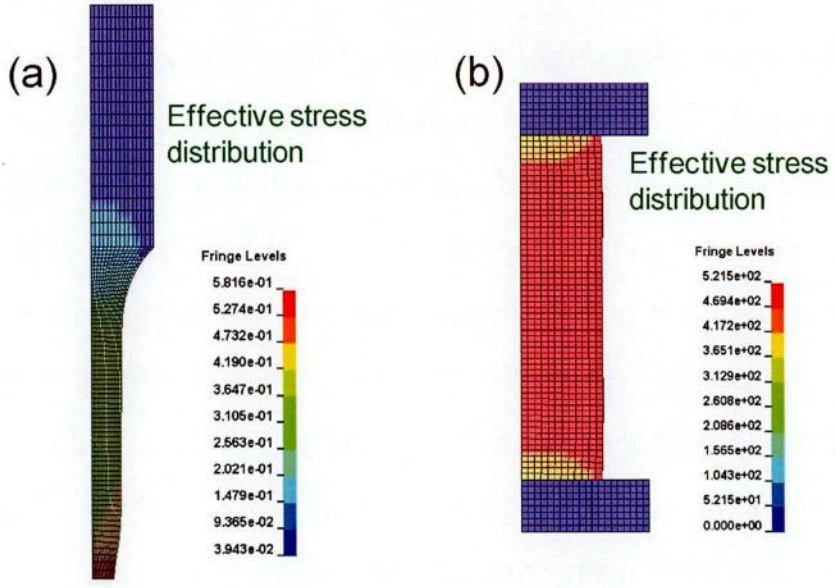

Fig. 7.13 Simulation results showing the effective stress distribution in tensile (a) and compression (b) test specimens.

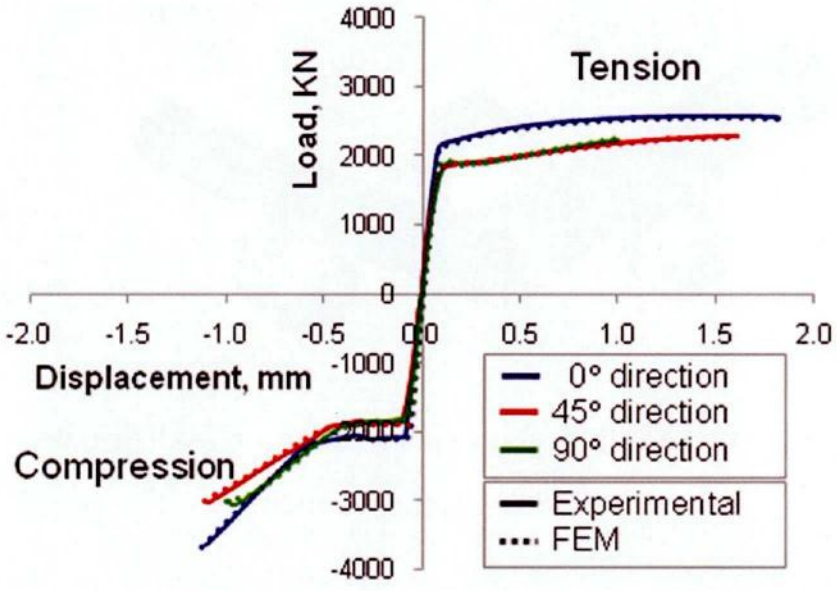

Fig. 7.14 Comparison between experimental and FEM results of tensile and compression tests.

The proposed model could be verified by performing the bending test simulation, which, unlike the tension and compression simulations, provide input and output data of different nature. While the inputs are based on tensile and compression properties, the output load-displacement curves at the load line of the experimental bending tests are obtained and compared to the simulation results. The deformed shape of the specimen and the plot of effective stress are shown in Fig. 7.15. The comparison of both experimental and FEM results of the bending test have also shown good agreement for all specimen orientations, as shown in Fig. 7.16. The experimental and FEM results show a near-coincidence to each other. These results show that the proposed model provides sound prediction of the alloy behaviors under different conditions.

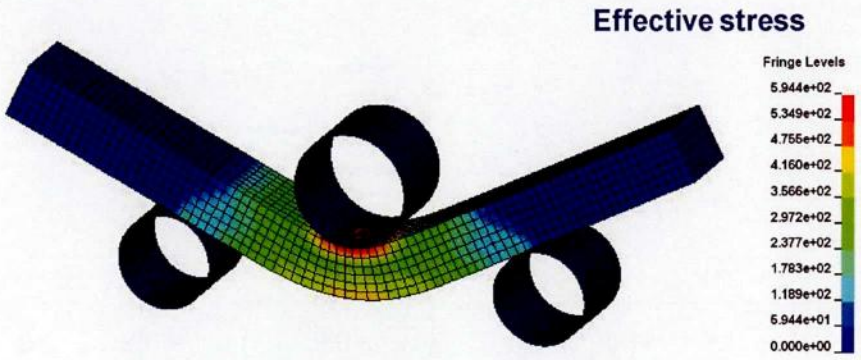

Fig. 7.15 Deformed shape with the effective stress distribution of the bending test specimen.

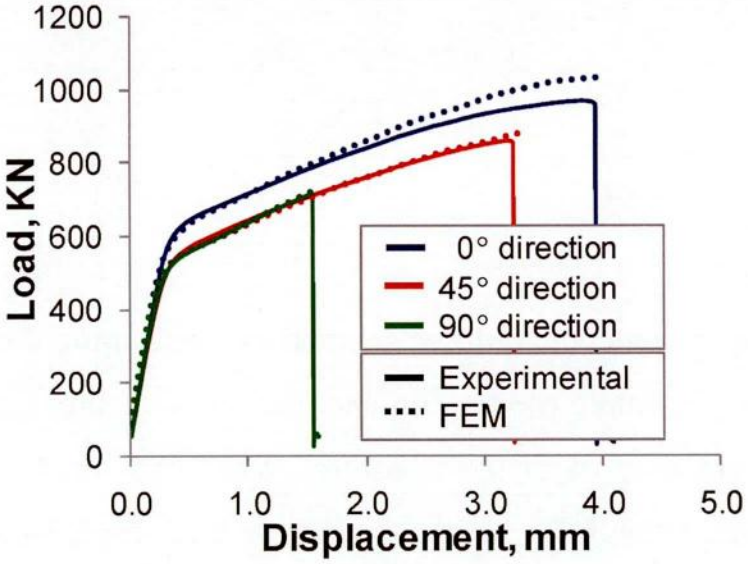

Fig. 7.16 Comparison between experimental and FEM results of the bending test.

The deformed shape and the plastic strain distribution plot for the ballistic impact test specimen are shown in Fig. 7.17. The deformation of the specimen is precisely similar to that of the experimental results in Fig. 7.11. The deformation parameters, in terms of the front side indentation diameter (d1) and depth (z1) and the back side protrusion diameter (d2) were then evaluated from the simulation results. The comparisons of those parameters

with those of the simulation using LS-DYNA material model (Mat. 124), as well as of experimental results are provided in Table 7.1.

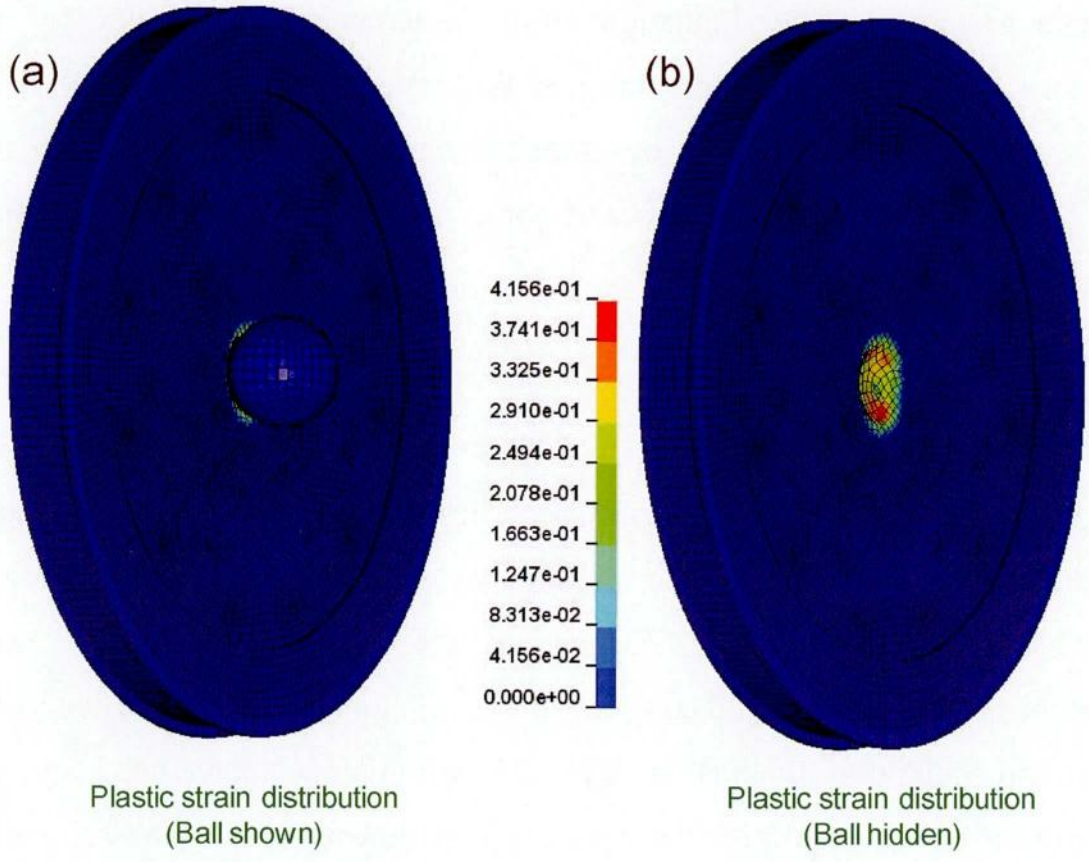

Fig. 7.17 The deformed shapes and the plastic strain distributions of the ballistic impact test specimen in the full model (a) and after hiding the ball (b) to reveal the indentation morphology.

Table 7.1 The experimental and FEM results of deformation parameters of specimens after ballistic impact test

	d1 [mm]	z1 [mm]	d2 [mm]
Experimental results	4.20	0.90	0.48
FEM results using Mat. 124	3.40	0.50	0.20
FEM results using the developed material model	4.25	0.80	0.52

The comparisons of the results show that the developed material model has resulted in a good comparison to that of the experimental results. It is clear from the table that the developed material model provides much better accuracy of the simulation results in terms of closer values of the deformation parameters than those of the material model Mat. 124. This proves the efficiency of the developed material model for predicting the alloy behaviors in different conditions, including static and dynamic conditions, precisely.

Summary and Conclusion

Mainly, the ballistic impact properties of the AMX602 alloy powder extruded at 623 K has been investigated and simulated using a newly developed material model. The parameters of that model have been optimized using tensile and compression simulations, and then verified using bending simulation. Evaluation of the simulation models have been done by comparing their results to those of the experimental ones. The following conclusions were obtained:

- The proposed methodology could estimate the global plastic deformation parameters (true stress and true plastic strain) precisely based on force-displacement curves.
- The developed material model could effectively imitate the mechanical behavior of the alloy at different loading conditions.
- The anisotropy of the alloy was considered by using the proposed material model which is based on Hill anisotropic yield function.
- Verification of the model showed a good agreement between experimental and FEM results in bending simulation.

- The ballistic impact test of the extruded alloy indicated a good performance under such severe loading condition.

- The alloy behavior under ballistic impact loading was accurately predicted using simulation based on the developed material model, which showed better comparison with the experimental results than that of LS-DYNA embedded material model (Mat. 124).

References

[1] M. Springmann, M. Kuna, Computational Materials Science, 32 (2005) 544-552.

[2] E.E. Cabezas, D.J. Celentano, Finite Elements in Analysis and Design, 40 (2004) 555-575.

[3] M. Joun, J.G. Eom, M.C. Lee, Mechanics of Materials, 40 (2008) 586-593.

[4] S. Dumoulin, L. Tabourot, C. Chappuis, R. Arrieux, Journal of Materials Processing Technology, 133 (2003) 79-83.

[5] M. Joun, I. Choi, J. Eom, M. Lee, Computational Materials Science, 41 (2007) 63-69.

[6] J. Isselin, A. Iost, J. Golek, D. Najjar, M. Bigerelle, Journal of Nuclear Materials, 352 (2006) 97-106.

[7] A. Husain, D.K. Sehgal, R.K. Pandey, Computational Materials Science, 31 (2004) 84-92.

[8] D. Hwang, A. Hashimoto, D. Numata, T. Kikuchi, K. Takayama, Key Rngineering Materials, 3221-323 (2006) 654-657.

[9] T. Jones, R. Delorme, M. Burkins, W. Gooch, 23rd International Symposium on Ballistics, Tarragona, Spain 16-20 April 2007.

[10] D.L. Zou, L. Zhen, Y. Zhu, C.Y. Xu, W.Z. Shao, B.J. Pang, Materials Science and Engineering A, 527 (2010) 3323-3328.

[11] J.C.F. Millett, S.M. Stirk, N.K. Bourne, G.T. Gray III, Acta Materialia, 58 (2010) 5675-5682

[12] LS-DYNA users manual.

[13] Ninshu MA, User's manual of a general anisotropic material model, JSOL Corporation, 2006

Chapter 8 Summary

This research study has focused on the development of magnesium alloys which have a potential for increased structural applications through the use of the rapid solidification powder metallurgy processing. Specifically, alloys including AMX602, ZAXE1711, ZAXE1713 and ZK61 have been fabricated by hot extrusion of atomized powders. Improved performances could be obtained for these alloys when produced via powder metallurgy compared to their cast form. They were even proven superior to other Mg alloys and to the same Mg alloys fabricated by using the conventional powder metallurgy route.

The spinning water atomization process (SWAP) used to produce the AMX602 and ZAXE alloys and the gas atomization process used to produce the ZK61 alloy have resulted in relatively coarse powders with very fine microstructures. Moreover, the high solidification rate of these processes has also enabled the supersaturation of the alloying elements such as Mn, Ca and La. These microstructures were much finer than those of the alloys in their cast form, which showed much coarser α-Mg grain sizes and intermetallic compound particles.

The extruded magnesium alloys have shown the evolution of favorable microstructures which contain fine α-Mg grains and intermetallic compounds. The fine grain sizes of the extruded powders have shown values that were as low as 0.3 μm. The main reason for these microstructures was the powder metallurgy processing of fine magnesium powders that resulted in the dynamic recrystallization into further finer grains, promoted by the formation of finely dispersed compound particles. These fine microstructures have usually been aimed because they provide good mechanical properties through the increase of the yield strength with the grain refinement,

according to Hall-Petch relationship. Furthermore, intermetallic compound strengthening obtained from the homogeneously dispersed fine particles effectively promoted the alloy resistance to grain boundary sliding. The latter effect could also be supported through the proper selection of alloying element combinations, including Al-Ca, Al-Ca-La, and Zn-Zr.

Another important fruit of the extrusion of Mg-alloys rapidly atomized powders was the evolution of more randomized texture compared to that of extruded cast billets. The electron back scattered patterns (EBSD) have shown less intensity for the basal plane [0001] texture of the extruded SWAP powders. The incomplete dynamic recrystallization, which occurred mainly in extruded cast billets, has been shown as a major reason for the increased texture intensity of the basal plane due to the strong orientation of the deformed grains compared to that of recrystallized ones. The grain refinement and the homogeneous dispersion of fine compound particles have supported the evolution of such randomized textures.

The aforementioned microstructure and texture evolutions have resulted in obtaining excellent tensile, compression and hardness properties of Mg alloys fabricated by hot extrusion of the atomized powders. The extrusion temperature has been shown to affect the properties of the extruded Mg-alloys considerably. The yield and tensile strengths have increased, and the elongation has decreased when the extrusion was performed at lower temperatures. This effect has dominated that of consolidation conditions, i.e. both the cold compaction and the spark plasma sintering have yielded similar properties to each other. The alloys in this study have shown high tensile strength, which reached the level of 450 MPa for the ZAXE1711 alloy SWAP powder extruded at 573 K, while maintaining an elongation level of 17 %. Such properties are superior to other Mg alloys and conventional Al alloys. They are even comparable to the tensile properties of some steel

alloys, the engineering parts of which are more than four times heavier than those of magnesium alloys, due to the difference in densities.

By investigating both the tensile and compression properties at various specimen orientations, it could be confirmed that the randomized texture evolution of extruded SWAP powders of Mg alloys have resulted in a remarkable decrease in their anisotropy, especially compared to those of extruded cast billets. The yield strengths of both tensile and compression loadings of extruded SWAP powders have shown closer values to each other at various specimen orientations. ZAXE1711 alloy has shown further decrease of the anisotropy compared to that of AMX602 alloy, which was revealed to be due to the encouragement of the texture randomization through the presence of the rare earth La element. The latter effect has been previously reported to occur by the formation of the transverse component of texture.

To provide more information on the mechanical performance of Mg alloys, the plane strain fracture toughness (K_{Ic}) of extruded AMX602 alloy has been studied, as it is becoming more important to provide such information for alloys used in structural applications. It has been shown that no valid K_{Ic} value could be obtained using the available specimen sizes, as the ductility levels of the alloy require much bigger specimens. However, the crack tip opening displacement (CTOD) values have been evaluated for the extruded alloy. Comparison of such fracture toughness parameter to those of other alloys has revealed that it showed comparable values, and also has shown its superiority in some cases.

Apart from the aforementioned static mechanical properties, the dynamic performances of Mg alloys have also been investigated by performing ballistic impact tests on extruded AMX602 alloy SWAP powders.

The results have shown a good performance of the alloy under that severe loading condition. The prediction of the alloy behavior under such test has also been performed through its simulation by FEM method using LS-DYNA software. To accurately imitate the mechanical characteristics of the alloy, a newly developed material model has been introduced. The parameters of such a model have been optimized using a procedure based on preliminary tensile and compression test simulation results. After the verification of that material model using bending test simulation, it was used for the simulation of the ballistic impact test. The results of the above mentioned analyses have shown a good comparison between both the experimental and FEM results. This suggested the availability of the proposed material model for the accurate representation of the alloy characteristics.

A general view of the aforementioned results of the microstructure, texture, and mechanical properties of the Mg alloys fabricated via the hot extrusion of atomized powders shows the remarkable improvement of these alloys. That improvement has been obtained due to the combined effects of chemical alloying, powder metallurgy processing, and the appropriate selection of the processing conditions, including consolidation and extrusion stages. It also shows how wide a field of applications Mg alloys can get.

Acknowledgments

I would like to express my great gratitude to Prof. Katsuyoshi Kondoh for his Academic supervision and support during the entire course of my study. I am deeply thankful to him for his valuable guidance, instructions and discussions that directed my research achievements. My gratitude is then extended to Prof. Kohji Minoshima, Prof. Kazuhiro Nakata, Prof. Seiji Katayama, and Prof. Hidetoshi Fujii for their valuable and constructive comments about this thesis. Many thanks for the kind help of Mr. Yoshio Enomoto, President of Enomoto Machine Co., Ltd in my study and research experiments. I also highly appreciate the support of Dr. Hisashi Imai in every issue related to my study which really helped to proceed smoothly. My special thanks go to Dr. Junko Umeda, Mrs. Eri Nishiyama and all the staff members and students in Kondoh laboratory for their remarkable help, not only related to academic issues, but also to my life in Japan.

I appreciate the support of Prof. Ninshu Ma, from JSOL Corporation, in the field of FEM simulation. My special thanks are given to Dr. Isamu Otsuka, manager of Epson Atmix, for providing SWAP powders, and for the staff in Kurimoto Co. for providing the cast ingots and the big size extrusions which were used in this study.

I also acknowledge the financial support of the Ministry of Education, Science, Sports and Culture, Japan, and the Culture Affairs & Mission Sector, Ministry of High Education of Egypt to carry out this research work.

My deep gratitude is also to my professors at the CMRDI, Egypt: Prof. Mahmoud Nasr, Prof. Abdel-Moem El-Batahgy, Prof. Alber Sadek, Prof. Wafaa Abdel-Raouf, Prof. Khaled Abdel-Ghany, and Prof. Mohammad

Megahed from Cairo University for their valuable advice and encouragements.

My sincere thanks and acknowledgments go to my parents, my wife, and even my children for their continuous advice, support and encouragements that have always been strengthening to me to fulfill my duties towards my study.

List of publications

e. International Journals

1- A. Elsayed, K. Kondoh, H. Imai, J. Umeda, Microstructure and mechanical properties of hot extruded Mg-Al-Mn-Ca alloy produced by rapid solidification powder metallurgy, Materials & Design, 31 (2010) 2444-2453.

2- A. Elsayed, H. Imai, J. Umeda, K. Kondoh, Microstructure and mechanical properties of hot extruded ZK61 alloy produced by rapid solidified powder metallurgy, Steel Research International, 81-9 (2010) 1304-1307.

3- A. Elsayed, J. Umeda, K. Kondoh, Application of rapid solidification powder metallurgy to the fabrication of high-strength, high-ductility Mg-Al-Zn-Ca-La alloy through hot extrusion, Acta Materialia, 59 (2011) 273-282.

4- K. Kondoh, A.H. Elsayed, H. Imai, J. Umeda, T. Jones, Microstructure and mechanical responses of powder metallurgy non-combustive magnesium extruded alloy by rapid solidification process in mass production, Materials & Design, 31 (2010) 1540-1546.

5- J. Umeda, M. Kawakami, K. Kondoh, A. Elsayed, H. Imai, Microstructural and mechanical properties of titanium particulate reinforced magnesium composite materials, Materials Chemistry and Physics, 123 (2010) 649-657.

6- A. Elsayed, J. Umeda, K. Kondoh, The texture and anisotropy of hot extruded magnesium alloys fabricated via rapid solidification powder metallurgy, Materials & Design, under review.

7- A. Elsayed, K. Kondoh, Fracture toughness characterization of rapidly solidified Mg-Al-Mn-Ca alloy powder metallurgy via hot extrusion, Materials Chemistry and Physics, under review.

f. Domestic Journals

1- A. Elsayed, K. Kondoh, H. Imai, J. Umeda, M. Kawakami, Mechanical characteristics of hot extruded non-combustible magnesium alloy using water atomized powder, Transactions of JWRI 37-2 (2008) 43-49.

2- A. Elsayed, K. Kondoh, H. Imai, J. Umeda, Effect of different La additions on the microstructure and mechanical properties of hot extruded SWAP Mg-Al-Zn-Ca powder, Transactions of JWRI 38-1 (2009) 19-23.

3- A. Elsayed, K. Kondoh, H. Imai, J. Umeda, Effect of consolidation and extrusion temperatures on tensile properties of hot extruded ZK61 magnesium alloy gas atomized powders via spark plasma sintering, Transactions of JWRI 38-2 (2009) 31-35.

g. International conferences

1- A. Elsayed, H. Imai, J. Umeda, K. Kondoh, Improved mechanical response of hot extruded SWAP Mg-Al-Zn-Ca powder with different rare-earth element additions, Magnesium Alloys and their Applications, 26-29 October, 2009, Weimar, Germany.

2- A. Elsayed, H. Imai, J. Umeda, K. Kondoh, Microstructure and mechanical properties of hot extruded ZK61 alloy produced by rapid solidified powder metallurgy, Metal Forming 2010, 19-22 September, 2010, Nagoya, Japan.

3- A. Elsayed, K. Kondoh, N. Ma, Experimental and FEM evaluation of mechanical properties of hot extruded rapidly solidified powder metallurgy Mg-Al-Mn-Ca alloy, Visual-JW2010, 11-12 November, 2010, Osaka, Japan.

4- A. Elsayed, J. Umeda, K. Kondoh, The production of powder metallurgy hot extruded Mg-Al-Mn-Ca alloy with high strength and limited anisotropy, 2011 TMS Annual Meeting & Exhibition, to be held during 27 February-3 March, 2011, California, USA.

h. Domestic conferences

1- A. Elsayed, K. Kondoh, H. Imai, Microstructure and mechanical properties of hot extruded Mg-Al-Mn-Ca alloy produced by rapid solidification powder, 日本学術会議材料工学連合講演会, 22-24 October, 2008, Kyoto.

2- A. Elsayed , M. Kawakami, H. Fukuda, H. Imai, K. Kondoh, Effect of hot extrusion temperature on rapidly solidified Mg-Al-Mn-Ca alloy consolidated via both cold compaction and spark plasma sintering, 平成21 年度塑性加工春期講演会, 29-31 May, 2009, Kyoto.

3- A. El-sayed , M. Kawakami, H. Fukuda, H. Imai, J. Umeda, K. Kondoh, Mechanical Properties of Powder Metallurgy non-combustive Mg-Al-Mn-Ca alloy Produced by Rapid Solidification , 粉体粉末冶金協会第 103 回講演大会, 2-4 June, 2009, Kyoto.